UNIVERSITY OF CALIFORNIA
RIVERSIDE

Sea Ice Drift in Arctic Marginal Ice Zones Derived From Optical Satellite Imagery

A Dissertation submitted in partial satisfaction
of the requirements for the degree of

Doctor of Philosophy

in

Mechanical Engineering

by

Rosalinda Lopez

September 2021

Dissertation Committee:

Dr. Monica Martinez Wilhelmus, Chairperson
Dr. Marko Princevac
Dr. Akula Venkatram

The Dissertation of Rosalinda Lopez is approved:

Committee Chairperson

University of California, Riverside

Acknowledgments

I acknowledge that work in this dissertation has been reprinted or partially reprinted from previous published work in the journal Remote Sensing of the Environment, volume 234, February 2019 (Chapter 2). I am the primary contributor to this article, while Dr. Monica M. Wilhelmus and Dr. Michael Schodlok are contributors.

I gratefully acknowledge the support of the Graduate Assistance in Areas of National Need (GAANN) program from the Department of Education (award P200A180037).

My appreciation to the Department of Mechanical Engineering, staff, faculty, professors, and committee members for the vital funding, assistance and formation while at UCR.

I am obliged for the invaluable insight, help, and discussion from my collaborators which contributed to the significant improvement of my work. In particular Dr. Georgy Manucharyan, Dr. Jennifer Hutchings, Dr. Jennifer Lukovich, Dr. Michael Schodlok, and Dr. Patrice Klein for broadening my scientific abilities and oceanographic knowledge.

I would like to thank my family, labmates, and colleagues for their emotional and academic support. This achievement is a direct result of your sacrifice, support and love.

Finally, my deepest gratitude is to my advisor, Dr. Monica M. Wilhelmus. Her endless support, guidance, shared-knowledge and patience culminate in this work. Without her, my Ph.D. studies could not have been possible. I sincerely thank her for never giving up on me, no matter what academic or personal obstacle I faced during these past years. Thank you.

Para mis padres, Rosalinda Acosta Ángeles y José Roberto López Ramos.

Sus alas han levantado mi vuelo.

ABSTRACT OF THE DISSERTATION

Sea Ice Drift in Arctic Marginal Ice Zones Derived from Optical Satellite Imagery

by

Rosalinda Lopez

Doctor of Philosophy, Graduate Program in Mechanical Engineering
University of California, Riverside, September 2021
Dr. Monica Martinez Wilhelmus, Chairperson

Warming temperatures and extreme weather conditions have transformed the Arctic climate system. Most salient are the reduction of ice cover and the growth of marginal ice zones (MIZ). MIZ are regions along the ice edge where meso/submeso-scale variability strongly influences the sea ice field and vice versa. Understanding how sea ice and ocean circulation evolve in MIZ is crucial to fully characterize the mechanisms that control surface dispersion and consequently transform the Arctic.

Existing sea ice products cannot retrieve comprehensive dynamical observations in MIZ. As a result, critical dynamical processes are often overlooked in scientific studies and are not properly constrained in numerical models. The main goal of this study was to develop a sea ice detection algorithm designed to acquire measurements in MIZ extending throughout the 21st century.

Optical remote sensing imagery, namely Moderate-resolution Imaging Spectroradiometer (MODIS), was employed to develop an algorithm capable of retrieving the complex MIZ sea

ice motion. The algorithm filters the atmospheric conditions abating MODIS images while maximizing ice identification via image processing and feature matching techniques. The robustness of the method was tested along the eastern coast of Greenland. Upon validation, a unique dataset of sea ice characteristics and kinematics was extracted from Fram Strait and the Beaufort Sea from 2003 to 2020. The dataset included geometric shape parameters, along with Lagrangian trajectories, angular velocities, and Eulerian velocity fields.

The data was employed to assess the influence of meso/submeso-scale ocean turbulence on sea ice dynamics. First, an in-depth analysis of the role of atmospheric and oceanic forcing on ice floe motion demonstrated the importance of meso/submeso-scale processes driving sea ice drift. Next, the seasonal and decadal variability of the ice flow field in the summer and spring-time MIZ was quantified. In these regions, sea ice dynamics differed from the central Arctic basin, highlighting the importance of a correct parametrization of sea ice in MIZ. Finally, for the first time, satellite-tracked sea ice was employed as surface tracers to analyze the topology of the underlying flow field. The results were validated with high-resolution buoys, providing an additional resource to characterize the eddy field.

Contents

List of Figures

List of Tables

Chapter 1

Introduction

1.1 Dissertation overview

Based on the intrinsically coupled interactions between sea ice and oceanic turbulence, sea ice can provide a window to study the evolution of marginal ice zone (MIZ) dynamics in a rapidly changing Arctic. MIZ are regions important regions in between the ice edge and open ocean where strong temperatures and salinity gradients drive the dynamics in this regions. Extensive ongoing efforts have been made to acquire remote sensing observations to characterize sea ice drift. The framework and current limitations of the available sea ice drift tools are introduced in this chapter, followed by the research objectives of this investigation. Chapter 2 delineates the methodology applied to develop a sea ice tracking algorithm from multi-platform satellite imagery in the spring- and summer-time Arctic MIZ. In Chapter 3, the compilation of sea ice characteristics and kinematics is employed to assess

the role of atmospheric and oceanic forcing on ice floe motion. A strong correlation between sea ice and the dynamics of the underlying ocean currents is established via an idealized quasigeostrophic model. Moreover, the size, spatial patterns, and temporal variability of the eddy field are explored, for the first time, using sea ice drift observations. Chapter 4 depicts a comprehensive investigation of sea ice surface dispersion. The dynamical metrics quantified from the MODIS imagery are leveraged to infer the characteristics of the under-ice eddy field via single-particle dispersion statistical analysis of sea ice. In Chapter 5, high resolution *in-situ* data from the Multidisciplinary drifting Observatory for the Study of Arctic Climate (MOSAiC) campaign is used along with MODIS-derived sea ice observations. The single- and two-particle relative dispersion metrics from both datasets are quantified across a broad range of spatiotemporal scales along the Fram Strait and Greenland Sea MIZ. Despite their inherent differences, both datasets retrieve the same topological features, serving as a validation to the present work. Chapter 6 concludes this thesis with a final discussion of the accomplished research goals and objectives.

1.2 Background

Every fall, the indigenous communities along the coast of the Arctic Ocean look for the return of the ice, crucial for their survival. After a period of long sun exposure and warm spring temperatures, sea ice begins to form in the Arctic owning to reduced sunlight and a drop in atmospheric temperatures. However, in the last decades, warming temperatures and extreme weather conditions have introduced positive feedback mechanisms that have altered

this cycle and transformed the Arctic landscape [41, 85, 89]. A thinner and reduced ice cover exposes dark waters to solar radiation, increasing surface temperatures, accelerating sea ice melting in the spring, and delaying freezing in the fall [98]. Record lows of sea ice extent have been observed every summer over the past four decades [22]. Sea ice is now much younger, thinner, and more mobile [106, 108]. The elders from the indigenous communities recall the disappearance of so-called mother ice, the large multiyear ice, began decades ago [117]. Now, multiyear ice has essentially disappeared [77].

The projected effects are far-reaching from a conservation and geopolitical stance. A summer ice-free Arctic ocean is predicted as soon as 2035 [29]. Consequently, new navigation routes will open for commerce and tourism, while unexploited reserves of oil and gas will become accessible [25, 80]. Moreover, coastal erosion, rising sea levels, and the absence of ice will continue to displace communities dependent on marine resources [25].

The observed reduction of Arctic sea ice extent has transformed the Arctic climate system. A notable consequence of the reduced sea ice cover is the increase in size, duration, and influence of regions known as marginal ice zones (MIZ) [124]. MIZ are characterized by significant salinity and temperature gradients, critical in momentum and heat transfer in polar oceans [126]. Therefore, an amplification of MIZ has the potential to alter marine habitat, ocean circulation, and the dynamics of the Arctic climate system [109].

In MIZ, the interactions between sea ice and open waters intensify. As a result, sea ice to rotates and deforms more rapidly than in the central ice pack. Recent numerical and observational studies have demonstrated the importance of ocean eddies in the transport of

sea ice in MIZ [38, 47, 76]. As such, the sea ice drift field can be used as an indicator to gauge the evolution of MIZ dynamics in a rapidly changing Arctic.

Despite the advances in climate modeling, surveying field campaigns, and satellite monitoring, a complete parametrization of sea ice-ocean-atmosphere interactions across a broad range of spatiotemporal scales in MIZ has not been accomplished. Critical dynamical processes are not properly constrained in climate models and have resulted in inaccurate sea ice extent predictions [123]. *In-situ* field campaigns in MIZ (e.g., 68, 126, 132, 141), are too scarce to fully monitor the state of the flow field. Moreover, sea ice drift products, even those yielding high-quality datasets, employ sensors that are not suitable to retrieve information in MIZ. The inability to capture long-term observations and the urgency to gain a physical understanding of the processes driving the dynamics in MIZ motivates this investigation.

1.3 Dynamics in marginal ice zones

MIZ are critical momentum and heat transfer regions between the consolidated ice pack and the open ocean. The dynamics in these regions are complex. In general, sea ice drift is governed by the Coriolis and inertial forces, as well as atmospheric, oceanic and internal stresses. In Cartesian coordinates, the momentum balance equation of sea ice is defined as [31, 32]:

$$m\frac{D\mathbf{u}}{Dt} = mf\hat{\boldsymbol{\kappa}}\times\mathbf{u} - mg\nabla H + \boldsymbol{\tau_{ice}} + \boldsymbol{\tau_a} + \boldsymbol{\tau_w}, \tag{1.1}$$

where D/Dt is the material derivative, $\hat{\boldsymbol{\kappa}}$ is the unit vector normal to the surface, $\boldsymbol{u}$ is the sea ice velocity, f is the Coriolis parameter, m is the averaged sea ice floe mass per unit area, H is the sea surface dynamic height, g is the gravitational acceleration, $\boldsymbol{\tau_{ice}}$ is the stress due to the variation in internal ice stress, $\boldsymbol{\tau_a}$, $\boldsymbol{\tau_w}$ are the drag forces due to air and water stresses, respectively. Considering the rotational speed of Earth, Ω, and ϕ as the latitude, $f = 2\Omega sin(\phi)$.

In MIZ the Coriolis and surface tilt forcing can be neglected in MIZ [61]. Furthermore, typically documented low sea ice concentrations and a highly fractured sea ice cover imply that the rheological effects are relatively small. Hence, in free drift, the important spatiotemporal scales of ice motion are those originating from wind and ocean currents. In particular, the intrinsically strong sea ice-ocean interactions can drive sea ice to mirror meso/submeso-scale ocean eddies, even amid strong wind conditions. As such, sea ice tends to accumulate in convergence zones of vortices, i.e. eddy cores [47]. Even after days of strong wind conditions, remote sensing imagery still captures the signature of ocean eddies [38], whereby images illustrate the complexity of eddies and filaments (Figure 1.1).

In the northern hemisphere, a vortex with rotational direction in the clockwise (counter-clockwise) direction is identified as an anti-cyclone (cyclone). Important eddy formation mechanisms include hydrodynamic (barotropic and baroclinic) instabilities and the fluid-solid interactions occurring at the topographic boundaries in region [38]. One one hand, a barotropic instability is generated in a homogeneous and non-stratified water mass, where shear instabilities occur due to horizontal shear. On the other hand, a baroclinic instability

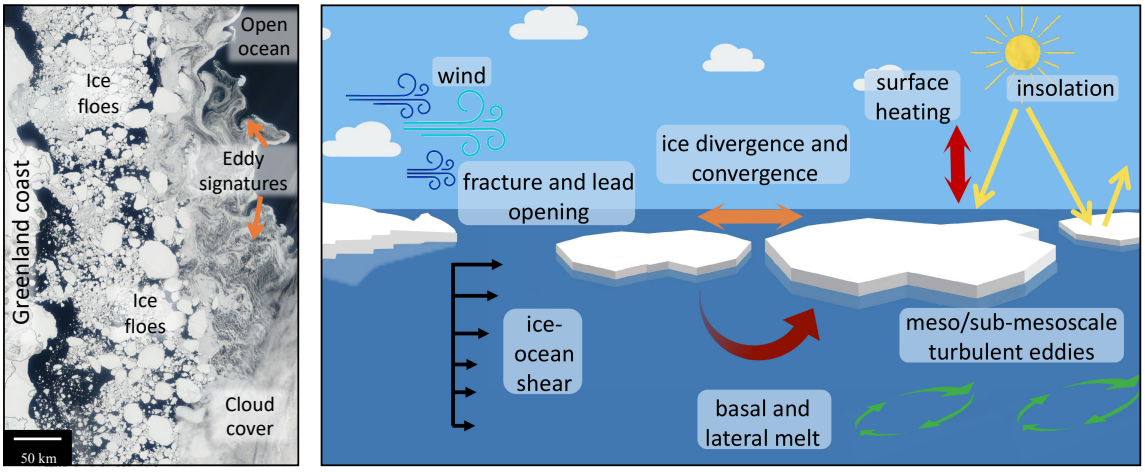

Figure 1.1: Marginal ice zone (MIZ). a) MIZ captured by satellite imagery. Sea ice displays complex motion due to its forcing mechanisms. The eddy signature of the underlying flow field is revealed by swirling ice and its accumulation in eddy cores. b) Key atmosphere, ice, and upper ocean processes of the Arctic MIZ.

emerges due to the vertical shear from isobaric and isopycnal layers. Along the ice edge, the interaction of the currents with bottom ocean topography is also a significant source of eddy formation [38, 134].

Characterizing sea ice interactions with the turbulent eddy field in MIZ remains difficult due to the inherent challenges of polar monitoring. A useful dimenseionless number is the Rossby number, R_o. R_o is employed as the criterion to separate the mesoscale from the submesoscale, and is defined as the ratio between inertial force and the Coriolis acceleration forcing due to the rotation of the Earth,

$$R_o = \frac{g'H}{f^2L^2} = \left(\frac{R_d}{L}\right), \tag{1.2}$$

where,

$$R_d = \frac{\sqrt{g'H}}{f}. \tag{1.3}$$

Here, g' is the reduced gravity, $g = (\rho/\rho_0)g$, where ρ is the density between the two layers. L is a a characteristic length scale. The Rossby radius of deformation, R_d, is representative of characteristic eddy length scale that is formed by geostrophic currents. In the Arctic Ocean, stratification is generally weak and the Rossby radius is significantly smaller than the mid-latitude oceans with $R_d = 30 - 50$ km [92]. Therefore, the small Rossby radius of deformation at high latitudes, $O(1)$ km, means that geostrophic eddies have small length scale ($2\pi R_d$). Even though coherent structures have been globally investigated through altimetry data, the presence of ice in the Arctic regions and the limited resolution of satellite sensors have challenged the ability to capture the wavelengths associated with these features within the meso/submeso-scale spatial range.

Oceanic eddies play a key role in the transport of nutrients, heat, salinity, and bio-geochemical properties [42, 74, 79, 140]. Recent studies have highlighted the role of meso- ($R_0 \sim O(-1)$) and submeso-scale ($R_0 \sim O(1)$) eddies, typically in the form of lateral density gradients, in modulating sea ice dynamics and vice versa. From satellite observations [38, 47], to *in-situ* field campaigns [71, 126, 141], and numerical idealized models [76], there is growing evidence of the important role of meso/submeso-scale turbulence in influencing sea ice transport. As such, sea ice transported by eddies can strongly affect the dynamics in the region. For example, sea ice drift can introduce positive feedback mechanisms that can result in accelerated sea ice melt [35]. The transport of sea ice and any induced lateral

freshwater transport can also enhance strong lateral buoyancy gradients that can affect the heat budget of the upper ocean [132]. Meanwhile, submesoscale flows can promote vertical heat and salinity fluxes in the water column [129]. In turn, these mechanisms can directly impact sea ice melt, formation, and dispersion rates [76, 129].

Understanding the multiscale features driving sea ice and the turbulent eddy field in MIZ is crucial to reach a system-level understanding of the Arctic. Advances in satellite monitoring technology has substantially improved the ability to acquire remote sensing observations to monitor polar regions, albeit with strong limitations in MIZ. In the following section, available sea ice drift products are presented, along with their limitations and the need for more comprehensive dynamical observations of sea ice to fully characterize the evolution of Arctic MIZ dynamics.

1.4 State of the art in sea ice drift monitoring

The recent advances in technology, the surge of satellite missions, and the development of new algorithms to acquire remote sensing observations have greatly improved the scientific capability to monitor polar regions. Remote sensing has proven to be a powerful tool, providing comprehensive information to monitor sea ice, validate models, and assimilate data. Some of the most commonly used and readily available sea ice drift products are listed in Table 5.1. The broad variability among these products exists due to the differences in the satellite- and air-borne sensors and the use of the different methodologies to calculate sea

ice drift, resulting in variations of spatial and temporal data resolutions [51, 55, 59]. Each product presents unique monitoring capabilities, with limitations.

Most commonly employed, Eulerian products detect sea ice motion by tracking the initial position of a sea ice parcel on a grid and calculating displacement vectors on subsequent satellite imagery. Eulerian products thus provide homogenous spatial and temporal data coverage. On the other hand, Lagrangian methods consist of analyzing a sequential record of positions of sea ice where the initial position of the ice parcel is not on a grid. These products allow for the identification of sea ice features. In both methods, sea ice displacement vectors can be calculated via two main ice motion quantification techniques: feature-matching (FM) and area-matching (AM). FM methods retrieve the motion of sea ice by identifying sea ice features on consecutive images [45]. On the other hand, AM algorithms take advantage of changes in intensities within the grid cells of consecutive images. Each grid cell is then analyzed via cross-correlation. The grid displaying the maximum cross-correlation (MCC) coefficient is identified and the displacement of sea ice within grid cells is quantified. Although robust, the technique fails where rotation and deformation of sea ice impede a correct intensity cross-correlation calculation [53]. In MIZ, most sea ice tracking algorithms fail to produce accurate results given the high vorticity and deformation rates of the sea ice field. Many products, including the Medium Resolution Sea Ice Drift product, the L3 Daily Brightness Temperatures, Sea Ice Concentration, Motion & Snow Depth Polar Grids product, and the Global high-resolution SAR sea ice drift product use MCC techniques to retrieve sea ice motion.

The quality of a given sea ice product mainly depends on the acquisition platform of the sensors being used. In general, the orbital tracks of the network of satellites are too sparse to derive sea ice fields at a sufficiently high temporal and spatial resolution as is required to resolve small-scale features of the sea ice drift field. This is the case of the Global Low Resolution Sea Ice Drift, which employs Special Sensor Microwave Imager/Sounder (SSMIS), Advanced Scatterometer (ASCAT), and Advanced- Microwave Scanning Radiometer 2 (AMSR2) sensors. The product provides sea ice concentration metrics, sea ice extent, and sea ice drift fields in a coarse 62.5 km grid and a 48 hr temporal resolution [59]. Another low-resolution product includes the Arctic Ocean Sea Ice Drift Reprocessed, which combines Lagrangian displacement data from AMSR, ASCAT, Special Sensor Microwave Imager (SSM/I), and Quick Scatterometer (QUICKSCAT) to quantify sea drift fields (31.25 km). Data from this product is not available over the summer periods due to the sensors' sensitivity to atmospheric water vapor, ice, and snow surface properties [27].

At moderate resolutions, one of the most popular products used to monitor the sea ice field in the Arctic is the Medium Sea Ice Drift product. This product employs Advanced Very High Resolution Radiometer (AVHRR) optical and infrared (IR) data to produce a sea ice drift field in a 20 km grid [19]. The National Snow and Ice Data Center (NSIDC) sea ice drift product provides one of the most comprehensive sets of Eulerian ice motion products for the Arctic Ocean by combining the Scanning Multi-channel Microwave Radiometer (SMMR), Advanced Microwave Scanning Radiometer for Earth Observing System (AMSR-E), SSM/I, SSMIS, AVHRR, as well as sea ice buoys and wind data. This product produces daily sea

ice motion vectors with a resolution of 25 km. However, it needs large areas of open ocean and fails in regions where both land and ocean are present [136].

In recent years, products derived from Synthetic Aperture Radars (SAR) have proven to be a reliable tool to track sea ice motion, owing to the launch of Sentinel-1A/B in 2016. Starting in 2018, SAR-derived products have provided big publicly available data at moderate-resolution (e.g., the 10 km sea ice drift fields from the Global High-Resolution SAR Sea Ice Drift product) [20]. In addition to these products, product generated at the Alaska Satellite Facility, MEaSUREs, offers Lagrangian sea ice trajectories and Eulerian velocity fields derived from eleven years of uninterrupted, three-day radar snapshots of sea ice from the Radarsat-1 satellite (1995-2012) and four years from the Envisat satellite (2008-2012). Unfortunately, the MEaSUREs sea ice drift product covers only half of the Arctic and the Antarctic poles [50, 63]. The sampling interval of the MEaSUREs sea ice drift product ranges from 1.5 h to 15 days. Similar to other products, MEaSUREs addresses its uneven temporal sampling by interpolating its measurements. As such, the motion at the meso/submeso-scale range is not properly resolved.

Optical imagery, namely AVHRR and Moderate Resolution Imaging Spectroradiometer (MODIS), represent the longest records of Earth ever compiled. The extensiveness of these datasets allows for the exploration of the evolution of the sea ice field over the years. The MODIS platform has provided a large number of Earth-monitoring products. However, due to the limitations of visual imagery in regards to clouds and illumination, sea ice studies often employ only a small sample of images with minimal cloud imprint (e.g., 125). Despite

Table 1.1: Available sea ice drift products derived from a variety of *in-situ* and remote monitoring sensors.

Program	Sensors	Products	Spatial/Temporal Resolution	Availability	Season
Global Low Resolution Sea Ice Drift	SSMIS, ASCAT, AMSR-2	concentration, extent, drift	62.5 km / 48 hrs	2009 - present	winter and summer
Arctic Ocean Sea Ice Drift Reprocessed	ASCAT, QUICKSCAT AMSR, SSM/I	drift	31.25 km / daily, weekly, monthly	1999 - 2020	winter
L3 Daily Brightness Temperatures, Sea Ice Concentration, Motion & Snow Depth Polar Grids	AMSR-E, AMSR2	brightness temperature, concentration, snow depth, drift	12.5 km / 1, 2, and 5 days	2012 - present	all year
AMSR-E/Aqua Daily L3 Sea Ice Drift Polar Grids	AMSR-E	drift	6.25 km / 5-day average	2011	summer
NSIDC Sea Ice Drift	AMSR-E, AVHRR, SMMR, SSM/I, SSMIS, NCEP/NCAR winds, drifting buoys	drift	25 km / 24 h	1978 - present	all year
Medium Resolution Sea Ice Drift	AVHRR	drift	20 km / 24 h	2014 - present	all year
Global High-Resolution SAR Sea Ice Drift	SAR	drift	10 km / 24 h	2018 - present	all year
MEaSUREs	SAR	deformation, age thickness, drift	10 - 20 km / 3 days	1996 - 2012	all year
Baltic Sea - SAR Sea Ice Thickness and Drift	SAR	concentration, thickness, drift	0.5 km / 24 h	2018 - present	winter

these limitations, some Arctic monitoring products are available, including snow cover MOD10A2/ MYD102A2 and sea ice extent MODIS MOD29/ MYD29 [111]. However, to date, no automatic sea ice drift measurements from MODIS imagery exist. The extensive MODIS dataset has the potential to produce a comprehensive time-series study of sea ice extending the twenty-first century, incomparable to any other SAR-based product.

1.5 Research objectives

This dissertation is devoted to the understanding of the evolution of the sea ice drift field in the Arctic MIZ. The lack of remote sensing tools to harness information of the sea ice field in these regions motivated this investigation. The main foal is to develop a sea ice detection algorithm designed to acquire measurements in MIZ. This new observational tool identifies and tracks sea ice in polar regions where dynamical measurements are sparse. On one hand, the decision to employ MODIS optical satellite imagery presented a unique opportunity to evaluate the variability of sea ice drift over the last two decades due to the extensiveness of the MODIS mission. On the other hand, optical imagery is often abated by cloud coverage and illumination changes. In this work, image processing techniques and FM methods are employed to develop a tool capable of tracking sea ice in MIZ despite cloud coverage, complex sea ice motion, and high sea ice deformation rates. The region south of Fram Strait along the coast of eastern Greenland was chosen to develop and validate this tool. The location was ideal because the region's strong winds and mean current dictated a year-round south-bound mean flow. As such, most of the ice was expected to drift southwards, which

simplified visual inspection efforts when developing the tracking algorithm. It is important to highlight, however, that the sea ice tracking algorithm is capable of identifying and tracking sea ice in any MIZ notwithstanding the mean flow direction.

The second research objective of this investigation is the compilation of sea ice characteristics and kinematics into a unique sea ice database. The developed methodology successfully retrieves geometric parameters including the perimeter, major and minor axes of an ellipsoid matching second-moment of inertia as the ice floe, centroid position, and surface and convex areas of identified sea ice floes. Moreover, relevant kinematic parameters include Lagrangian trajectories, angular velocities, and monthly and seasonal Eulerian velocity fields. These parameters were extracted from MODIS imagery acquired from 2003 to 2020.

The scope of this work is the thorough investigation of the sea ice field from the calculated sea ice dataset. This endeavor consists of assessing the role of atmospheric and oceanic forcing on ice floe motion. The results elucidate the feasibility of identifying meso/submeso-scale eddies from satellite-derived sea ice drift fields with the long-term goal of developing a new tool to characterize the oceanic turbulent eddy flow field. The eddies identified from sea ice observations are characterized based on their size, spatial patterns, and temporal variability.

The third objective of this investigation consists in quantifying the interannual variability of sea ice drift within the past two decades. One of the most salient consequences of rising atmospheric and oceanic temperatures is the registered drastic changes in the Arctic climate

system. The extensive database of sea ice Lagrangian measurements extends throughout the 21^{st} century, allowing for an unparalleled long-term analysis of the MIZ sea ice evolution.

Finally, the last objective of this investigation is to employ sea ice as parcels subject to the ocean surface forcing to analyze the topology of the underlying flow field. For the first time, Lagrangian trajectories of sea ice derived from satellite imagery are employed to measure sea ice dispersion statistics. The high-latitude turbulent oceanic eddy field is inherently challenging to observe due to the difficulty associated with capturing coherent structures corresponding to Rossby deformation radii in ice-covered regions. As such, this new sea ice analysis tool provides a unique approach to employ readily available data to characterize the processes driving the dynamics in regions where field data is difficult to obtain.

Chapter 2

Ice Floe Tracker: an algorithm to automatically retrieve sea ice drift from moderate-resolution satellite imagery

2.1 Introduction

Historically, ice motion has been quantified via Lagrangian and Eulerian methods. Lagrangian methods often consist of analyzing a sequential record of positions of on-ice buoys. With over 700 buoys deployed through the International Arctic Buoy Program since 1991, buoy trajectory measurements have provided long-term information regarding the dynamics of sea ice in the Arctic (e.g., 99, 113, 131, among others). However, Lagrangian analysis of buoy

trajectories does not provide uniform sampling due to constraints in spatial and temporal coverage of the drifting instruments.

Eulerian methods have been primarily used to analyze remote sensing observations, which allow for uniform spatial and temporal coverage of sea ice motion [51]. Time series of airborne or satellite imagery of sea ice are superimposed on a grid, and displacement vectors are calculated via two main ice motion quantification techniques: area-matching (AM) and feature-matching (FM). AM techniques fail to track ice floes where rotation and deformation are present [53]. On the other hand, FM result in inhomogeneous sea ice motion fields given that features are not evenly distributed throughout the image [45].

By adopting both AM and FM ice motion retrieval methods, studies done with microwave, infrared, and visible space- and airborne-instruments have provided continuous long-term observations to monitor sea ice motion, as introduced in Chapter 1.

Remote sensing imagery from active sensors has been commonly analyzed using AM and FM techniques, for example, active scatterometer data from NASA Scatterometer (NSCAT) and NASA's Quik Scatterometer (QuikSCAT) [27, 30, 64, 155]. More predominant, however, has been the use of Synthetic Aperture Radars (SAR) to quantify sea ice drift given the high resolution of the data as well as its independence from uneven illumination and atmospheric conditions. The development of algorithms employing SAR imagery dates back to the first Earth-orbiting satellite designed for remote sensing of the Earth's oceans, SeaSat, [24] and the European remote-sensing satellite ERS1 [55, 130]. More techniques to identify sea ice employing SAR imagery include studies by 17, 44, 53, 78, 86, 87. One advantage of SAR

is that it provides optimal resolution for the detection of small features over large regions (especially over the ice pack, where high ice concentration is encountered), and thus feature analysis from SAR imagery proves efficient due to the rich texture provided by these sensors [11]. However, due to inherent speckle noise from the backscattering microwave signal, SAR imagery often requires further filtering and ice features can be affected [60]. In addition, the incidence angle at which the backscatter signal is measured and the type of the target surface (ice or open water) alter this measurement. A correction factor must hence be taken into consideration in the majority of algorithms (e.g., 150).

Data from visible sensors are not affected by speckle noise and allows for sea ice-water discrimination at the pixel level, which can prove beneficial when analyzing regions under dynamic conditions with relatively low ice concentration (such as in the marginal ice zone). However, it has lower resolution than SAR and is affected by atmospheric conditions. Moderate Resolution Imaging Spectroradiometer (MODIS) has resulted in the longest continuous daily global moderate-resolution satellite observation record of Earth ever compiled [147]. Since the launch of the Earth Observing System Terra and Aqua satellites (1999 and 2002, respectively), the comprehensive database of MODIS imagery has been a good resource to monitor sea ice at resolutions ranging from 250 m to 1 km [95]. Due to the limitations of visual imagery in regards to clouds and illumination, sea ice studies often employ only a small sample of images with minimal cloud imprint (e.g., 125). To date, no automatic sea ice drift measurements from MODIS imagery exist.

In this Chapter, an algorithm for automatic identification and tracking of ice floes is presented. The algorithm provides sea ice drift and velocity information by processing MODIS imagery. Our technique integrates three main modules: image processing, feature identification, and ice floe tracking. The image processing module of the ice floe tracker effectively minimizes noise due to uneven illumination and cloud coverage, while increasing the contrast between ice floes and ocean water. The ice floe matching module allows the retrieval of Lagrangian trajectories of ice floes with length scales ranging from 8 to 65 km in a region where the annual mean of the Rossby radius of deformation, R_0, is 5 km [92], and the eddy radii range from 15 to 35 km [72].

This chapter is organized as follows. After a description of the database and study area presented in Section 2.2, the structure of the algorithm is explained in Section 2.3, followed by a discussion on its performance in Section 2.4. Acquired measurements and derived products are presented in Section 2.5. Finally, Section 2.6 provides a summary along with an outlook of improvements and potential applications.

2.2 Data and study area

2.2.1 Data: MODIS images

Moderate-resolution (250 m) georeferenced MODIS imagery was employed. The images were downloaded from the platform NASA Worldview[1], which implements the product

[1]NASA: https://worldview.earthdata.nasa.gov

MODIS Level 1B 250M to produce 8-bit GeoTiff images. The images are displayed on an Arctic polar stereographic projection (WGS 84/NSIDC Sea Ice Polar Stereographic North 70° N for minimal distortion at the poles and the marginal ice zone). In particular, two digital color images are used: Corrected Reflectance True Color and Corrected Reflectance False Color. Each of these images is composed of three bands corresponding to RGB channels, namely band 1 (620-670 nm, 250 m), band 4 (545-565 nm, 500 m), and band 3 (459-479 nm, 500 m) for the former and band 7 (2105-2155 nm, 500 m), band 2 (841-876 nm, 250 m), and band 1 (620-670 nm, 250 m) for the latter. Given that the high-resolution bands, i.e., bands 1 and 2, are used to sharpen the ones with lower resolution, digital images have an effective resolution of up to 250 m. In this study, the RGB intensity values of the True Color images are used as reflectance data to extract ice features, while False Color images are used to differentiate between ice and clouds.

The EOS-NASA satellites acquiring the images (Terra and Aqua) follow a sun-synchronous near-polar orbit with a period of 100 min [147]. Hence, each satellite passes over any given latitude at approximately the same local time during each orbital pass, maintaining a consistent angle of sunlight upon the Earth's surface, critical in assessing time-series data. Thus, as Terra and Aqua image their swath at about the same sun time during each pass, a minimal variation of solar illumination is achieved due to a consistent orbit and sun angle. Within a season, the majority of changes in illumination observed in the images originate from variations in atmospheric conditions (i.e., cloud imprint) as well as shifts in the satellite tracks. As the sensors capture sun reflectance data, spring and summer

are the optimal seasons in which sea ice measurements can be retrieved in the Arctic. This study covers a period of the 2017 spring season spanning from 20.04.2017 to 05.06.2017.

While in orbit, each satellite acquires an image (2340×2030 km^2) every 5 min along its track [146]. Worldview provides a daily real-time global image composed of a single revisit cycle for each satellite (an image from Terra's descending-southbound orbit and another from Aqua's ascending-northbound orbit). From these global images, the study region is selected (Figure 2.1). Although each satellite produces a global image daily, the repeat frequency does not occur along the same ground track, resulting in a slightly shifted satellite track every day with a 16-day repeat cycle. As a result, the snapshot of the study region can be composed of one or two satellite passes (100 min apart) depending on the satellite track. For the study period, 21% of the images are composed of two satellite passes (hereon referred to as composites). The advantage of working with this data set rather than individual images is that these images have been color-calibrated, geolocated, and processed to eliminate geometrical distortions (e.g., bow-tie and stretching) as well as atmospheric effects (e.g., Rayleigh scattering).

Daily images from both Aqua and Terra were sorted to produce a comprehensive data set from which to retrieve ice floe trajectories and velocities. Due to the differences in the revisit cycle of each satellite, the time difference between images, Δt, ranges from 20 to 90 min according to the orbit track timestamp of each satellite.

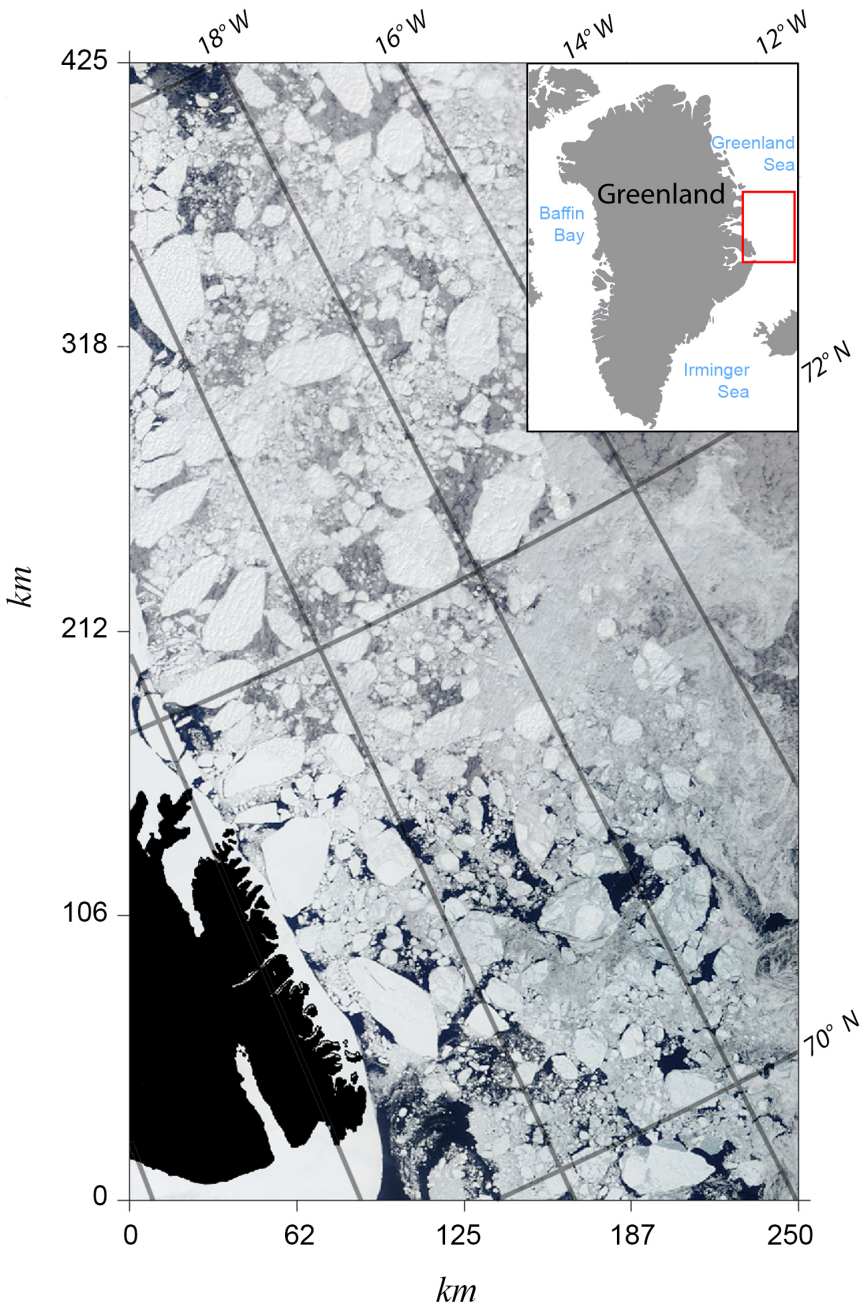

Figure 2.1: Study region: eastern Greenland. Representative MODIS True Color image corresponding to 06.05.2017 (displaying bands 1, 4, and 3). The grey grid indicates latitudes and longitudes, land is shaded black. Note that the study region is smaller than a satellite swath. Inset map shows the geographical location of the study area.

2.2.2 Study area: eastern Greenland coast

The study area is located along the eastern coast of Greenland (Figure 2.1) and is characterized by strong winds [39] and the East Greenland Current (EGC). The majority of the ice exported from the Arctic exits through Fram Strait, the largest and most concentrated meridional sea ice flow in the world [139]. The EGC, as the only major southward flowing current in the Greenland Sea [148], transports over 90% of this ice [114]. The seasonal sea ice cover allows for the identification of ice floes under dynamical conditions in the study region. Furthermore, the EGC is important both locally and globally as a link between the Arctic Ocean and the North Atlantic Ocean. Small variations in freshwater supplies, such as freshwater spreading outside the EGC into the Greenland Sea, can alter the convective overturning of water masses and weaken the thermohaline circulation [1].

2.3 Automatic algorithm for ice floe tracking

The developed adaptive algorithm is composed of three main stages: image processing (Section 2.3.1), feature identification (Section 2.3.2, and tracking (Section 2.3.3). These routines include processing functions involving numerical constants and thresholds that have been set according to statistical analysis of the whole image sequence (total of 94 images). The robustness of these parameters was tested by processing both a larger domain within Fram Strait for the 2017 spring season and the marginal ice zone (MIZ) within the Beaufort Gyre for the spring and summer seasons for years spanning 2005 to 2018 (not presented in

this study). These analyzes proved successful despite the very different dynamical properties in these regions. Hence, it is unlikely that additional tuning is required to analyze other regions within the Arctic. Nonetheless, the values of all the thresholds imposed are outlined in the pertaining sections. All modules in the algorithm are implemented in Matlab using a text-based interface to operate the Image Processing Toolbox.

2.3.1 Image processing routine

Imagery derived from optical sensors is affected by atmospheric processes. The first modules in the algorithm automatically minimize the effects of uneven image illumination caused by cloud coverage. Routines to enhance ice-water discrimination are then implemented, followed by ice floe segmentation and feature identification. All of these processes are laid out in the flow chart of Figure 2.2, with representative products of the main stages of the algorithm presented in Figure 2.3.

Pre-processing

Initially, both RGB Reflectance False Color (RGB channels corresponding to bands 7, 2, and 1, respectively) and True Color images (RGB channels corresponding to bands 1, 4, and 3, respectively) are automatically downloaded from the open-access Earth Observing System Data and Information System (EOSDIS) Worldview platform and loaded into the module. A

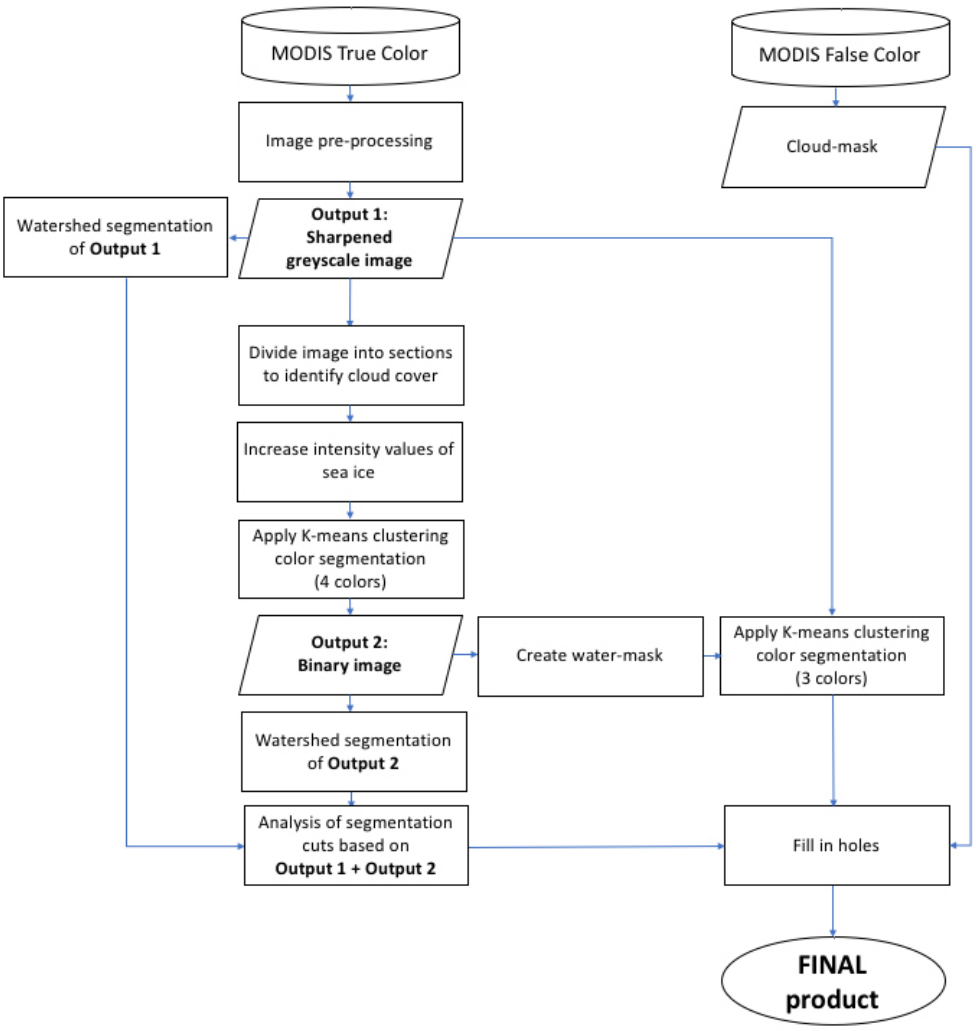

Figure 2.2: Image processing flowchart. Overview of the algorithm developed to process MODIS imagery for ice floe identification. Outputs 1 and 2 refer to panels c) and e) of Figure 2.3, respectively.

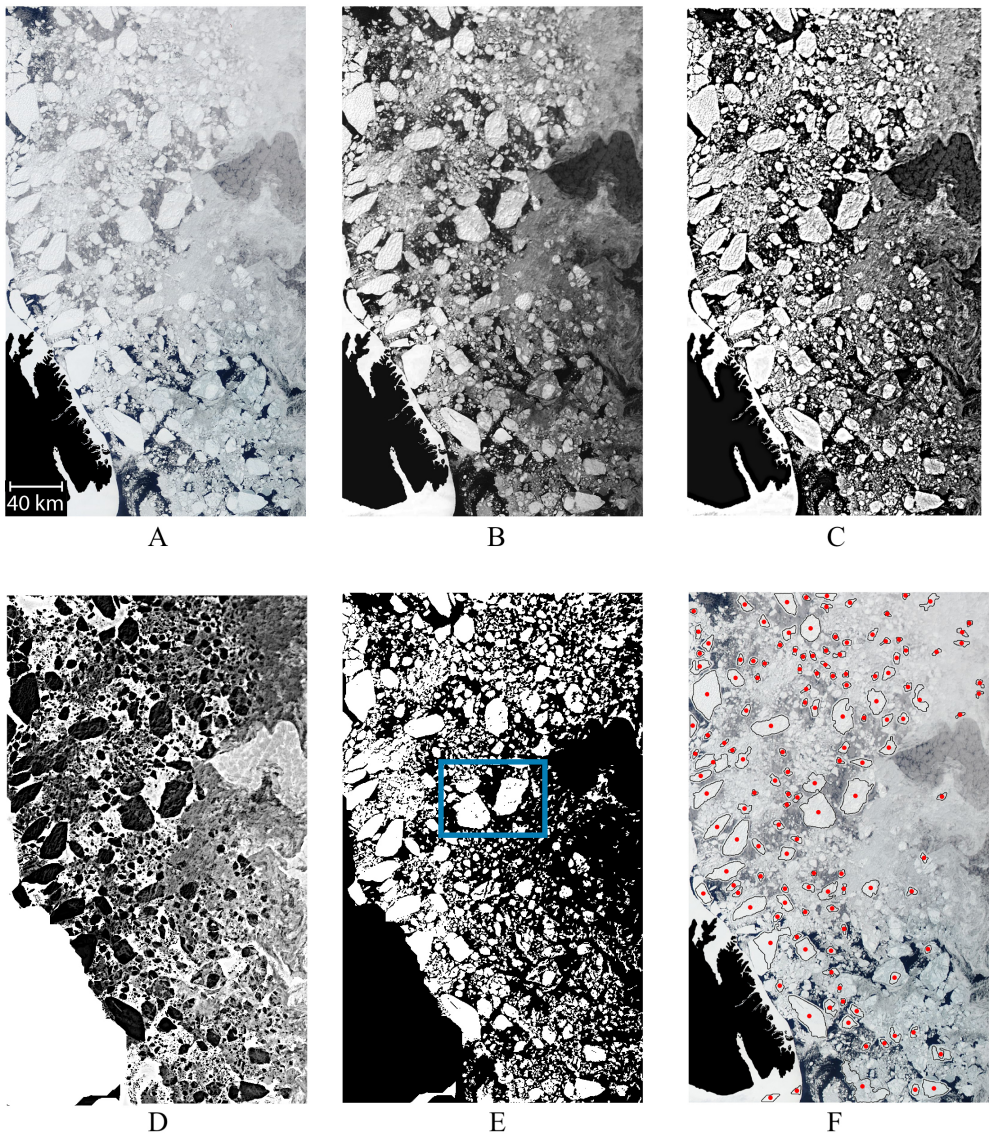

Figure 2.3: Ice floe tracker. Panels are representative of outputs at main stages of the algorithm: a) unprocessed MODIS RGB True Color image, b) image after cloud minimization, c) sharpened image, d) image after ice-water discrimination; note that colors are reversed for clarity in the presentation, e) binary image after K-means color segmentation, and f) segmented ice floe contours superimposed on the corresponding unprocessed True Color MODIS image. The geometric centroids of identified ice floes are marked with red on the bottom rightmost panel.

land mask is then superimposed and dilated 12 km into the ocean to reduce computational time and minimize identification errors of landfast ice.

Although a cloud mask product (MOD35) is available, the algorithm does not employ it to avoid removing regions where ice floes can be potentially retrieved. Instead, reflectance thresholds were employed to discriminate sea ice from clouds and open water [2]. False Color RGB images are first analyzed to distinguish snow and ice from clouds. Since snow and ice are very reflective in the visible part of the spectrum (band 1), and absorbent both near infrared (IR) (bands 2) and short-wave infrared (band 7), False Color RGB images display ice and snow with blue, and clouds with white color (Figure 2.4). Furthermore, by analyzing the red channel of the image (band 7) separately from the other channels, the cloud imprint is readily observed (Figure 2.4.b).

Following statistical analysis of the images, pixel thresholds were set to create a cloud mask at each time step. First, a preliminary mask is created by identifying pixels exceeding an intensity value, l_1, of 110 in channel 1 (band 7), since, unlike ice, clouds appear bright near IR. The preliminary mask is then corrected for pixels including discernible ice floes underneath clouds by selecting pixels with $l_1 < 200$ in the red channel (band 7), and also $l_2 > 190$ in the green channel (band 2). Also, pixels with a ratio of l_1/l_2 ranging from 0 to 0.75 were found to contain underlying ice floe features that could be resolved with the presented algorithm. The final cloud mask is generated by subtracting pixels from which ice floes could be retrieved from the preliminary cloud-mask (Figure 2.4.d).

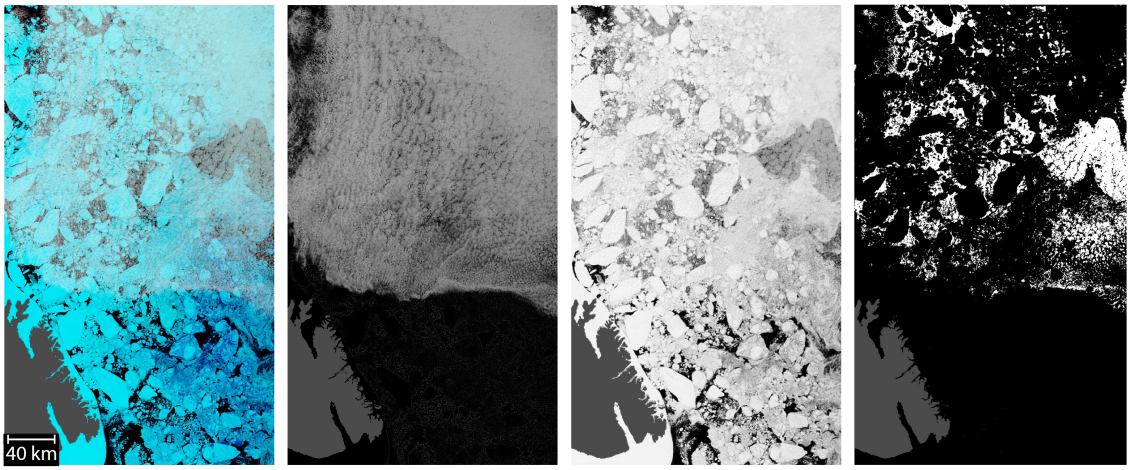

Figure 2.4: Reflectance False Color MODIS image. a) Representative False Color image used to identify clouds, with RGB channels corresponding to bands 7 (2105-2155 nm), band 2 (841-876 nm), and band 1 (620-670 nm), respectively. b) Band 7 of the RGB. c) Band 1 of the RGB. d) Computed cloud mask of the region. The land is shaded in gray in all images.

True Color RGB images are processed to identify ice floes. To minimize the effects of uneven image illumination due to clouds, an intensity enhancement method, known as histogram equalization, is adopted for its effectiveness in removing thin clouds in visible satellite imagery [137]. This technique is based on the premise that cloudless images have more contrast than those taken on cloudy days [127]. Histogram equalization takes the histogram of the input image (Figure 2.5.a) and aims to evenly distribute the intensities over the whole intensity domain so that these span over a wider range on the intensity scale. To accomplish this, the probability density function (PDF) of the RGB True Color image is computed:

$$PDF(l) = \frac{n_l}{N}, \tag{2.1}$$

where n_l is the number of pixels at every intensity l, and N is the total number of pixels in the image. The cumulative distribution function (CDF) is then obtained by summing all of the probabilities over the entire intensity domain:

$$CDF(l) = \sum_{i=0}^{l} PDF(i). \tag{2.2}$$

Ideally, this function would map the input histogram (e.g., Figure 2.5.a) into an image with an equal number of pixels at each intensity level. However, the intensity values in real digital images are discrete and final; hence, this transformation cannot produce a perfectly uniform output histogram. Nonetheless, mapping the input image via its CDF modifies the dynamic range of the image such that its intensities are better distributed [119]. To that end, the CDF value at every l is multiplied by the maximum intensity value, l_{max} =255:

$$T(l) = CDF(l) * 255. \tag{2.3}$$

This is performed using all RGB channels of the True Color image, producing a flatter and more evenly distributed histogram (Figure 2.5.b). As a result, images have maximum contrast [144], and the noise due to thin clouds is reduced. The equalized True Color RGB image is subsequently converted to greyscale (Figure 2.3.b). The effect of the histogram equalization is evident in the central region of Figure 2.3.b, where the thin haze produced by clouds is reduced, and ice floes are better resolved than in the original image (Figure 2.3.a).

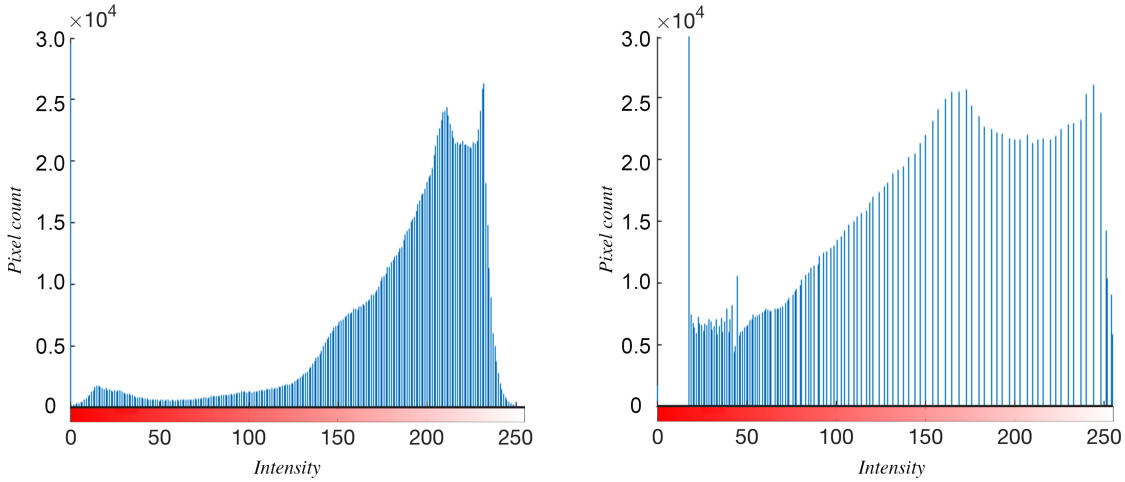

Figure 2.5: Histogram equalization. Distribution of intensity values of the red channel of a representative True Color MODIS image a) before and b) after histogram equalization is performed.

Ice-water discrimination

After image pre-processing, the next module in the algorithm increases the contrast between ice floes and seawater (e.g., bright objects and dark background, respectively, in Figure 2.3.b). By enhancing the difference in intensities between sea ice and ocean pixels, ice floes can then be readily segmented and identified.

First, the algorithm sharpens the images by subtracting a blurred copy (L). Blurred images are generated by imposing a Gaussian function (G) on each pixel of produced copies,

$$L(x, y, \sigma) = G(x, y, \sigma) * n(x, y, l) \ , \tag{2.4}$$

where σ is the standard deviation of the Gaussian distribution that effectively determines how much blurring will be imposed. A value of $\sigma = 2$ was prescribed on a 10-pixel radius

based on empirical analysis of the images. As a result of this operation, ice floe contours are better distinguished from seawater (e.g., compare Figure 2.3.b to Figure 2.3.c).

Next, the algorithm selectively identifies pixels containing sea ice and increases their intensities to brighten ice floes in the sharpened images. Due to cloud overcast and residual noise from the image pre-processing routine, artifacts may appear as shadows and color gradients on the surfaces of some ice floes (e.g., mid-section of Figure 2.3.c). To better discern ice-pixels, sharpened images are divided into nine subsections, and band 7 (short-wave infrared) is analyzed to evaluate the presence of clouds (e.g., Figure 2.4.b). If the number of bright pixels with intensity value $l \geq 110$ (indicative of bright clouds) covers less than 20% of any given subsection, the standard deviation of pixels with high intensities ($\sigma_{l>110}$) is quantified. If $\sigma_{l>110} \geq 100$, the intensity of every pixel with $l > 125$ in any given subsection is increased by 30%. This enhances ice floe-water discrimination while minimizing the gradients within the surface of ice floes. On the other hand, if cloud coverage on the subsection is extensive, only pixels with intensity $l >175$ are brightened. This results in images with a dark water background and bright ice floes (e.g., Figure 2.3.d, which for ease of visualization is shown with black and white reversed).

Once the resulting greyscale images have been enhanced to increase intensity differences between sea ice and water, their grey levels are used to perform a color-based segmentation routine via K-means clustering [73] to automatically discriminate ice floes from seawater. The grey shades are classified based on the chromatic similarities between pixels containing sea ice and water. To perform this task, a total number of four clusters were defined to

partition the images and identify ice floes. The algorithm groups all of these in the same cluster since most of the pixels pertaining to ice floes have similar chromatic values. From the four clusters generated, the cluster containing the ice floes is automatically selected by identifying pixels with low intensities ($l \approx 0$) in band 7 (e.g., Figure 2.4.b), and high intensities ($l \approx 255$) in band 1 (e.g., Figure 2.4.c.) By selecting low l values in band 7, pixels with artifacts due to clouds are effectively discarded, while the selection of high l values in band 1 isolates sea ice, which is highly reflective in the visible part of the spectrum. Once the ice floe cluster is identified, the image is binarized by assigning the pixels in this cluster value of one, while the rest of the pixels (the water-mask) are assigned a value of zero. Finally, objects with a surface area less than 1 km^2 are filtered from the image to eliminate ice floes with geometrical parameters that cannot be properly resolved (e.g., Figure 2.4.e).

Segmentation

Incorrect identification of adjacent ice floes as a single over-sized floe can occur if the individual contours of neighboring ice floes are not fully resolved (e.g., ice floes enclosed by the blue outline in Figure 2.3.e). Ice floe segmentation is performed to minimize such identification errors by identifying intensity valleys and applying a watershed segmentation to each image. To this end, bordering ice-pixels are identified and connected via a watershed function by calculating the inverse Euclidean distance of each ice-pixel to the nearest water-pixel, and recognizing that pixels within the center of the ice floes have larger absolute distances to water pixels than those at the contour [36]. The watershed function is applied to

both ice-water discriminated images (e.g., Figure 2.3.d), and binary images that have already been processed via K-means color segmentation (e.g., Figure 2.3.e) to reduce any artifacts due to incorrect segmentation. Given that one set of images is formed of greyscale images, while the other set is composed of binary images, the inverse Euclidean distance metric results in different intensity valleys. Retrieved ice floe divisions that align in both images are thus the only ones imposed.

Watershed segmentation allows for ice contour identification without distortion. However, this function must be combined with the following image operations to identify ice floes as single objects correctly. First, the color-based segmentation routine employing K-means clustering is performed on sharpened images taking into account the water-mask produced during the ice-water discrimination module (considering three-color clusters). The cluster containing the ice floes is automatically selected, and binary images are produced holding the rest of the parameter space constant. The computed watershed segments are also applied, and artifacts are filtered by removing objects with areas smaller than 3 km^2. Second, single white pixels connecting large groups of white pixels are removed, followed by an erosion-and-dilation operation, whereby the ice floes are shrunk in size by 4 pixels and then expanded by 4 pixels again, to eliminate gaps in ice floe contours.

Holes can appear on the surface of ice floes covered by clouds. Clusters of dark pixels are identified to correct this issue. If these clusters (irrespective of the number of pixels) are entirely surrounded by bright pixels, dark pixels within the cluster are reassigned an intensity value of one, thus filling in the holes on the surfaces of ice floes. Finally, to generate the

final product of the image processing routine (e.g., Figure 2.3.f), the cloud-mask produced at the beginning of the algorithm (e.g., Figure 2.3.d) is applied to each filled-in image.

2.3.2 Feature identification

Once segmented images are obtained, ice floes are recognized as objects, and their geometrical parameters are calculated, including perimeter, major and minor axes of a circumscribing ellipsoid, centroid position, and surface and convex areas. The convex area is defined as the area of the smallest convex polygon enclosing an ice floe. The full suite of geometrical parameters is used to identify and track ice floes in subsequent MODIS images automatically. From the positions of tracked ice floes, displacement vectors are calculated together with sea ice velocities (taking into account image acquisition time differences).

Limiting thresholds on the size of retrieved ice floes are imposed to ensure the accuracy of the feature identification module, whereby information of ice floes with surface areas less than 44 km^2 or greater than 940 km^2 is discarded. The lower threshold is applied given that ice floes with areas below this cut-off cannot be reliably differentiated solely based on geometrical measurements. For instance, the standard deviation of geometrical parameters for ice floes with areas below 44 km^2 decreases by an order of magnitude compared to those above that limit, restricting accurate differentiation between neighboring ice floes. The maximum threshold, on the other hand, eliminates the identification of residual imprints of large atmospheric conditions as over-sized ice floes.

As a result of this module, the agglomerations of ice floes being resolved are vast, with length scales ranging from 8 to 65 km (e.g., objects with red markers in Figure 2.3.f). A database containing the geometrical parameters of all ice floes, together with their positions (provided both in polar stereographic and lat/lon coordinates), is generated and transferred to the tracking module.

2.3.3 Tracking

Ice floes are automatically tracked by: (1) comparing the geometrical information of ice floes within consecutive images, (2) finding potential matches by evaluating the percent difference in prescribed geometrical parameters between reference ice floes and their prospective pair based on empirically derived thresholds, and (3) selecting the best candidates based on the assessment of a similarity metric. As implemented, this analysis occurs in a multi-step process. The first step analyzes image pairs within a 24-hr window, while a second step repeats steps (1) through (3) within a 48-hr window. Given that the accuracy of the retrieved ice floe trajectories depends on the evaluation of geometrical parameters, identified ice floes that are too small to retrieve this information reliably are excluded from the tracking module (ice floes with length scales less than 8 km and surface area of approximately 44 km^2).

Before inspecting the geometrical parameters of ice floes within consecutive images, upper bounds on the distances traveled by drifting ice floes are imposed to improve computational time (Table 2.1). Displacement thresholds of 3.75 and 7.5 km were set for acquisition time differences of 20 and 90 min, respectively. For longer acquisition time differences,

Table 2.1: Restrictions on sea ice displacement applied to the multi-step matching module according to the time difference between potential ice floe matches.

	Δ t			
	20 min	90 min	24 hr	>24 hr
Displacement radius	3.75 km	7.5 km	30 km	60 km

displacement thresholds of 30 and 60 km were imposed for differences of 24 hr and >24 hr, respectively. High thresholds are imposed to avoid tuning these parameters when analyzing regions with different dynamical properties.

If the displacement thresholds are met, the geometrical parameters of ice floes within consecutive image pairs are examined. Potential matches are detected by identifying ice floe pairs that meet empirically derived bounds on the percent difference of major and minor axes, surface area, and convex area (Table 2.2). Given that measurable differences in these factors decrease with ice floe size, a lower tolerance is imposed on ice floes with areas less than 75 km^2 (resulting in a reduction of the percent difference of all parameters ranging from 30 to 35% compared to bounds imposed on larger ice floes). The numerical thresholds imposed throughout this module were empirically determined by trial-and-error analysis of the whole image sequence. The empirical method to select these thresholds consisted of manually tracking ice floes for a few days, while continuously measuring these parameters and their day-to-day differences. The value of the thresholds imposed to each parameter is an upper bound on the registered variability of each metric.

Table 2.2: Geometrical thresholds applied to the first and second passes of the ice floe tracker algorithm. Numerical values indicate the percent difference in geometrical parameters of evaluated ice floes from one trajectory point to the next (except for the surface area difference and the correlation coefficient).

Parameter	Threshold [%]	
	Ice floe area < 75 km^2	Ice floe area ≥ 75 km^2
Major axis	7	10
Minor axis	8	12
Surface area	18	28
Convex area	9	14
Surface area difference	18	24
$\Psi - S$ cross-correlation coefficient	0.7	0.7

Due to the resolution of the images, uneven illumination due to cloud overcast, and residual artifacts from the image processing module, the contours of identified ice floes can vary substantially, even during short periods of time. However, the geometrical parameters evaluated to match ice floes are not directly dependent on the accuracy of ice floe contour detection. The major and minor axes are defined by circumscribing an ellipsoid around an ice floe, which has the same second-moment of inertia as the ice floe. Hence, the length of both major and minor axes are robust metrics despite ice floe contour variability. For this reason, strict bounds were considered for the major and minor axes, as seen in Table 2.2. Surface and convex areas are slightly affected by the accuracy of ice floe contour detection, which justifies more lenient thresholds. An example of the evaluation of geometrical parameters to

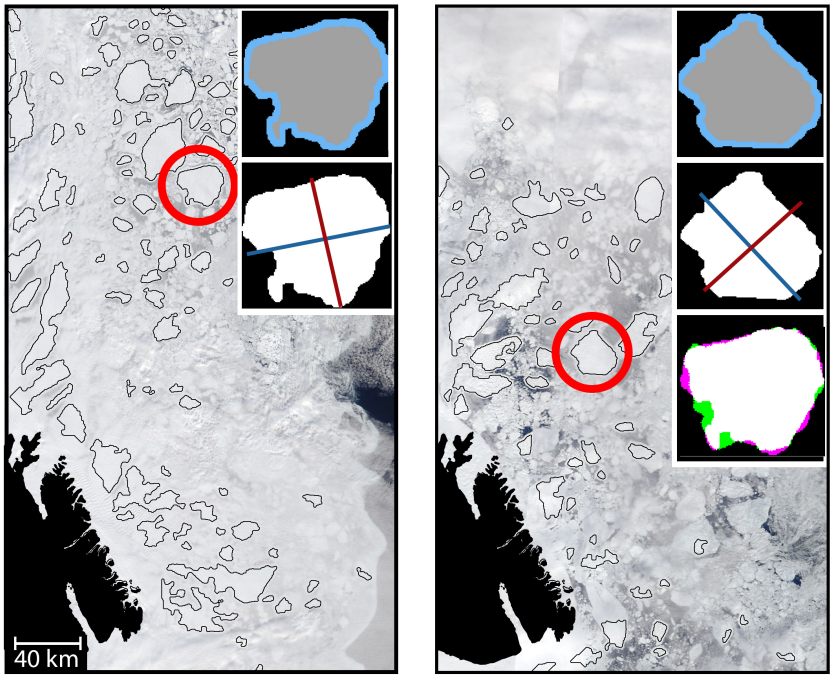

Figure 2.6: Ice floe identification via evaluation of geometrical parameters. The circled ice floe is identified continuously for nine days. The position of the ice floe is presented both a) at the beginning (30.04.2017) and b) at the end (08.05.2017) of the automatically retrieved trajectory. The contour of the ice floe is delineated with light-blue, and its area is filled in with gray. The major and minor axes of the circumscribing ellipsoid are indicated by a red and blue line, respectively. The bottom inset of b) shows the ice floes rotated until aligned and superimposed against each other. Matching areas are shown in white, while the pink and green colors show misaligned regions.

retrieve an ice floe match is presented in Figure 2.6, illustrating an ice floe tracked during a 9-day period. Although the shape of this ice floe changes from day one to nine (Figures 2.6.a and 2.6.b, respectively), the tracking module successfully identifies the correct match based on evaluation of its geometrical parameters, notwithstanding large rotations.

Finally, two additional metrics are used to evaluate potential ice floe matches: surface area difference, and the $\Psi - S$ correlation coefficient (Table 2.2, below the dotted line). To calculate the surface area difference between a reference ice floe and its potential match,

both ice floes are superimposed, and the potential ice floe match is rotated about its center of mass until the area difference between the two is minimum (e.g., bottom inset of Figure 2.6.b). If the area difference between the superimposed ice floes is below 24%, the so-called $\Psi - S$ similarity metric is calculated for each ice floe. Ψ is defined as the angle between the tangent to the ice floe contour and the horizontal (calculated at regular intervals throughout the contour), while S is the arc length of the boundary traversed (evaluated at the same points throughout the contour) [78]. Once the $\Psi - S$ function is calculated, the normalized correlation coefficient is computed:

$$\rho(k) = \frac{\sum_{j=1}^{n} (\Psi - S)_1(j)(\Psi - S)_2(j-k) - \mu_1\mu_2}{\sigma_1\sigma_2}, \tag{2.5}$$

where the subscripts 1 and 2 refer to quantities pertaining to the reference ice floe and its potential match, respectively. Also, μ is the mean of the $\Psi - S$ function, σ is the standard deviation, k is the offset between correlation measures and n is the last point of the ice floe contour. A given pair is considered a final match if $\rho(k \approx 0) > 0.70$. If more than one potential ice floe match is being evaluated, the ice floe pair with the smallest percent differences in analyzed geometrical parameters (including superimposed matching area and the $\Psi - S$ correlation coefficient) is selected as the final match.

The first pass of the tracking algorithm analyzes consecutive image pairs with a time difference Δt ranging from 20 min to 24 hr, whereby heavy cloud cover can thwart continuous ice floe tracking. During the second pass (also referred to as *1-day skip* module), longer

trajectories can be recovered by applying the same analysis to a longer time series. By analyzing a total of five images spanning a 48-hr period, the *1-day skip* module successfully retrieves longer trajectories if ice floe identification was corrupted for up to 24 hr (one to four images of missing information). The process is better illustrated with the following hypothetical example, in which the first pass identifies ice floe *A* for days 1, 2, and 3. Its trajectory is then retrieved for days 1, 2 and 3 and velocity vectors can be computed for days 1 and 2 (considering ice floe displacements between image pairs 1+2 and 2+3, and the corresponding Δt between images). Suppose that excessive cloud coverage on day 4 impedes the continuous identification of ice floe *A* and, as a result, ice floe *A* is identified as a new ice floe *F* on day 5. The *1-day skip* module corrects this and relabels ice floe *F* as *A* while retrieving not only a longer trajectory (spanning days 1 through 5) for ice floe *A*, but also more comprehensive information regarding the ice floe velocity (given the retrieved image pair 3+5). The algorithm recognizes that the time difference between days 3 and 5 is 48 hr and assumes a linear drift to calculate the velocity vector. On average, this increases the number of points in a trajectory from 2 to 3 trajectory points. It is also important to comment that there are a total of two images per day (originating from each one of the EOS satellites). This is taken into consideration in the algorithm but omitted in this example for simplification. Similarly to the first pass, a displacement radius threshold is imposed during the *1-day skip* module, see the fourth column of Table 2.1). In addition, ice floe trajectories with a higher number of extrapolated positions from the *1-day skip* module than of retrieved

positions from the first pass are compared to those of neighboring ice floes (within a 30 km radius) to eliminate spurious trajectories.

2.4 Performance evaluation of the algorithm

Manual ice floe identification in unprocessed True Color RGB MODIS images (with a dilated land mask was performed to quantify the error associated with algorithm-derived products. This set of baseline images was selected such that a broad range of cloud-coverage conditions were included in the analysis (Figure 2.7). Manual identification of ice floes was open to human interpretation of contrast, intensity, and texture of the images, unavoidably making this process subjective to the discretion of the authors.

In general, good agreement between manually identified ice floes and algorithm results were observed. Both the shape and location of ice floes qualitatively matched manual selections everywhere except in regions with dense cloud cover. Differences in geometrical parameters between manually identified ice floes and the tracker output ranged from 1.7 ± 0.7 % to 4.9 ± 0.02 % (Table 2.3).

The mismatch between manually and automatically identified ice floes can be attributed to artifacts arising as a byproduct of the image processing module (e.g., ice floes within regions 1 through 5 in Figure 2.7). As a result of the implemented strategies to filter clouds, ice floes in certain parts of the images can be darkened, thereby reducing the number of identified ice floes (e.g., regions 1 and 2 in Figure 2.7). Also, although reflectance data were

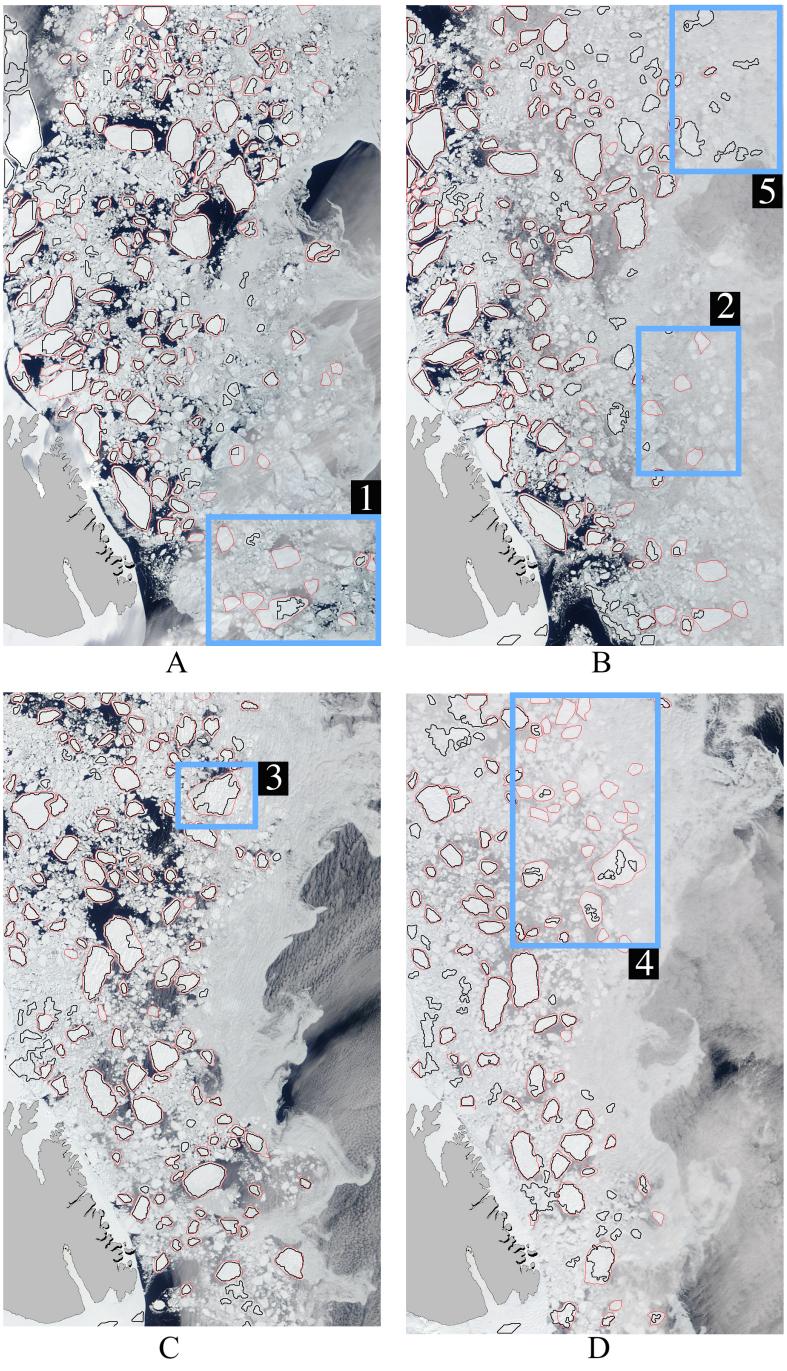

Figure 2.7: Evaluation of the algorithm. A superposition of raw MODIS images and algorithm-derived products (black outline) is presented along with manual ice floe identifications (red outline) for the following acquisition dates: a) 04.05.2017, b) 05.05.2017, c), 21.05.2017, and d) 24.05.2017.

Table 2.3: Identification error of geometrical parameters. Identification errors are taken as percent differences between manual and automatic results.

Parameter	Identification error
Major axis	4.1 ± 2.1
Minor axis	4.9 ± 0.02
Surface area	1.7 ± 0.7
Convex area	1.7 ± 0.8

used to distinguish sea ice from clouds, remanent errors from the image processing routine can appear as distorted shapes (e.g., regions 3 and 4). Additional sources of error are cloud residues due to thick clouds that cannot be completely filtered, as the cloud intensity values are brightened and identified as ice floes (e.g., region 5 in Figure 2.7.b). In most cases, these artifacts are products of the histogram equalization operation, which is applied to flatten and evenly distribute intensities in the image. However, given the large concentration of pixels in brighter sections of the original histogram, spikes are unavoidably introduced (Figure 2.5). Notwithstanding these processing issues, the algorithm still retrieves reliable ice floe trajectories and drift by leveraging the tracking module. The geometrical parameters of the artifacts that could result in incorrect ice floe identification have high variability throughout the image sequence; hence these are not matched within consecutive images, and the final products of the algorithm are not affected by issues stemming from the image processing routine.

Quantitatively, error in sea ice drift (σ_u), which results from the error of retrieving the correct geographical position of an ice floe and the error associated with correctly tracking it over time, is computed as [34, 51]:

$$\sigma_u = \frac{(2\sigma_g^2 + \sigma_f^2)^{1/2}}{\Delta t} \quad , \tag{2.6}$$

where σ_g and σ_f are the standard deviations of the absolute geographic position error and the tracking error respectively, and Δt is the corresponding time interval.

Retrieving the correct geographical position of ice floe centroids depends on three factors: (1) the geolocation accuracy of MODIS images (σ_i = 150 m) [146], (2) image resolution (σ_{ii} = 250 m), and (3) the accuracy of automatically identified centroid positions. Estimation

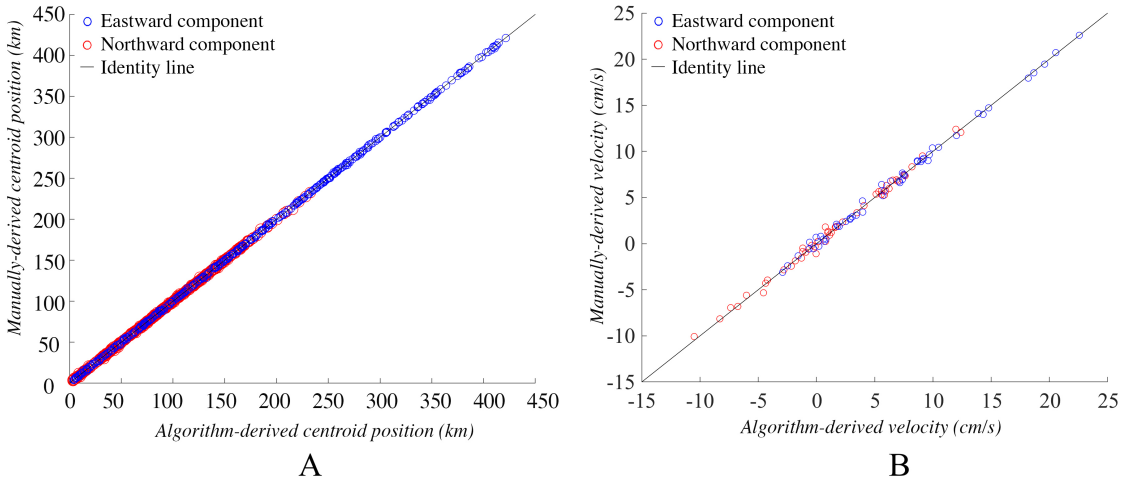

Figure 2.8: Evaluation of automatic ice floe detection. Comparison between ice floe centroid positions and velocity vectors derived by the ice floe tracker algorithm and from manually identified ice floes. Eastward and northward components along the stereographic projection axes are depicted in blue and red circles respectively for both position and velocity vectors.

of centroid positions with the ice tracker algorithm showed good agreement with manually identified ice floes, which are taken as ground truth ($R^2 = 0.99$, Figure 2.8.a). The root mean square error (RMSE) is used to estimate the error associated with automatic centroid identification,

$$\sigma_{iii} = \sqrt{\frac{\sum_{i=1}^{N_g}(x_i^m - x_i^a)^2 + (y_i^a - y_i^m)^2}{N_g}} = 255\,\text{m}, \tag{2.7}$$

where $N_g = 430$ is the total number of algorithm-manual ice floe pairs, x_i^a, and y_i^a are the coordinates of the ith automatically identified ice floe along the projection grid, respectively. Finally, x_i^m, and y_i^m are the coordinates of the ith manually identified ice floe, respectively. The geographical position error is then attributed to the greatest source of error (σ_{iii}), thus σ_g= 255 m.

Ice floe drift velocities were computed from manually identified ice floes. To this end, daily displacements were produced by employing the tracking module on the manually outlined ice floes. These trajectories were manually verified and compared to the results of the trajectories automatically produced with the algorithm, showing good agreement (R^2=0.99 in Figure 2.8.b). The error associated with the tracking module is derived from the RMSE,

$$\sigma_{iv} = \sqrt{\frac{\sum_{i=1}^{N_f}(u_i^m - u_i^a)^2 + (v_i^a - v_i^m)^2}{N_f}} = 0.5\ \text{cm/s}, \tag{2.8}$$

where $N_f = 50$ is the total number of algorithm-manual ice floe velocity vector pairs. u_i^a, and v_i^a are the eastward and northward components of the ith automatically identified ice floe velocity vectors along the polar stereographic axes, respectively, and u_i^m, and v_i^m

are the eastward and northward components of the ith manually identified ice floe velocity vectors, respectively. Based on σ_{iv}, the tracking error was computed (considering Δt = 1 day) yielding σ_f = 430 m. Hence, employing Equation 2.6, the error in the automatically retrieved sea ice velocity, σ_u, ranges from 46.77 cm/s to 0.65 cm/s (corresponding to images acquired with a Δt of 20 min and 24 hr, respectively).

2.5 Ice floe trajectories and velocities

2.5.1 Ice floe trajectories

A total of 1,061 ice floes were automatically tracked during the study period (Figure 2.9). In this image, the color gradient is indicative of the length of each trajectory, e.g., lines colored with dark blue represent trajectories comprised of two trajectory points (equivalent to identifying the same ice floe on two consecutive images). Similarly, yellow lines represent the longest ice floe trajectories (with eleven, or more, trajectory points). The length scale distribution of tracked ice floes for the duration of the study shows that the majority of the ice floes for which trajectories could be retrieved have length scales smaller than 15 km, and surface areas smaller than approximately 100 km^2 (Figure 2.10).

On average, ice floes identified for more than 24 hr were tracked for up to 2.5 days, corresponding to an average of 7 trajectory points. A total of 2,489 drift vectors composed the 1,061 trajectories retrieved. From these, 73% of the drift vectors had a southward

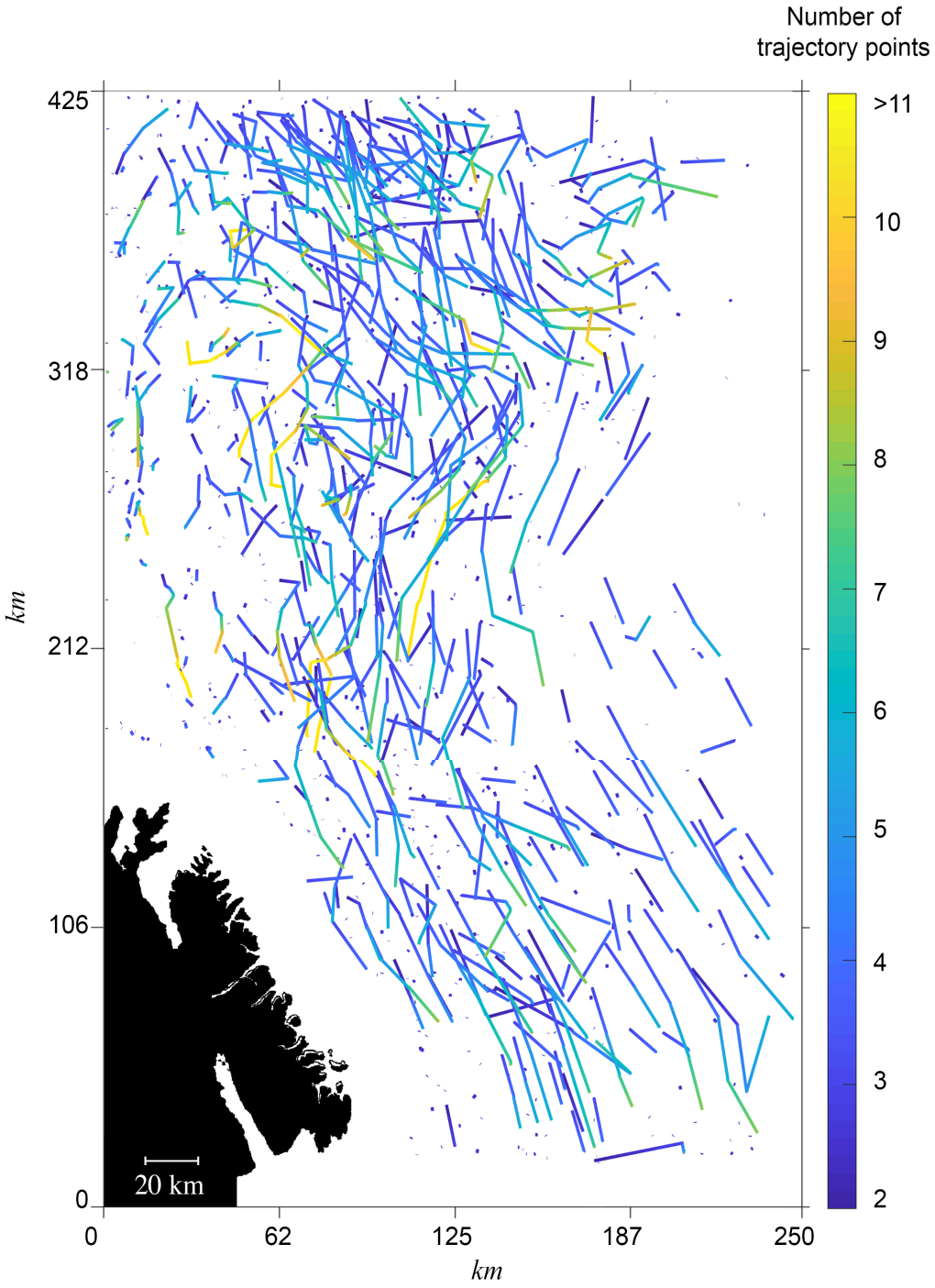

Figure 2.9: Ice floe trajectories. Retrieved ice floe trajectories during the period 20.04.2017 - 05.06.2017 are presented with solid lines. Both the length of the lines and the color gradient scale with the number of retrieved trajectory points.

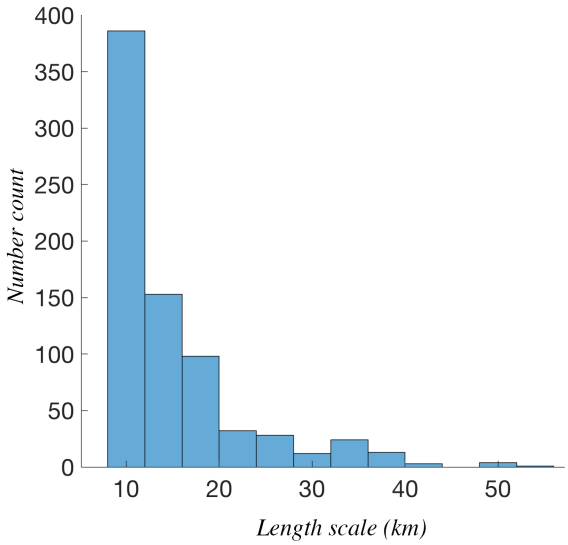

Figure 2.10: Length scale distribution of tracked ice floes. The characteristic length scale is defined as the major axis of a circumscribing ellipsoid.

direction. In these cases, displacement was dominated by an eastward motion (along the projection axes) with 66% of ice floes drifting to the south-east and 34% to the south-west. Out of all the northward trajectories, 72% corresponded to ice floes with length scales less than 15 km (and a surface area of roughly 100 km^2). Irrespective of size, 43% of the tracked ice floes experienced northward drift, at least partially (Figure 2.9).

2.5.2 Ice floe velocities

Eastward and northward sea ice velocities along the stereographic projection axes were computed from the retrieved ice floe trajectories. Specifically, velocity vectors were acquired from the drift vectors composing each trajectory, and the corresponding acquisition time difference between trajectory points for the entire study period (Figure 2.11). A mean

velocity field spanning the study period was computed by computing the weighted average of sea ice velocity vectors within a uniform grid. The spatial resolution of the grid was chosen such that approximately ten velocity vectors were enclosed in each cell, which was roughly 20 km by side. A post-processing routine commonly employed in experimental velocimetry studies was implemented to eliminate outliers [104]. This involved evaluation of the velocity field via thresholds of the maximum local velocity (twice the standard deviation from the mean of the sample data to detect velocity outliers), a standard deviation test (mean velocity minus five standard deviations of the gathered data), and a normalized median test. The resulting average sea ice velocity field is presented in Figure 2.12, where yellow arrows indicate the velocity vectors that were replaced during post-processing and the black arrows represent the final velocity field product. The majority of the flagged vectors that were interpolated according to the post-processing routine are observed to fall in the vicinity of the sea ice edge. In future versions of this algorithm, these errors can be mitigated by implementing a filter to discard sea ice floes drifting along the ice edge. With a higher resolution sea ice concentration map, the sea ice edge can be better identified and bands of brash ice or pancake ice floes, changing too fast to allow a reasonable tracking of these segments, can be removed from the analysis to improve the output. On average, northward sea ice velocities ranged from -9.3 ± 0.65 cm/s to 1.4 ± 0.65 cm/s (with negative values denoting a southward drift); while eastward velocities varied between -1.7 ± 0.65 cm/s to

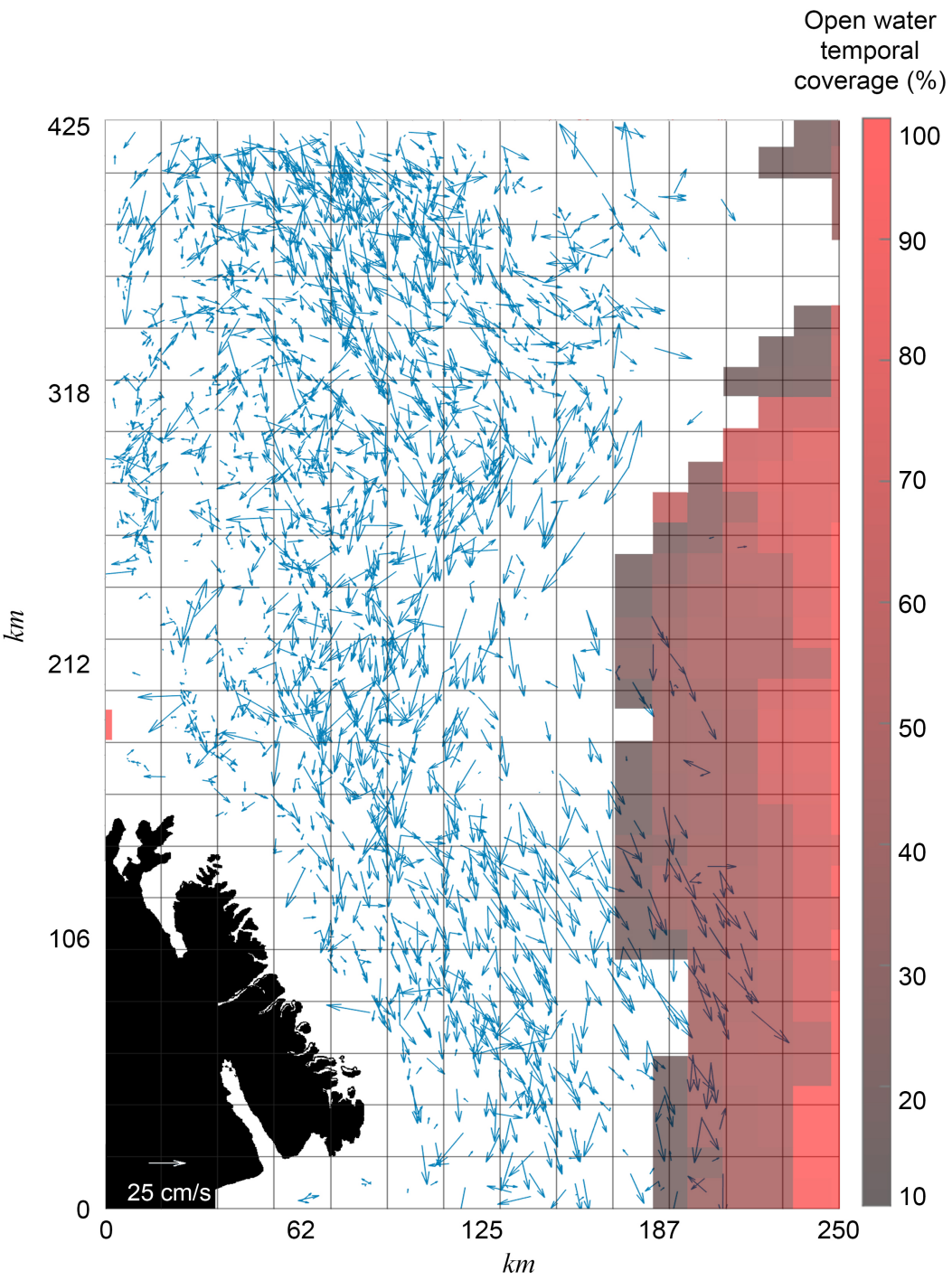

Figure 2.11: Drift velocity vectors. All drift velocity vectors retrieved during 20.04.2017 - 05.06.2017 are displayed on a 20 km grid. The AMSR-E/AMSR2 Unified L3 Daily 12.5 km Sea Ice Concentration Version 1 layer provided by the MODIS Worldview platform was employed to map the open water for the entire study period. Note that overlapping vectors are a result of superimposing the data in a single image. Red hues indicate the amount of time open water was observed in the area during the study period.

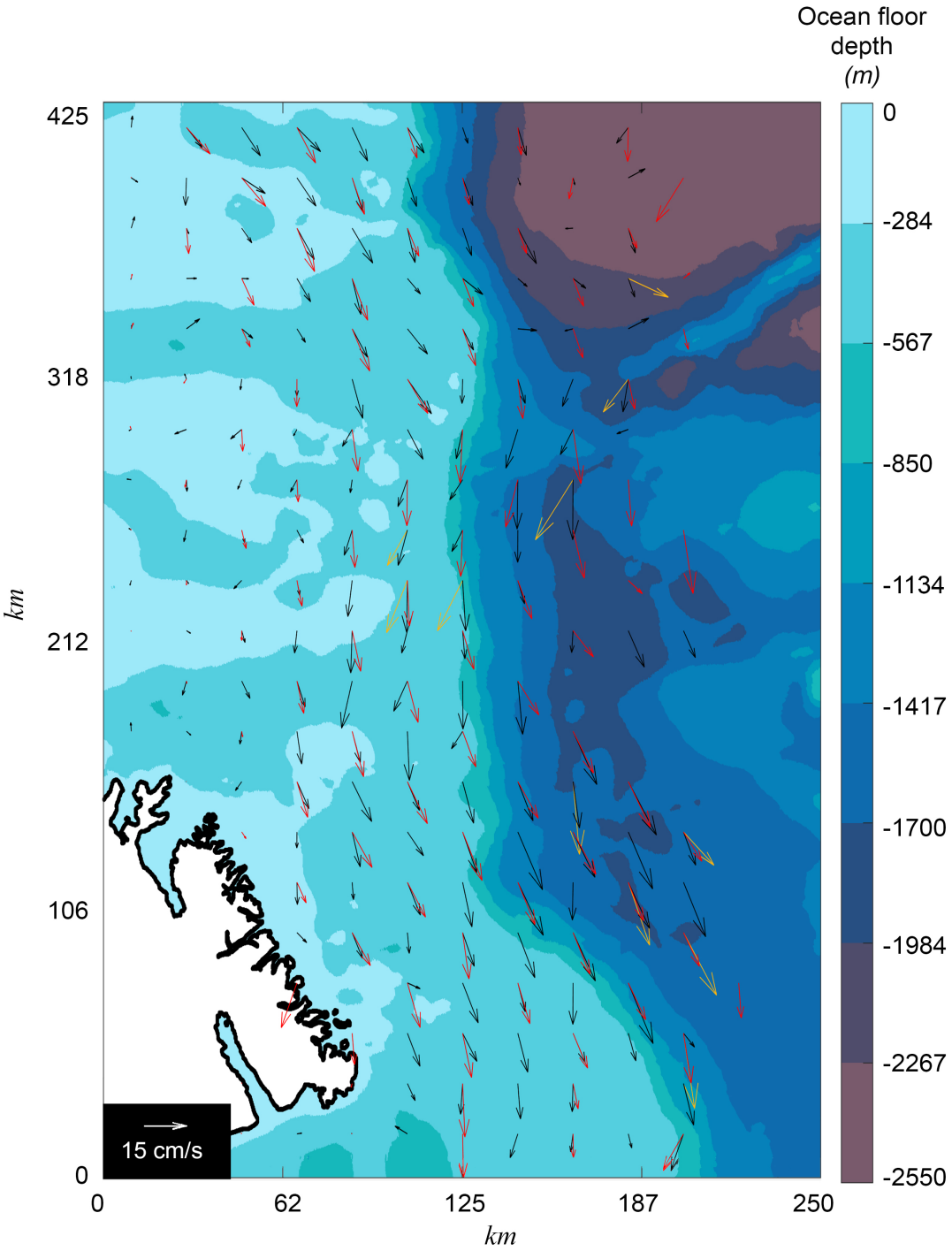

Figure 2.12: Mean sea ice velocity field. The derived velocity field before post-processing (in yellow), overlapped with the post-processed output (in black) and the CMEMS SAR sea ice velocity product of the region (in red) are presented in this figure. Ocean bathymetry is reproduced in color from ETOPO1, National Geophysical Data Center (NGDC) NOAA.

4.1 ± 0.65 cm/s (with negative values denoting a westward drift). The mean sea ice speed was 9.4 ± 0.65 cm/s.

Information on sea ice motion was also acquired from the CMEMS global high-resolution SAR sea ice drift product 011-006 (10 km of resolution). A CMEMS mean velocity field for the study period was obtained by linearly interpolating daily velocity fields onto the 20 km grid used to analyze the MODIS output. To that end, the Delaunay triangulation of points technique was employed to interpolate the scattered CMEMS data onto the 20 km grid. The Delaunay triangulation is performed by summing the three vertices of a triangle enclosing the query point. This produces the velocity field seen in Figure 2.12. Note that a few grid points in this map are empty since not all the areas in the study region had ice transition through them during the study period (see Figure 2.11). Weighted averages produced northward velocities ranging from -11.6 ± 0.6 to 0.8 ± 0.6 cm/s, while eastward velocities varied between -0.5 ± 0.6 to 3.4 ± 0.6 cm/s. The mean sea ice speed was 12.4 ± 0.6 cm/s. Comparison of the ice tracker output to the CMEMS sea ice drift product qualitatively shows good agreement. Although the CMEMS sea ice drift product employs high-resolution SAR data, moderate resolution MODIS data produced comparable results to SAR. Quantitative comparison between both products resulted in an RMSE of 5.2 cm/s ($R^2 = 0.79$, with a total vector pairs of N=86, Figure 2.13).

The discrepancy in the results compared to the CMEMS product are due to several factors. This includes differences in the operation of MODIS and SAR instruments, the most important one being that SAR imagery is not affected by clouds. In addition, the CMEMS

product employs Sentinel-1 data resampled to a 300 m resolution before sea ice displacement is computed, which is slightly different from the MODIS 250 m resolution employed in this study. Moreover, the consecutive SAR images used to calculate sea ice displacement are typically 12 to 36 hr apart [133], in comparison to the images employed in this study, which range from 20 min to 48 hr apart. While the weather independence of SAR images is indeed an advantage to extract sea ice motion, the temporal coverage of MODIS is more comprehensive. These factors contribute to the differences observed in Figure 2.13.

An additional source of error is introduced by the *1-day skip* module. Although this module significantly increased the trajectory vectors retrieved in this study, the module introduces uncertainties to the final product. When the trajectory of an ice floe is extended, the module assumes a linear drift, which is not correct. Nevertheless, this module was

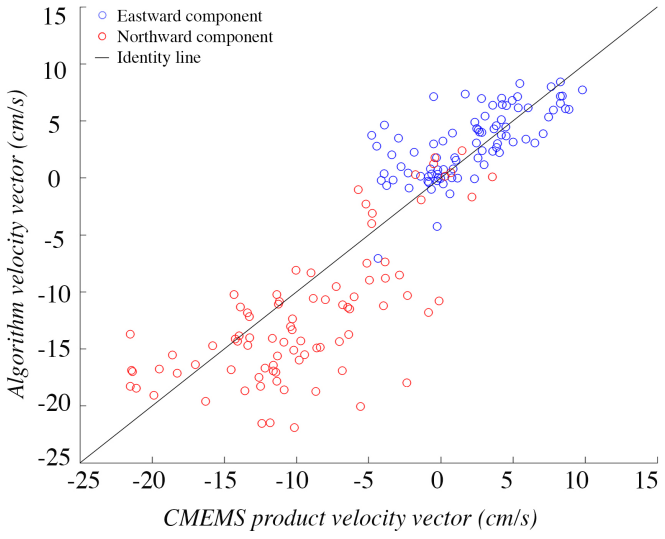

Figure 2.13: Comparison of MODIS and SAR velocity vectors. Comparison between mean velocity ice motion vectors derived with the presented algorithm and the CMEMS ice drift product for eastward and northward components along the stereographic projection axes.

necessary due to the persistent cloud cover observed in MODIS imagery. Without this module, the vector fields are too scarce to produce a mean velocity field. Moreover, the number of trajectory vectors increases with the *1-day skip* module, resulting in an improved RMSE. Without a *1-day skip* module, RMSE= 7.2 cm/s, as compared to the RMSE of 5.2 cm/s when employing the *1-day skip* module.

Other products, such as the OSI-SAF medium resolution sea ice drift product, were also explored to evaluate the output of the presented algorithm. Although this product retrieves valuable data for the Arctic Basin, no data was available for the study region during the study period.

Finally, reported sea ice drift velocities in the literature are presented here as a reference for the estimates presented in this study. Buoy measurements done by 145 during the spring of 1997 eastward from the study region (in the area delineated between 70° and 74° N and 0° and 10° W) resulted in a sea ice mean velocity of 29 ± 18 cm/s for a period of 41 days. A recent GPS study by 149 performed in between 2012 and 2014 northward from the study region (between 74° and 78° N and 6° and 20° W), reported mean ice floe velocities ranging from 6.1 ± 7.9 cm/s to 34.3 ± 20.9 cm/s in a 41-day and 52-day period, respectively. Further north in Fram Strait, at the same longitudes of the study region, monthly mean ice floe velocities have been measured to range from -15 to 5 cm/s (meridional) and -10 to 10 cm/s (zonal) during the spring of 2015 [88]. The results in this study fall within one standard deviation of the reported values in literature. Note that direct comparison is not straightforward as sea ice drift depends on the study period and location.

2.6 Conclusions

In this paper, a new processing algorithm is presented. This algorithm is developed to leverage existing long-term MODIS datasets to analyze ocean surface conditions in the Arctic. The method is adaptive, thereby differentiating sea ice-water interfaces based on pixel intensity. The intensity of the images is manipulated via time- and cost-efficient techniques to identify ice floe positions and track them continuously. No manual interaction is needed to process images, thus allowing the analysis of inaccessible and remote areas of Arctic regions with dynamic sea ice motion and relatively low sea ice concentrations via Lagrangian methods.

Various factors play a role in the quality of the products here presented. First, the centroid positions of the ice floes must be precisely located. As a quality check, the algorithm was evaluated against manual identification. Second, a good agreement in most geometrical parameters is critical for the quality of the results. A shortcoming of this method is to fully filter atmospheric conditions, which results in geometrical parameter errors (Table 2.3). Also, differentiation between landfast ice and floating ice is not possible with the present method. However, given that drift vectors within landfast ice are effectively zero, the final products are not affected by these identification errors. Third, a sufficiently high temporal sampling along the entire trajectory is needed to sample the mean velocity field correctly. While *1-day skip* module is useful, it unavoidably introduces uncertainties to the final product by extending ice floe trajectories assuming a linear drift, which is not necessarily correct.

Nonetheless, the calculated mean ice floe velocities are in good agreement with previously derived estimates in the region and SAR-derived sea ice drift products. Other sea ice drift products were explored to validate the algorithm, such as OSI-SAF medium-resolution sea ice drift product, alas the product was not able to resolve ice floe motion in the region of interest. This emphasizes one of the motivations behind this work; studies in regions where existing sea ice products cannot resolve ice motion, particularly near the coast, can benefit from using the presented algorithm.

More importantly, the observed variability of sea ice drift strongly suggests that our ice floe tracker can be employed to analyze mesoscale eddy fields. In a region highly influenced by the East Greenland Current, the retrieved northward trajectories are a clear indication of variability from a southward mean flow. These spatial deviations from the mean, especially at small length scales, highlight the feasibility of retrieving kinematic parameters of sea surface turbulence in the Arctic from MODIS imagery. Future implementations of this method could benefit from including an additional module based on cross-correlation techniques, such as those commonly used to process particle image velocimetry measurements in experimental studies of fluid mechanics, to resolve turbulent eddies with smaller length scales.

Given the accessibility of this method, this work will help to further the exploration of turbulence dynamics in the Arctic. In this region, eddy radii range from 20 to 40 km [38]. Hence, mesoscale ocean turbulence statistics could be, in principle, retrieved with this product. Furthermore, evidence of eddying motion was observed in the computed trajectory and mean velocity maps. In the central region of the study area, for example, sea ice drift

follows the topographic shelf partitioning of the ocean floor (Figure 2.12). Closer to the coast, however, whether wind- or oceanic-driven, areas of recirculation are observed both in shallow waters (<280 m) (top left corner of Figure 2.13) as well as in deep waters (<2000 m).

With the continuation of the MODIS program, this ice floe tracker provides new means to study sea ice drift in the Arctic. New analysis methods are introduced in the next chapters of this thesis.

Chapter 3

Sea ice dynamics mirror the underlying turbulent oceanic currents amid strong atmospheric forcing

3.1 Introduction

An accurate understanding of the sea ice field is crucial for navigation operations and the conservation of the Arctic. Of particular interest are marginal ice zones (MIZ), where the coupling between sea ice and the open ocean intensifies. In these regions, the oceanic flow field plays a crucial role in the formation, melt, and distribution of sea ice. In MIZ, sea ice spanning a wide range of length scales move primarily due to wind and ocean forcing. Evidence of meso/submeso-scale turbulent eddies interacting with sea ice has been

thoroughly documented, from *in-situ* measurements to satellite remote sensing imagery. Nevertheless, a complete parameterization of these interactions remains difficult to achieve. In this chapter, sea ice field information derived from MODIS imagery is used to investigate the role of oceanic eddies on sea ice transport.

Several studies have investigated the role of atmospheric and oceanic forcing on sea ice drift. Lukovich et al., [68], for example, characterized ice drift features associated with individual ice beacons during the winter of 2008 to investigate the key mechanisms causing variability in the sea ice drift field. The team assessed atmospheric and oceanic conditions during three case studies in which the effects of coherent structures were observed, i.e., reversal events forcing buoys into loops or meanders. The team demonstrated that the sea ice-ocean-atmosphere coupling was enhanced, but only for a single case, with others showing a weak coupling. Furthermore, although the study attempted to characterize atmospheric conditions during turbulent events, the number of study cases was too small to adequately characterize these interactions. In a subsequent study, Lukovich et al., [69] employed GPS beacons deployed in the southern Beaufort Sea in the fall of 2009. The team identified inflection points in the drift of sea ice, as well as directional changes of the beacons during eight loop- and meander-reversal events in the beacons' trajectories. The direct comparison of ice drift and surface winds showed that these events were highly correlated to surface wind changes. This work established a framework to characterize directional changes in sea ice drift in response to atmospheric forcing based on Lagrangian dispersion statistics. Gabrielski et al., [26] also analyzed the wind field along the trajectories of a single buoy.

Their findings suggested a strong coupling between sea ice drift and atmospheric forcing. However, a single case study is not sufficient to fully characterize these interactions.

In this chapter, the role of atmospheric and oceanic forcing on ice floe motion is assessed employing a robust statistical analysis. To that end, a correlation analysis between wind and ice velocity fluctuations is performed to determine the influence of atmospheric forcing during turbulent events in sea ice drift. An innovative approach employing ice floe rotation measurements is here presented. This metric has never been reported on a large sea ice database due to the inherent difficulty of measuring this parameter from *in-situ* or remote sensing observations. This in-depth assessment of the wind field led to the development of an automatic eddy detection tool from MODIS imagery.

This chapter is structured as follows. In the next section, the methodology used to characterize the dynamics of sea ice is presented. Section 3.3 presents the analysis of the results regarding sea ice-atmospheric interactions and the eddy detection tool. Conclusions follow in Section 3.4.

3.2 Technical approach to characterize sea ice drift

3.2.1 Angular ice floe velocities

The unique dataset developed in Chapter 2 contains information on ice floe shape characteristics derived from MODIS imagery. The dataset includes the perimeter, major and minor axes of the ellipsoid matching the second central moment, centroid position, and surface and

convex areas. The convex area is defined as that of the smallest convex polygon enclosing an ice floe. These surface metrics allow the quantification of the rotation angle evolution of an ice floe. The angle evolution of sea ice has been rarely reported in the literature due to the inability to calculate it from *in-situ* field measurements [149].

The calculataion of the rotation of sea ice is based on examining the shape of floes at consecutive trajectory points. To illustrate this process, an example is presented in Figure 3.1, where the Lagrangian trajectory of an ice floe is displayed for a period of two weeks. The daily positions of the ice floe are plotted. In addition, the mean velocity field spanning the study period is presented (see Chapter 2). In this example, as the ice floe drifts southward, significant continous rotation about its center of mass is observed. To quantify the evolution of the rotation angle, the shape of the ice floe at the beginning of the measurement period is superimposed (panel a) onto its shape at a subsequent location (panel b). The angle of rotation, which produces the minimum misaligned regions during this superposition process, is then selected. These misaligned regions are highlighted in panel c with different colors for reference. In this particular case, the ice floe rotated 61° clockwise in 7 days. The analysis described here is performed at each point of each ice floe trajectory until the evolution of the angle of the entire dataset computed is computed. Finally, the angular velocity of the ice floes, Ω, is quantified employing the acquisition timestamp of the images.

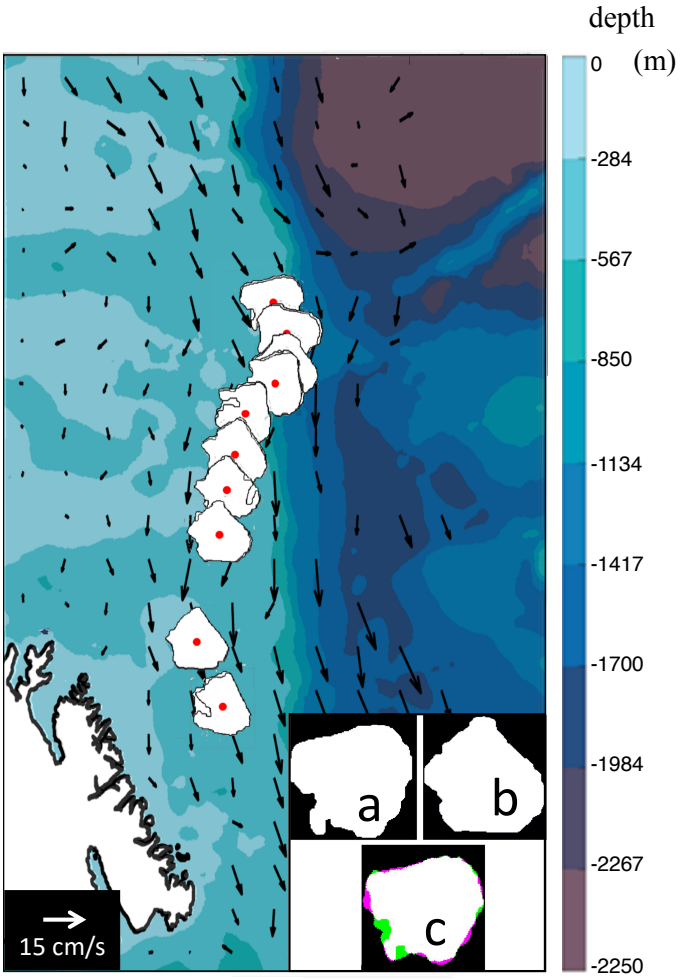

Figure 3.1: Ice floe rotations. Example of a two-week Lagrangian trajectory with daily contours plotted on map from both Aqua and Terra satellites. a) Contour of the ice floe at the beginning of the image sequence. b) Contour of the same ice floe after nine days. c) Superposition of both contours used to quantify ice floe rotation. Matching areas are shown in white. Pink and green areas denote misaligned regions.

3.2.2 Curvatures of ice floe trajectories

An analysis of the nature of the trajectories is also performed. The retrieved sea ice trajectories are classified into two groups: those displaying a straight path for over 5 days, and those with curved trajectories. Since the analysis is sensitive to noise, sea ice trajectories

are first smoothed using a Bezier curve interpolation scheme [66]. Next, the curvature of a trajectory is calculated employing the tools developed by [84]. The consecutive points along the trajectory are analyzed in sets of three labelled A B and C, which form the line segment $\overline{ABC}$. A circle circumscribing $\overline{ABC}$ is estimated, as well as a radius r_i to the center of this circumscribed circle. The local curvature vector is thus defined as $k_i = \epsilon_i / r_i$, where ϵ_i is the unit vector in the direction from B to the center of the circle.

The magnitude of k_i is substantially smaller for straight curvatures compared to curved ones. In other words, for local straight paths, the center of a curve lies far from the three points $\overline{ABC}$. In contrast, a path with an inflection has a center much closer to these points. By statistical analysis cutoff values of $k_i < 0.002$ and $k_i \geq 0.002$ were determined to discriminate between straight and curved trajectories, respectively. It is important to note that these bounds are applied on images with a spatial resolution of 250 m and, hence, k_i values are obtained using pixels units. In conclusion, a segment is considered to have an *inflection* if $k_i \geq .002$ for at least 5 days. Otherwise, it is considered *straight*.

3.2.3 Wind velocity field

The ERA5 10 m wind speed reanalysis data was employed to assess the role of atmospheric forcing on ice floe dispersion. The product is obtained from the European Centre for Medium-Range Weather[1]. Hourly wind data is averaged considering a 7-hour window (3 hours before and 3 hours after sea ice velocity measurements are acquired). Using a

[1]Copernicus: https://cds.climate.copernicus.eu

biharmonic spline interpolation scheme, the wind velocity vectors are interpolated to match the exact position of the ice floes positions.

3.2.4 Automatic eddy detection tool

An automatic eddy detection algorithm was developed. Sea ice Lagrangian trajectories and their rotation evolution were used to characterize the flow field and identify meso/submeso-scale ocean eddies.

A geometric definition of a loop is implemented to identify sea ice trapped inside of an eddy [7]. In this scheme, an ice floe that followed a trajectory descrubed by a closed curved is considered to have formed a loop if the motion occurred between 5 to 21 days, according to the time and length scales observed in the area [38]. The ice floe closes its loop when its initial and final position overlap. Realistically, the distance between the initial and final positions, D, is not zero. Thus, D must be smaller than a threshold maximum distance D_0, which depends on the scale of the eddy in question [18]. From a manual identification and analysis of trajectory loops, the tolerance was set such that small floes (< 180 km^2) forming loops between 5 to 7 days with a surface area, A_L, smaller than 300 km^2 are assigned a value of $D_0 = 10$ km. The threshold distance for bigger ice floes (> 180 km^2) is set to $D_0 = 20$ km.

In general, even if an ice floe trajectory forms a closed loop by meeting the distance threshold, the ice floe may in fact be locally trapped [18]. The distance between the initial and the final positions, D must form a loop with a perimeter smaller than half the displacement distance of the ice floe during the query days to ensure that the ice floe is indeed circulating.

In addition, there is no certainty that a large ice floe is being turned by an underlying eddy or some other forcing source if the surface area of the ice floe, A_i covers the area formed by the loop, A_L. Therefore, from statistical inspection, $A_L \geq 32A_i$ to ensure the trajectory points of an ice floe actually form a loop. Due to the image resolution, only loops with an area greater than 2 km^2 are considered.

Finally, not all the loops formed by sea ice were eddies. As atmospheric forcing drives sea ice to drift over an oceanic eddy field, the eddy field forces sea ice to rotate over its own axis while it moves through the eddy. To identify oceanic eddies correctly, the angular velocity of sea ice, Ω, had to coincide with the motion of the eddy field. To that end, eddy vorticity, ζ, is defined as 2π divided by the time taken by the ice floe to complete the loop. As such, this tool allows for the quantification of an eddy's rotational direction, lower-limit apparent radius, and location.

To summarize, the following conditions must be met to identify an eddy from sea ice:

1. The ice floe must form a loop within 5 to 21 days and have a radius of over 2 km^2.
2. The ice floe must return to an initial point considering a tolerance of D_0.
3. The distance traveled by the ice floe must be long enough to avoid trapping.
4. The area of the loop formed by the eddy must be greater than 32 times the area of the ice floe forming the loop.
5. The ice floe must rotate over its own axis in the same direction as its translation displacement direction.

3.3 Results

The developed approach to track the translational and rotational evolution of sea ice provides a resource to automatically characterize the oceanic turbulent eddy field from MODIS imagery. The Beaufort Gyre (BG) is a major basin-scale anticyclonic current in the Western Arctic Ocean. For a few decades, the gyre has accumulated a large amount of fresh water [102]. To maintain equilibrium, the number of small eddies in this region has increased [154]. To investigate the inter-annual variability of the BG, the characteristics of the underlying flow field in MIZ were evaluated within the past two decades. The position, velocity, and rotation rates of over 28,000 ice floes in the BG MIZ were calculated. Sea ice transitioning over an eddy was demonstrated to rotate over its vertical axis according to the underlying eddy flow field.

The characteristic rotation rate of the observed floes, Ω, depended strongly on their size. Normalized by the Coriolis parameter $f = 10^{-4}$, their rotation rates can reach values of up to 0.15 for the relatively small 5 km floes. In comparison, floes larger than 50 km rotate an order of magnitude slower than the smallest detectable floes. An example of this behavior is presented in Figure 3.2 (panels a-e). The rotation evolution of two ice floes is plotted. As the floes drift, it is evident that they also significantly rotate about their center of mass. A sketch of the recovered five-day trajectories is displayed in the last panel. The smaller ice floe shows a faster rotation rate than the bigger ice floe. The color of each ice floe is

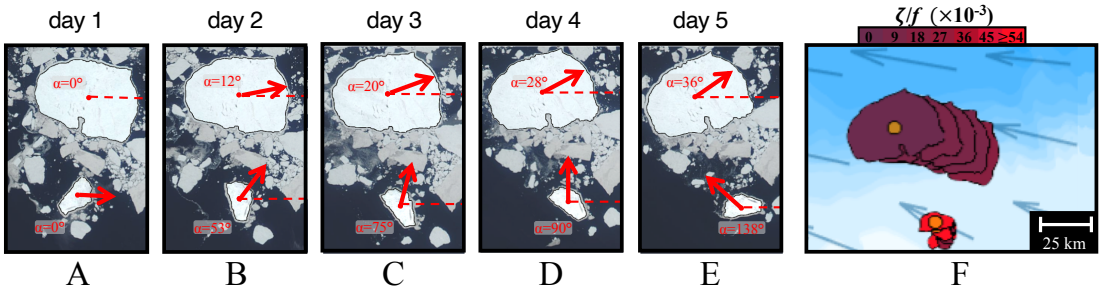

Figure 3.2: Ice floe rotation rates. a-e) Time series of the rotation rate of two representative sea ice floes over five consecutive days. f) Sketch of collapsed trajectories for both ice floe cases. The color of each ice floe is representative of its vorticity normalized by the Coriolis parameter, f at a given time step. The mean geostrophic ocean current velocity (2003–2014) is plotted in background [4]. Ocean bathymetry is reproduced in color from ETOPO1, National Geophysical Data Center (NGDC) NOAA [91].

representative of their vorticity normalized by the Coriolis parameter taken at each time step of their trajectories.

The statistics of floe rotation predominantly reflect the properties of the oceanic eddy field. A strong correlation between the rotation rates of sea ice and the vorticity of underlying ocean eddies was established via an idealized high-resolution numerical model [2]. The model simulates translational and spinning motion of floes via a two-layer quasi-geostrophic (QG) framework [3]. The model is initialized by ERA-5 atmospheric wind data. The model also employs the MODIS sea ice observations, which include the shape of the ice floes and linear and rotational velocities (see Figure 3.3.A). The main model parameters include the Rossby deformation radius, R_d, the vertical shear of the horizontal currents, ΔU, the ratio of layer depths, δ, and the drag coefficients of the top and bottom boundaries. These parameters are

[2]This investigation was done in collaboration with the Oceanographic Team from the University of Washington. The effort to develop the QG model was performed by Dr. Manucharyan, while the author provided the observations to initialize the QG model and participated in the analysis of the results.

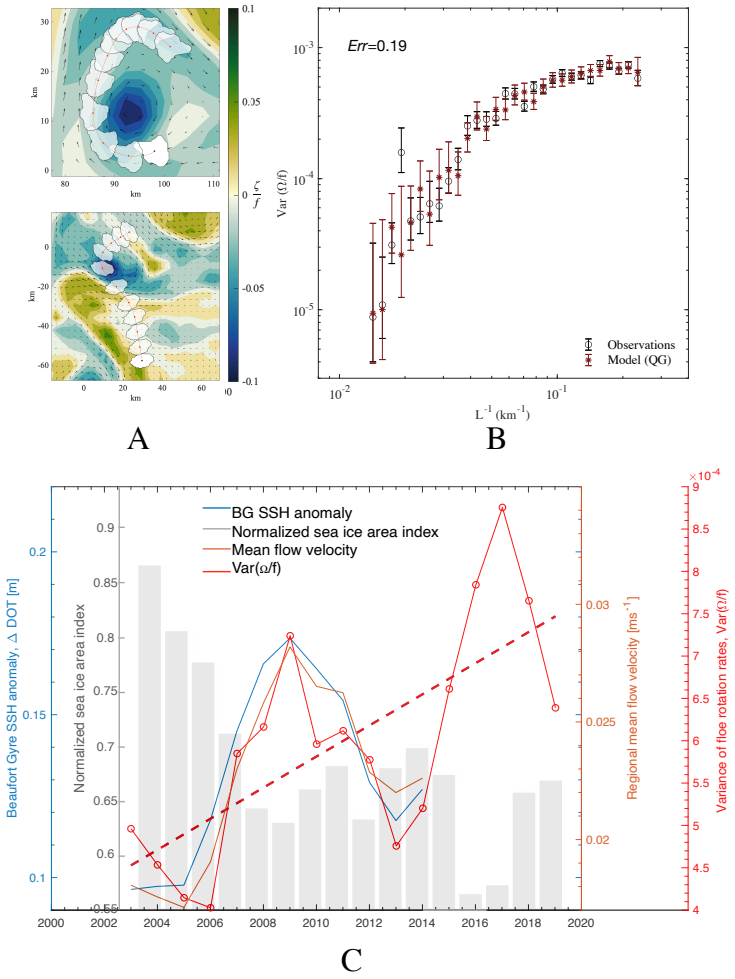

Figure 3.3: Sea ice and oceanic statistics. a) Examples of floe rotation and translation over eddies initialized with a constant wind flow field and sea ice shapes and velocities (from MODIS imagery). The underlying oceanic flow field was generated by a QG model with best-fit parameters from MODIS observations. Color scheme represents the average ocean vorticity normalized by f. b) Variance of the simulated (red) and observed (black circles) floe rotation rates as a function of floe length-scale; the error bars denote 95% confidence intervals. c) Interannual evolution of the floe rotation rates variance (red), bulk SSH anomaly associated with the Beaufort Gyre (blue), mean flow in the south-east Beaufort Gyre, and the seasonal mean of sea ice concentration (gray). The data points in the timeseries represent three-year running mean values.

adjusted to produce an eddy field that mimics the observed rotational statistics of the ice floes (as seen in Figure 3.3.B). The variance of the simulated sea ice floe rotations agree with the variance of the observed floe rotation rates. Within a few hours, the simulated ice floes reach statistical equilibrium with the driving forces, and the floe angular velocity is highly correlated to the ocean vorticity, ζ, averaged over the floe surface area.

The inter-annual variability of the sea ice rotation rates is investigated by comparing the observed rotation statistics against the conditions of the region over the twenty-first century. Figure 3.3.C shows the the ice floe rotation rates against the strength of the BG. To assess the strength of the BG, two metrics were quantified: the BG sea surface height (SSH) anomaly and a regional mean flow velocity. To quantify a characteristic seasonal average SSH anomaly, the difference between the SSH of an area encompassing the center of the gyre and its periphery is calculated. The center of the gyre was defined as the region enclosing most of the gyre during the spring and summer seasons from 2003 to 2019. The area surrounding the gyre excludes shallow waters that were below 100 m deep. Next, a regional mean flow velocity is calculated as $KE_o = \frac{1}{2}\rho_o\left(< u_o^2 > + < v_o^2 > \right)$. The monthly geostrophic oceanic currents are denoted by (u_o, v_o). Angle brackets denote regional averages within the time frame of availability of sea ice floe observations. Water density values are taken as ρ_w=1 kg/m^3 and ρ_o=1000 kg/m^3. Both metrics are produced from Armitage et al., [4]. From figure 3.3.C, the strong correlation between the rotational characteristics of sea ice with the oceanic conditions of the BG demonstrates that the statistics of floe rotation can be used to infer the properties of the oceanic eddy field.

It was also observed that ice concentration suppresses the eddy field due to the frictional eddy kinetic energy dissipation by the ice-ocean drag taken from the NSIDC MASIE-AMSR2 (MASAM2) 4-km product [23]. A sea ice area index is calculated by defining the area covered by sea ice relative to the total area of the Beaufort Sea (983,663 km^2). This relationship provides direct observational evidence that declining sea ice concentrations lead

to enhanced turbulent activity on the ocean surface. Ice cover dramatically suppresses the eddy field due to the frictional eddy kinetic energy dissipation by the ice-ocean drag. The consequences of this can be far-reaching as sea ice continues to retreat. Large-scale currents and the eddy field will become much more energetic, contributing to enhanced lateral and vertical flux of heat, salt, and chemical tracers.

Upon establishing a strong correlation between the rotation rates of sea ice and the vorticity of underlying ocean eddies, the influence of atmospheric and oceanic forcing on ice floe motion was further assessed. To that end, an analysis between wind and ice velocity vectors was performed to determine the influence of atmospheric forcing on sea ice drift during turbulent events. First, the sea ice trajectories collected from the Greenland Sea MIZ from 2003 to 2020 were classified into two groups: trajectories with *straight* and *curved* sections (Section 3.2.2). The wind forcing contribution on these two groups of trajectories was evaluated via statistical analysis.

The turning angle between the sea ice drift observations and the 7-hr mean ERA wind vectors were calculated. Distinguishing between trajectories with straight and curved sections, the influence of the wind was examined. The majority of the *straight* sea ice trajectory sections remained *with wind heading*, as the majority of sea ice followed the direction of the wind within 0° to 30° (Fig 3.4.A, grey). On the other hand, when the *curved* sections were examined, there was no clear relationship between the direction of the observed sea ice velocity and that of the wind (Fig 3.4.A, orange). This is an indication that the influence of wind during an inflection is not the dominant factor for sea ice drift and

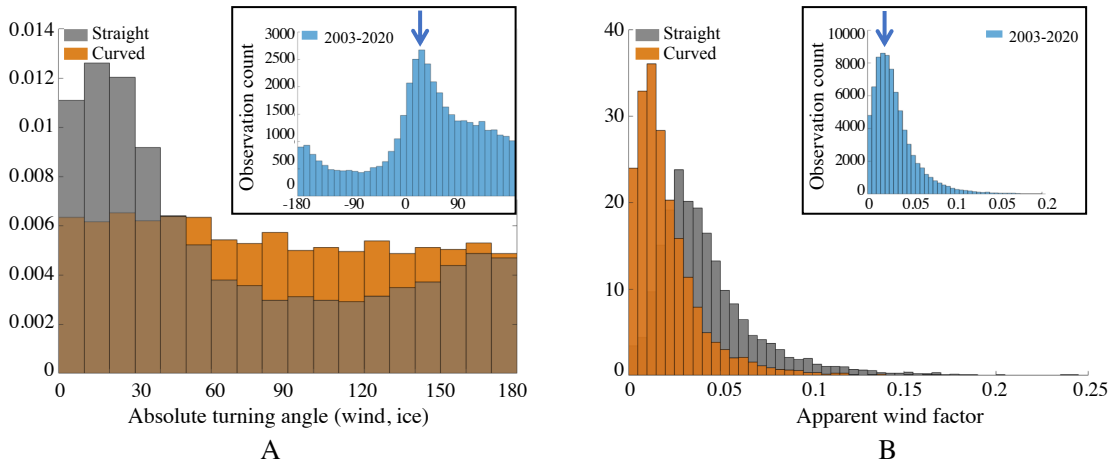

Figure 3.4: Turning angle and wind factor. a) Probability distribution of turning angles between ice and wind velocity vectors. Metrics from ice floes following straight paths are displayed in grey, while inflection paths are presented in orange. The majority of straight path observations are *with wind heading*. (Inset) Histogram of turning angles between ice and wind vectors considering all the observations collected during this study. As expected in the northern hemisphere, sea ice vectors pointed 20° to 30° to the right of wind vectors. b) Probability distribution of the apparent wind factor, ($|v_{ice}|/|v_{wind}|$). The apparent wind factor of ice with straight trajectories is much larger than those in inflection paths. (Inset) Histogram of apparent wind factor considering all the observations collected during the study. The expected 2% influence of wind on ice is observed.

could possibly point at sea ice trapped in a vorticity-dominated region, i.e. an oceanic eddy core. Next, the turning angle between the sea ice drift and the mean wind vector of all of the sea ice observations was calculated, notwithstanding of the sea ice trajectory characteristics. Overall, the ice vectors remained 20° to 30° east of the wind direction, as expected from Earth's rotational effects, (Fig 3.4.A, inset). Floes driven by wind will follow 25° to the right of the wind [90]. Floes driven by water currents will show rotation uncorrelated to the wind direction.

The apparent wind factor was also quantified. This parameter describes the ratio of sea ice speed to wind speed, $\frac{|v_{ice}|}{|v_{wind}|}$. Sea ice speed is known to be about 2% of the surface wind speed [90]. As expected, assessing all of the collected measurements regardless of trajectory

direction, sea ice drift speed corresponded to 2% of the wind speed, (Fig 3.4.B, inset). Once again, a distinction between the *straight* and *curved* trajectories was performed. The *straight* trajectory sections display a greater apparent wind factor than the *curved* sections (Fig 3.4.B). As such, wind forcing has a stronger influence on sea ice motion when the trajectories of sea ice do not curve or are unaffected by the underlying turbulent flow field.

To examine the nature of wind, the variability of 24-hr winds of *straight* and *inflection* trajectories was quantified. No clear distinction between the two groups was observed, indicating that the observed deviation from a mean southward flow of sea ice is not entirely due to intermittent atmospheric events. These results are in accordance to the low correlation found between sea ice and wind motion in the Beaufort's sea MIZ by [71], who attributed submesoscale ocean currents to the observed sea ice motion. The decorrelation found between curved wind trajectories and the wind vectors demonstrates that wind is not the only source of sea ice motion variability.

The weak correlation displayed by wind velocities and the curving sea ice paths presented the feasibility to identify Lagrangian coherent structures in the flow field from sea ice motion. When sea ice is trapped in an eddy vortex, its motion can mirror the underneath oceanic coherent structure and can consequently form a loop in its trajectory. Eddies in the region are reported to range within 20-40 km with a lifetime of 2-3 weeks [142]. Meanwhile, larger eddies have been detected in the region, reaching 80-90 km and lasting no more than 10 days [48]. Therefore, sea ice loops are restricted to spatial scales smaller than 100 km with a minimum of a 5 day lifetime. Atmospheric vortices develop at spatial scales too large

($O(2)$- $O(3)$) km and at time scales too quick (1-2 days) to induce the observed loops in sea ice trajectories [143]. Additionally, inertial oscillation frequencies in this region vary from -1.885 to -1.975 cycle/d. For these reasons, the motion here described can be attributed to oceanic forcing.

In order to recognize these turbulent events, loops in sea ice trajectories are automatically identified, i.e., inflection sections of sea ice trajectories when the sea ice returns to an original position after some time and closes its curve as described in Section 3.2.4. The acquisition of Ω on a large sea ice dataset has not been reported before in the literature. Sea ice displaying closed curvatures in their inflection trajectories over a period of 5 days or more, in addition to coinciding ω and ζ directions, were identified as motion driven by oceanic eddies. Some examples are presented in Figure 3.5.A-C. The insets show daily positions of sea ice recovered from satellite observations. The radius of sea ice trajectories transitioning over oceanic eddies is presented as a low-bound length scale of oceanic eddies in the region, ranging from 3 to 23 km. A total of fifty-one eddies were identified via sea ice observations. The locations of eddies are observed to cover the entire study region, concentrating in shallow waters, as seen in Figure 3.5.E. Leveraging the ability to retrieve rotation rates, the rotational direction of an ice floe is employed to determine the rotational direction of the underlying eddy. There was a slight anticyclonic directional preference, with 63% of the eddies rotating in that direction, but no dominant gyre drives the motion in this region.

Ice–ocean interactions were observed using the first ice- tethered profiler equipped with a velocity sensor in the Beaufort Gyre by Cole et al., [12]. The team collected ice velocity, u_{ice}, and ocean velocity at 7-m depth, u_{ocean}, among other parameters, from October 2009 to March 2010 in the Canada Basin. Over the 6 months of observations, the speed regression between the ice and ocean at 7-m depth was $u_{ocean} = 0.43u_{ice}$. Leveraging this information on the sea ice-ocean field, the collected sea ice velocities in this study were scaled using this factor (see Figure 3.5.D). Sea ice trapped in an eddy displays sea ice rotation rates equal to the underlying eddy flow field. This is in accordance with [75] and the results presented earlier demonstrating sea ice transitioning over an eddy rotated over their vertical axis in accordance with the underlying eddy field of motion. These results emphasize how the accurate parametrization of sea ice in MIZ is important, as the evolution of sea ice drift in MIZ cannot be solely attributed to wind. As such, meso/submeso-scale oceanic currents must be taken into consideration for accurate modeling and forecasting of sea ice conditions in the Arctic.

3.4 Conclusions

In order to improve prediction models of sea ice evolution, it is crucial to understand the ocean-ice-atmosphere coupling across a wide range of scales. The results from an extensive investigation of the sea ice and atmospheric fields reveal the critical physical processes driving sea ice motion in MIZ regions. The Lagrangian sea ice observations, along with a

suite of concurrent upper ocean and atmospheric measurements, provide crucial information to achieve accurate parameterization of sea ice-turbulent ocean interactions in MIZ.

In this chapter, a correlation between the rotation rates of sea ice and the vorticity of underlying ocean eddies via an idealized QG model was established. The model simulates the translational and spinning motion of floes. The model was initialized with ERA-5 atmospheric wind data as well as observational data of sea ice derived from MODIS imagery. Sea ice rotation was demonstrated to predominantly reflect the vorticity of underlying eddies.

The role of atmospheric and oceanic forcing on sea ice motion was further investigated. Leveraging atmospheric forcing information, sea ice variability was found to have a weak correlation to atmospheric forcing. From this framework, an automated eddy detection tool employing MODIS-derived sea ice trajectories was presented. Using the trajectory and, for the first time, rotation information of sea ice, meso/submeso-scale eddies along the Greenland Sea and Fram Strait MIZ were automatically identified. The ability to quantify sea ice vorticity provides an innovative source to analyze the underlying turbulent eddy field.

A total of fifty-one events were identified in which sea ice trajectories formed loops as if trapped in eddies. Even in the presence of strong winds, the imprint of oceanic eddies is evident in the Lagrangian trajectories of sea ice floe motion. These observations highlight the importance of sea ice-ocean interactions, such that sea ice drift in MIZ cannot be solely attributed to atmospheric forcing. Understanding the tight connection between sea ice and ocean dynamics will allow for a more comprehensive characterization of the turbulent eddy field at the meso/submeso-scale range in MIZ.

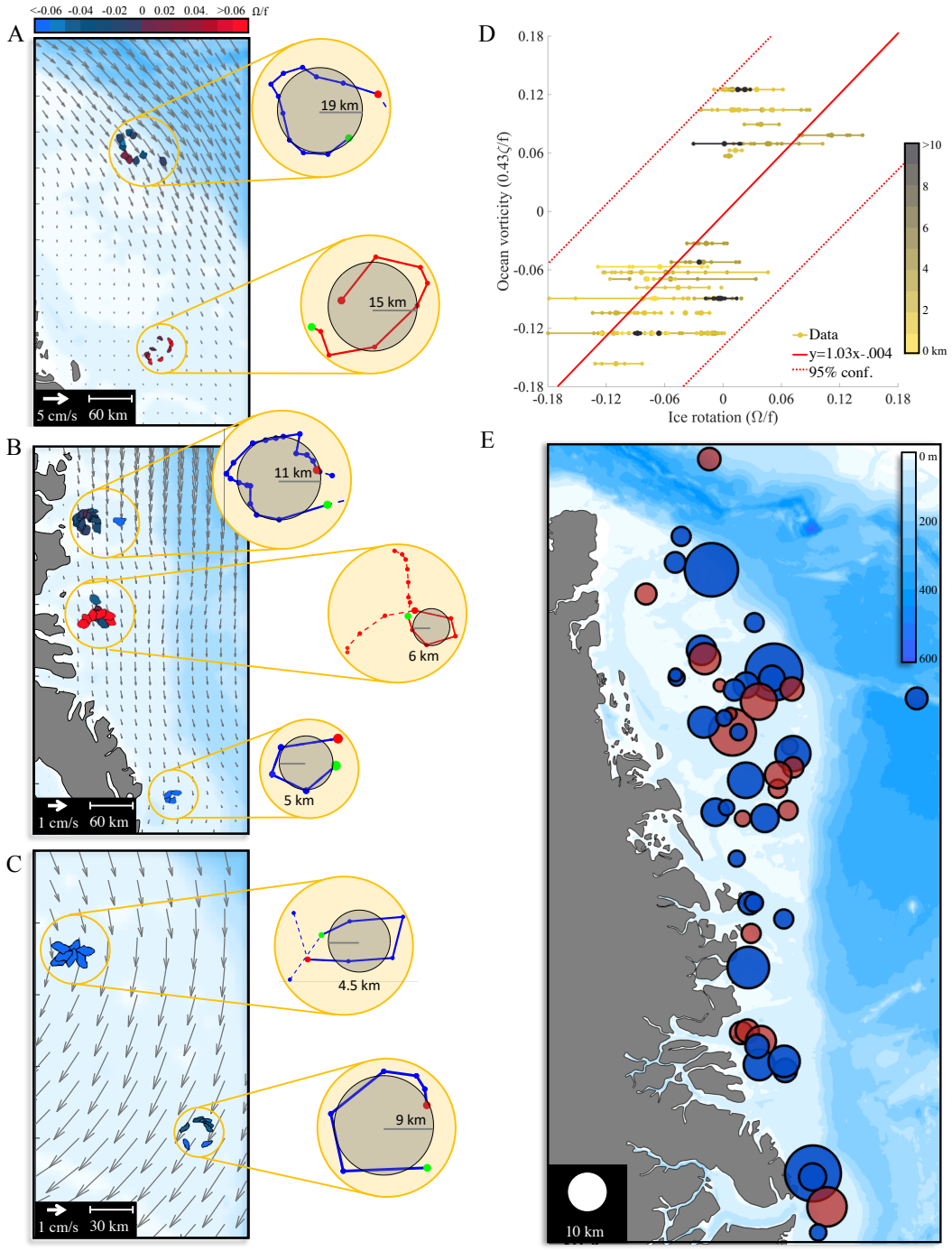

Figure 3.5: Rotation characteristics of tracked sea ice. a-c) Examples of sea ice trajectories forming loops during (a) 09.2006, (b) 06.2007, and (c) 07.2007, respectively. Daily positions and shapes of sea ice displayed with normalized rotation rates. Monthly mean velocity flow field calculated from NSIDC 25-km sea ice drift product. Insets show the loops formed by the trajectories, along with an estimated eddy core radius. d) Scatter plot of average normalized eddy vorticity versus daily normalized sea ice rotation rates of sea ice displaying eddy-like trajectories (all normalized by f). Ice rotation rates belonging to the same sea ice under the influence of the same eddy are joined by a straight line. Color scheme is representative of estimated apparent eddy radius. e) Eddy locations, apparent radii and direction of eddies identified using the MODIS detection tool during the spring- and summer-time MIZ from 2003 to 2020. Red (blue) circles denote cyclonic (anticyclonic) direction of the eddy. Marker size is proportional to eddy apparent radius. Bathymetry of the region is taken from General Bathymetric Chart of the Oceans (GEBCO).

Chapter 4

Sea ice evolution during the twenty-first century from statistical dispersion metrics

4.1 Introduction

Characterizing the critical processes driving sea ice motion in MIZ is crucial for the improvement of prediction models, ocean operations, and the conservation of the Arctic. However, monitoring the long-term changes of sea ice dynamics in these regions remains challenging. Dating back to work done by Cole and Thorndike [13, 14], sea ice motion has been employed as a tracer to extract the signature of turbulence in the ocean. Building on to the framework of these studies, the structure and evolution of the sea ice drift field within the

MIZ is investigated in this chapter. The unique dataset of sea ice observations derived from optical MODIS images developed in the Chapter 2 is employed to quantify the dispersion statistics of sea ice, namely single-particle dispersion statistics.

The focus of this chapter encompasses the north-eastern coast of Greenland (Figure 4.1.B). Year-round, the region is covered by sea ice exported from the Arctic through Fram Strait. As mentioned earlier, Fram Strait is the largest and most concentrated meridional sea ice flow in the world [139]. The region is characterized by strong winds [39], and the East Greenland Current (EGC). The EGC, as the only major southward flowing current in the Greenland Sea [148], transports over 90% of this ice [114]. Submesoscale oceanic eddies drive recirculating warm Atlantic waters into the region, impacting the heat, salinity and thus sea ice structure [140]. The first baroclinic Rossby deformation radius, R_0 in the Greenland Sea is approximately 5 km [92]. This suggests eddy wavelength variability in the order of $2\pi R_0$. In the region, eddy radii ranges from 15 to 35 km, while eddy lifetime ranges from 20 to 30 days [38, 72]. The sea ice velocity field is employed to study the topology of the underlying flow field in MIZ and infer the properties of the turbulent eddy field in the region.

The MODIS dataset employed in this study represents the longest record of Earth ever compiled [147]. As such, these images can provide invaluable daily observations at moderate spatial resolutions extending throughout the 21st century. The number of observations is extensive, in contrast to studies that employ, for example, solely IABP data. Therefore, the extension of the long-term MODIS database allows for the analysis of inter-annual variability of sea ice dispersion by focusing on the following questions:

- What are the characteristics of sea ice dispersion in MIZ?
- How have the properties of sea ice velocity field changed in the last two decades?

These questions are addressed in this chapter. In section 4.2.1, a brief theoretical review of single-particle statistics and the methodology employed to quantify single-particle dispersion of sea ice is presented. The absolute dispersion and variability of the sea ice field over the twenty-first century are presented in Section 4.3. Finally, this chapter concludes with a discussion and summary in Section 4.4.

4.2 Theory review and methodology

4.2.1 Absolute dispersion theory

Here, the theory developed by Taylor [128] on the absolute diffusion of a turbulent flow is applied. The first stipulation of this turbulence theory is the assumption of a statistically homogeneous and steady turbulent flow field without the presence of a mean flow. Therefore, the influence of the mean flow must be removed from the MODIS-derived sea ice measurements. To that end, sea ice motion is decomposed into a mean (predictable) and a fluctuating (unpredictable) component. The latter component is motion due to fluctuations caused by turbulence in the ocean. Let $\mathbf{u}$ be the velocity of an sea ice i, at time t:

$$\mathbf{u_i}(t) = \mathbf{u_i'}(t) + \overline{\mathbf{u_i}}(t) \ . \tag{4.1}$$

The fluctuating component of sea ice velocity, $\mathbf{u_i'}(t)$, is free of the influence of the mean flow [26]. Then, the fluctuating displacement of sea ice is obtained by integrating this fluctuating velocity in time [105],

$$x_i'(t) = x_i(t) - \frac{t}{T}\int_0^T u_i(t')dt', \tag{4.2}$$

where x_i is the position of an ice floe, and T is an averaging temporal window.

Once the influence of the mean flow is removed from the measurements, the absolute dispersion of sea ice, r'^2, can be calculated. Sea ice dispersion is defined as the displacement of sea ice from an initial position. Absolute dispersion is obtained by averaging this dispersion over the ensemble comprised of N ice floes:

$$\begin{aligned} r'^2 = \frac{1}{N-1}\sum_{i=1}^{N}\left[\ |x_i(t) - x_i(0) - \langle x_i(t) - x_i(0)\rangle|^2\ \right], \\ r'^2 = <\ [x_i'(t) - x_i'(t_0)]^2\ > \ . \end{aligned} \tag{4.3}$$

Here, $x_i(0)$ indicates its initial position of an ice floe. $\langle x_i(t) - x_i(0)\rangle$ denotes the influence of the mean flow.

The Lagrangian integral time scale, T_L is calculated by integrating the normalized velocity fluctuation autocorrelation function [103]

$$T_L = \int_0^\infty R(\tau)d\tau\ , \tag{4.4}$$

where τ is the lag time of consecutive trajectory points. The normalized velocity fluctuation autocorrelation function, $R(\tau)$, is defined as [26, 67]

$$R(\tau) = \frac{\langle \mathbf{u_i'}(\mathrm{t})\mathbf{u_i'}(\mathrm{t}+\tau)\rangle}{\langle \mathbf{u_i'}(\mathrm{t})^2\rangle} \, . \tag{4.5}$$

T_L is an important metric, as it can reveal the temporal regimes of the flow field. These regimes are characterized by different topological features. In isotropic and homogeneous 2D turbulence, tracers follow two distinct regimes, a ballistic and a diffusive regime [103]. These regimes can be identified by defining their absolute diffusion, the rate at which ice floes are being dispersed, as [16, 56]

$$\kappa(t) = \nu^2 \int_0^t R(\tau) d\tau \, , \tag{4.6}$$

where ν is the velocity variance $\langle \mathbf{u_i'}(\mathrm{t})^2\rangle$. To distinguish between dispersion regimes, the absolute dispersion can be written in terms of $R(\tau)$ [56]:

$$r_i'^2 = 2\nu^2 \int_0^t (t-\tau) R(\tau) d\tau \, . \tag{4.7}$$

At short time periods, i.e., $t \ll T_L$, dispersion is characterized by a ballistic regime. In this case, $R(\tau) \approx 1$, such that dispersion grows quadratically over time:

$$\begin{aligned} r_i'^2 &= 2\nu^2 \int_0^t (t-\tau) \cdot 1 \, d\tau \, , \\ r_i'^2 &\approx t^2 . \end{aligned} \tag{4.8}$$

If the mean flow is not properly removed from the residual velocities, dispersion will be affected. For example, when the mean flow is not removed, the absolute dispersion grows quadratically in time when the mean flow is comprised of a strong shear flow [26].

During a late-time limit, i.e., $t \gg T_L$, sea ice experiences random walk motion [103], known as a diffusive regime. In this regime, absolute diffusion is constant and can be defined as the time evolution of the absolute dispersion [16, 56],

$$\kappa(t) = \frac{1}{2}\frac{d}{dt}\langle r_i'^2 \rangle \ . \tag{4.9}$$

Combining equation 4.6 and 4.9:

$$\begin{aligned} \frac{1}{2}\frac{d}{dt} &= \nu^2 \int_0^\infty R(\tau) d\tau \\ r_i'^2 &= 2\nu^2 \int_0^\infty R(\tau) d\tau \ . \end{aligned} \tag{4.10}$$

At this long-time limit, if the integral of the normalized autocorrelation function, $R(\tau)$, converges to a constant value, i.e., $\beta = \int_0^\infty R(\tau) d\tau$, then dispersion grows linearly:

$$r_i'^2 = 2\nu^2 \, \beta \, t \ . \tag{4.11}$$

Both regimes, $t \gg T_L$ and $t \ll T_L$, have often been observed in oceanic flow. Rampal et al., [107] investigated the trajectory of 450 IABP drifters deployed between 1979 and 2001 over the entire Arctic basin. They observed that the absolute dispersion of their buoy

ensemble grew, first, quadratically in time following a ballistic regime. After 10 days, they observed a linear growth in their absolute dispersion measurements (diffusive regime). Rampal et al., [105] studied the trajectories of sea ice employing IABP buoys for three consecutive winter seasons (2007-2011). An integral timescale was found to be 1.71 days, where a clear transition between the ballistic regime and a diffusive regime was observed.

A third regime is of particular interest. This regime is observed at intermediate scales, between $2T_L$ and $30T_L$ [103]. In the past, this anomalous dispersion regime has been difficult to resolve in oceanic flow, mainly due to the inability to completely remove the influence of a background mean flow [56]. Known as an anomalous dispersion regime, it is observed if the integral of the normalized autocorrelation function does not converge to a constant value in equation 4.10. If that is indeed the case, dispersion is quantified by a power-law exponent, where $\alpha \neq 1$ or $\alpha \neq 2$:

$$r_i'^2 \propto t^{\alpha} \, . \tag{4.12}$$

Anomalous dispersion has been observed in both numerical simulations [9, 21] and experiments [120]. A power-law exponent of α=5/3 denotes dispersion in rotational (elliptic) regions. On the other hand, a power-law exponent of α=5/4 indicates regions associated with eddies, motion driven by shear and stretching [21]. For the first time, Rupolo et al., [115] observed the existence of anomalous dispersion subsurface floats in the Western North Atlantic. Later, Lukovich et al., [67] examined the trajectories of 22 ice beacons in the Beaufort Gyre (BG) during the 2007-2008 winter. The sea ice displacement was decomposed into zonal and meridional direction of the BG. Zonal dispersion, in agreement

with the strong zonal shear of the region, grew as t^2. An anomalous dispersion regime was identified when the team analyzed meridional dispersion, which followed a scaling law of $t^{5/4}$, characteristic of flow dominated by mesoscale eddies. The investigation found the integral time scales to be 1.2 days in the zonal and 0.7 days in the meridional direction.

Gabrielski et al., [26] performed an analysis on 29 Fram Strait Cyclones (FRAMZY) and Arctic Climate System Study (ACSYS) ice buoys deployed in the Fram Strait region in the winters of the years 2002, 2003, and 2007-2009. In addition, 49 IABP buoys were also tracked in the winters between 1988-2011. The absolute dispersion of the cross-stream component grew quadratically during short timescales (<3 days). Anomalous dispersion was observed at longer timescales, with a $\alpha = 5/4$ power law. The integral timescale calculated for the FRAMZY/ ACSYS ensemble was 0.45 days and 0.46 days for the IABP ensemble.

These studies established the framework to investigate sea ice dispersion using surface drifters in the Arctic oceans. However, despite the high seasonal atmospheric and oceanic variability in the region, neither seasonal nor annual distinctions in the data employed are taken into consideration in any of these studies [112, 153]. As such, a complete characterization of sea ice drift cannot be yet completed to understand the evolution of surface dispersion in MIZ. For the first time, the trajectories of sea ice derived from MODIS satellite imagery are employed to quantify the evolution of sea ice dispersion in the Fram Strait and Greenland Sea MIZ.

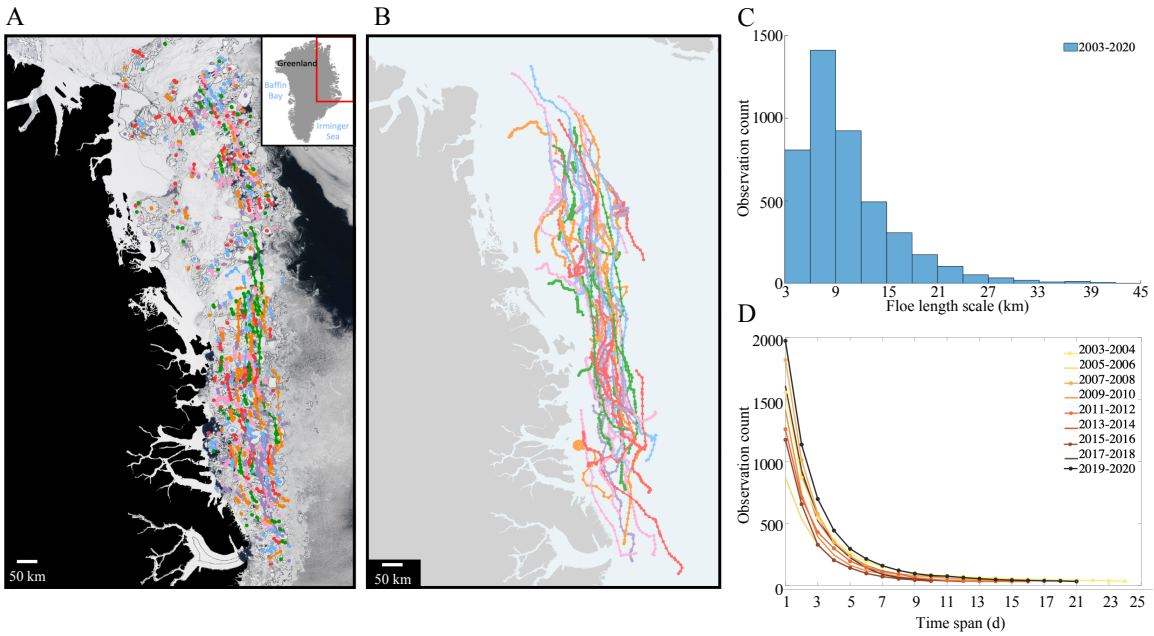

Figure 4.1: Sea ice observations. a) Retrieved trajectories of identified ice floes along the eastern Greenland coast. The background image corresponds to 14.05.2003, and all backward-in-time trajectories that include ice floe positions on that day are shown with colors. The position of the center of mass of each identified ice floe is marked with a circle, and the displacement vectors are presented with solid lines. b) Ice floe trajectories lasting over 30 days retrieved between March 31 and September 19 (2003 – 2020). c) Length scale distribution of detected sea ice floes. d) Time span of the Lagrangian trajectories analyzed to calculate absolute dispersion metrics.

4.2.2 Methods

To investigate the structure of the sea ice drift field within the MIZ, sea ice kinematics are quantified from remote sensing data to calculate the dispersion statistics of sea ice as single particles. First, sea ice must be identified and tracked from MODIS imagery. Next, the velocities of sea ice are calculated.

Calculation of sea ice Lagrangian trajectories and linear velocities

Sea ice is identified and tracked employing the methods developed in Chapter 2 [65]. Daily sea ice positions and velocity measurements are calculated. As such, for a given ice floe i, its instantaneous position $\mathbf{x_i}$ $\big(x_i(t),\, y_i(t)\big)$ and its instantaneous velocity, $\mathbf{u_i}$ $\big(u_i(\mathrm{t}),\, v_i(\mathrm{t})\big)$ are estimated with a temporal resolution of 24 hr. Here, $u_i(\mathrm{t})$ and $v_i(\mathrm{t})$ are the eastward and northward velocity components, respectively, along the Arctic polar stereographic projection axes. The trajectories of these ice floes are also recorded. An example is presented in Figure 4.1, where backward trajetories of sea ice identified on 14.05.2003 are displayed in different colors for ease of visualization.

An unprecedented number of sea ice trajectories were calculated and employed in this analysis, totaling 13,280. The captured trajectory lifetimes ranged from 2 to 90 days. Sea ice trajectories lasting over 30 days during our study are presented in Figure 4.1.B. The recovered sea ice dataset was composed of sea ice with length scales (taken as the square root of the surface area) which ranged from 3 to 42 km (Figure 4.1.C). Given the broad range of spatial scales, this dataset provided comprehensive sampling at the ocean surface across meso- to submeso-scales.

The large number of the observations allowed for the binning of the data into groups of two years. The number of sea ice floes used for this analysis is shown in Figure 4.1.D. When an ice floe is no longer tracked, it stops contributing to the dispersion analysis. The longer the trajectory, the harder it becomes to track that specific ice floe due to cloud coverage or

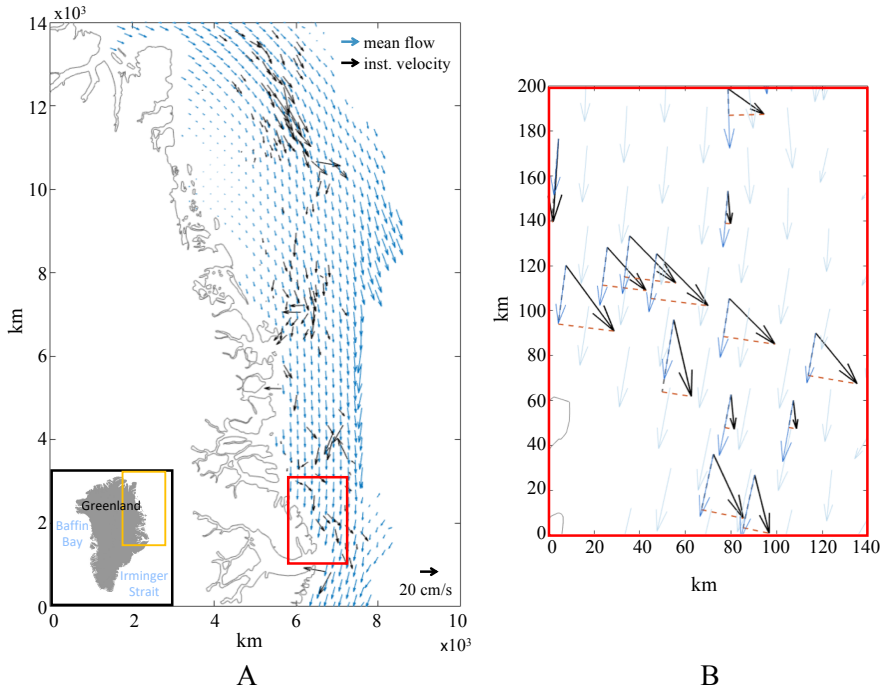

Figure 4.2: Mean velocity field. a) NSIDC mean velocity field calculated during the period from 05.04.2017 to 05.05.2017 (blue arrows) along with instantaneous velocity vectors captured from MODIS imagery on 20.04.2017 (black arrows). b) Zoomed-in area (red square) displays mean flow field calculated at locations of instantaneous velocities via a biharmonic interpolation (dark blue arrows). The orange dashed line indicates the cross-stream velocity component.

high deformation rates in the region. To ensure statistical integrity, the last point of the dispersion curve must contain at least 30 sea ice trajectories.

Calculation of sea ice mean velocity flow and absolute dispersion

To correctly parameterize the turbulent flow field via single-particle statistics, the influence of the mean flow field is removed from the MODIS-derived Lagrangian trajectories. There exist several approaches to achieve this. One way to calculate the mean flow of the region is by grouping observations into geographical bins of equal size. However, there are several factors to consider when doing so. For example, the dataset employed can have uneven

coverage and produce an array-bias [16]. Furthermore, the size of temporal and spatial bins must be selected carefully [56]. There have been several attempts to address this issue, including Rampal et al., 2009 and 2016 [105, 107]. In both studies, the smallest integral time and length scales that converged to a constant value were selected, i.e., selecting the smallest region containing the displacements r_i' as geographical and temporal bins are varied.

Another approach is to calculate Lagrangian averages from individual Lagrangian trajectories of the tracers. Zavala Sansón [151] calculated a mean velocity vector for each of their drifters by averaging retrieved velocities over a temporal window equal to the mean lifetime of their total drifters (45 days). Given that the trajectories in the present dataset are too short to assess a Lagrangian mean flow of individual ice trajectories, an additional sea ice product is employed. Daily velocity fields from the National Snow and Ice Data Center (NSIDC) 25 km sea ice drift product were used [135]. These Eulerian velocity fields are averaged over a dynamic temporal window of $T = 31$ days. As a result, each observation has an instantaneous velocity vector and a mean velocity vector derived from the NSIDC product.

The NSIDC product provides vertical and horizontal velocity components, $\mathbf{U}_{\mathrm{NSIDC}}(t)$ and $\mathbf{V}_{\mathrm{NSIDC}}(t)$, projected onto a NSIDC EASE-Grid North projection. To compute the zonal and meridional components of this data, the following rotation matrix is applied:

$$\begin{aligned} \mathbf{u}^{\mathrm{zon}}_{\mathrm{NSIDC}}(\mathrm{t}) &= \quad \mathbf{U}_{\mathrm{NSIDC}}(\mathrm{t}) \cdot \cos(L) + \mathbf{V}_{\mathrm{NSIDC}}(\mathrm{t}) \cdot \sin(L) \\ \mathbf{u}^{\mathrm{mer}}_{\mathrm{NSIDC}}(\mathrm{t}) &= -\mathbf{U}_{\mathrm{NSIDC}}(\mathrm{t}) \cdot \sin(L) + \mathbf{V}_{\mathrm{NSIDC}}(\mathrm{t}) \cdot \cos(L) \ . \end{aligned} \tag{4.13}$$

Here, L is the longitudinal coordinate of the vector in question. Thus, $\mathbf{u}^{\text{zon}}_{\text{NSIDC}}(\text{t})$ and $\mathbf{u}^{\text{mer}}_{\text{NSIDC}}(\text{t})$ are the converted velocity components along latitudinal lines and longitudinal lines on the Earth's surface, respectively. Finally, these geo-referenced components are transformed into a cartesian polar stereographic coordinate system, $\mathbf{u}_{\text{NSIDC}}(\text{t})$ and $\mathbf{v}_{\text{NSIDC}}(\text{t})$ [28].

The monthly mean velocity field for April 20, 2017 (T spans from April 5 to May 5) is displayed in Figure 4.2.a (blue arrows). The ice floes' instantaneous velocity vectors retrieved from MODIS images are displayed with black arrows in a zoomed area in Figure 4.2.b. The monthly mean velocity vector at the location of the MODIS observations is computed by means of a biharmonic spline interpolation. These vectors are shown with darker blue arrows in Figure 4.2.b. This interpolation method is ideal to calculate a mean velocity field of the ocean since it provides minimum-curvature interpolation of nonuniform data [116]. The resulting mean velocities are used to calculate the residual velocities of the tracked ice floes.

The velocity component parallel to the mean flow, $v^{||}_{ice}$, and the component perpendicular to the mean flow, v'_{ice} are calculated. The latter is displayed with orange dashed lines for each instantaneous velocity vector in Figure 4.2.b. A complete removal of the mean flow influence is impossible, and by only considering the perpendicular velocity v'_{ice} as the residual velocity, the influence of the mean flow field is excluded as much as possible [26]. v'_{ice} is then used to calculate sea ice absolute dispersion using equation 4.2 and is referred to as the fluctuating velocity component of sea ice henceforth.

The mean flow field was calculated by integrating the velocity flow field over a dynamic temporal window, T, of 31 days. The duration of 31 days was chosen to account for the variability of oceanic conditions of the region, i.e., eddy lifetime in the region is about 20 to 30 days [38]. To assess the chosen averaging window, the autocorrelation function of the velocity fluctuations was examined, see Figure 4.3.A. The rapid decrease and eventual convergence to 0 in the autocorrelation function is an indication that the correct averaging parameters were chosen to calculate a proper mean velocity field [105]. The autocorrelation function of the fluctuating velocities of the ensemble comprising the years 2003-2020 also rapidly decreases and eventually converges to 0 (Figure 4.3.A, inset).

4.3 Sea ice dispersion results and analysis

Sea ice dispersion is calculated employing the velocity fluctuations of sea ice, v'_{ice}, obtained from MODIS imagery. The absolute dispersion of sea ice revealed a dispersion growth following an anomalous dispersion regime (Figure 4.3.B). Error bars based on standard error, $\frac{\sigma}{N}$, where σ is the standard deviation of r'^2, are also presented. Each of the bi-yearly groups displayed a 5/4 power law growth behavior for time scales between 1 to 24 days (Figure 4.3.B. In addition, when binning all the observations into a single ensemble encompassing the years 2003 to 2020, the dispersion regime clearly followed anomalous dispersion from 1 to 41 days (Figure 4.3.B, inset). This dispersion growth regime is indicative of a flow field where shear and stretching dominate [9, 21]. In MIZ where meso/submeso-scales are known to influence

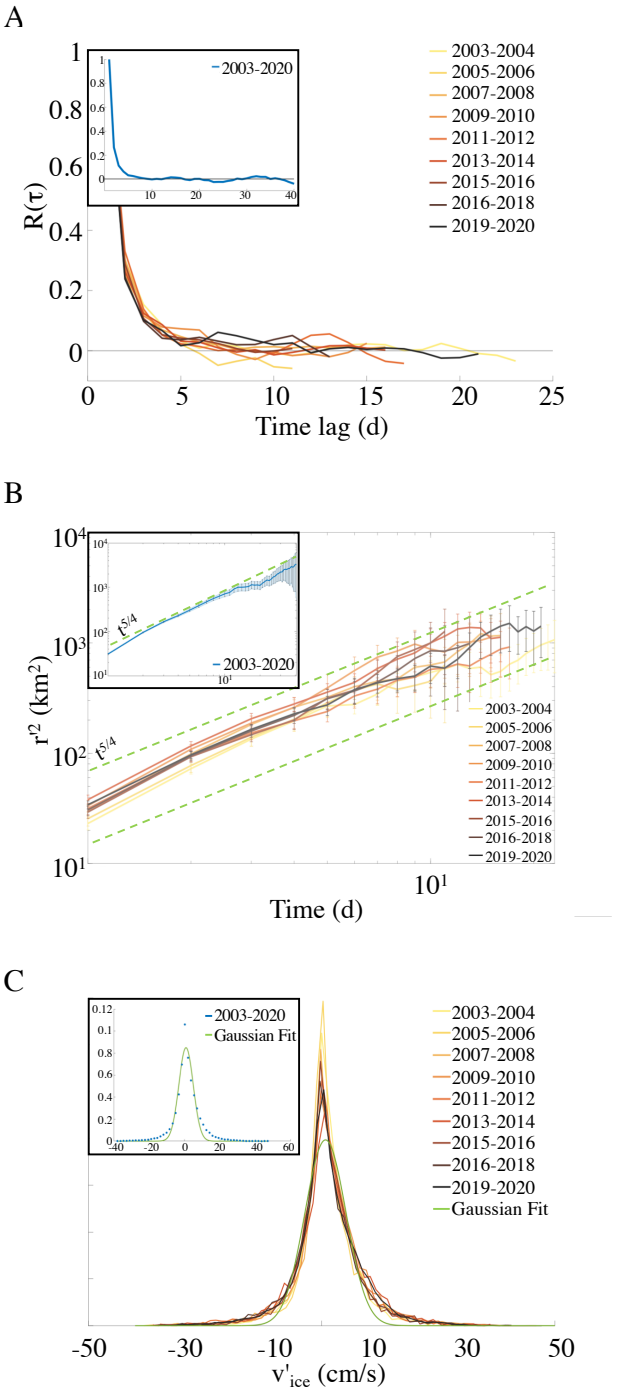

Figure 4.3: Single-particle dispersion statistics. a) Normalized autocorrelation functions v'_{ice}, binned into two-year groups. (Inset) v'_{ice} autocorrelation function of an ensemble composed of all the observations collected from 2003 to 2020. b) Absolute dispersion of sea ice calculated from v'_{ice}. Retrieved data is binned into two-year periods. The hyperbolic regime, $r'^2 \propto t^{5/4}$, is displayed for reference (dashed green line). (Inset) Absolute dispersion calculated for ensemble composed of all the observations collected from 2003 to 2020. c) Fluctuating velocity PDF for binned groups. Green line indicates a Gaussian distribution. (Inset) PDF of fluctuating velocities of an ensemble composed of all the observations collected from 2003 to 2020.

surface dynamics, this behavior indicates the effect of hyperbolic or elliptical regions of coherent structures on ice drift. A ballistic regime was expected at shorter timescales, but the regime cannot be captured due to the daily resolution of the measurements. Nevertheless, this demonstrates the ability to retrieve sea ice velocity fields from remote sensors to reveal the topology of the underlying flow field. The results presented here were in accordance to buoy studies in this region (e.g., [26]).

The integral time scale, calculated as $\int_0^{T_0} R(\tau)d\tau$, varies slightly between all years, from 0.7 to 1.2 days. In this region, the inertial oscillation frequencies vary from -1.885 to -1.975 cycle/d. This suggests that ice motion across-the-mean-flow is governed by timescales associated with oceanic phenomena and not by these high-frequency inertial oscillations [67]. In comparison, buoy studies such as [26] found values from 0.38 to 0.57 days in the Fram Strait region. The short timescales indicated forcing mechanisms associated with higher frequency processes. Furthermore, Lukovich et al., [67] calculated 0.7 days in the BG, while Colony et al., [13] measured integral time scales of 5 days in the Arctic basin. As these studies used different ways to remove the mean flow influence from their measurements, variation among studies was expected.

Furthermore, probability density functions (PDF) of the velocity fluctuations were calculated (Figure 4.3.C, inset). A Gaussian behavior of a PDF suggests a ballistic regime (random-walk) of sea ice dispersion. Analysis of the fourth-order-moment of the PDF revealed departures from Gaussianity. A Gaussian distribution would yield a kurtosis value of 3, whereas, for each of the bi-yearly groups, a kurtosis value was quantified ranging from

5.8 to 8.4. The 2003-2020 ensemble yielded a kurtosis value of 7.1 (Figure 4.3.C, inset). The PDF of the sea ice velocity fluctuations exhibited extended tails, reaching maximum values of 47 cm/s, which contributed to the high kurtosis. These high velocities can be associated with intermittent high energy events in the flow field, i.e., coherent structures [8].

Sea ice drift speeds were observed to be greatly affected by the rising temperatures. A strong correlation between the conditions of the sea ice field and its drift speed was found. To assess the conditions of the field, four regional monthly sea ice extent indices were calculated from different sources. Monthly mean sea ice cover values were calculated from (I) the Multisensor Analyzed Sea Ice Extent (MASIE) and the National Snow and Ice Data Center (NSIDC), (II) area, and (III) ice extent indices [22]. A fourth metric, the monthly means of sea ice export exiting Fram Strait was also calculated from (IV) Smedsrud et al., [118]. A strong correlation between these metrics was observed (Figure 4.4.A, grey). These four metrics were therefore used to describe the monthly ice cover conditions during our study period.

On seasonal time scales, sea ice drift speed was found to be highly correlated to the sea ice cover conditions (Figure 4.4.A). April and May had the highest values of sea ice drift speed every year, when the ice extent values were the highest. In the late summer months from July through September, the speed drift of sea ice decreases. These findings contradict the recent observations that sea ice speeds have increased as a result of decreasing sea ice concentrations in the Arctic basin [93]. When low sea ice concentration values in the central Arctic are observed, the response of sea ice to atmospheric forcing is more readily

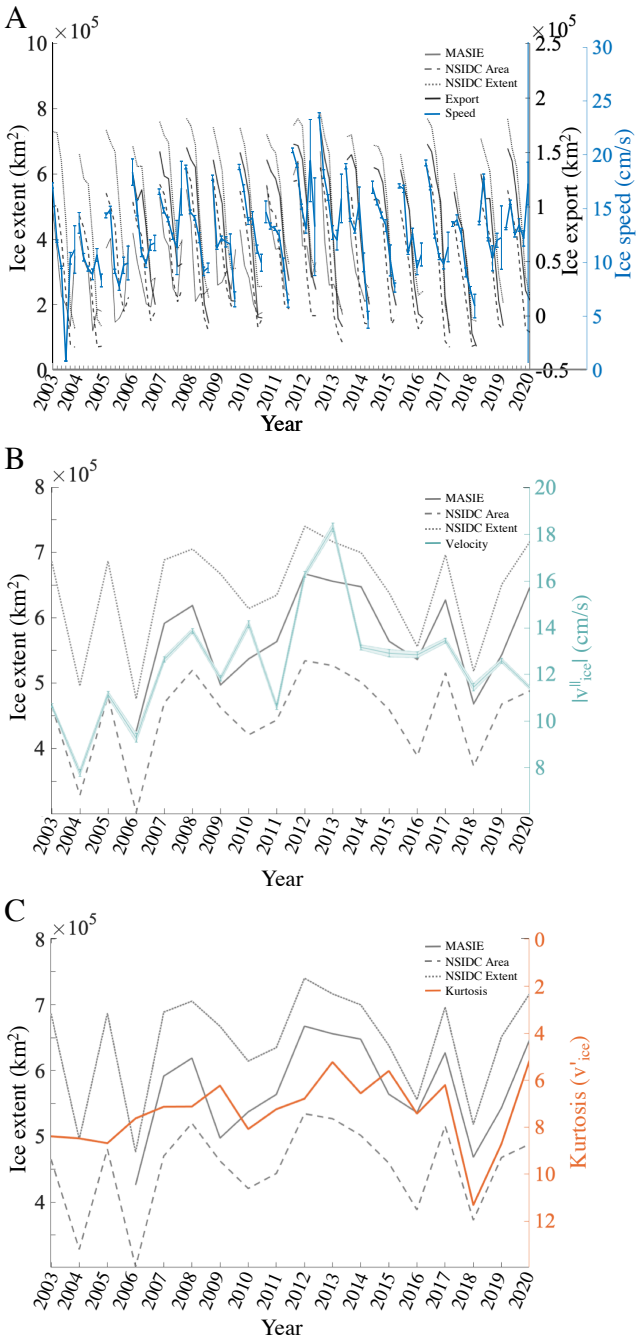

Figure 4.4: Sea ice field evolution a) Time series of monthly average values of sea ice extent from MASIE and NSIDC products plotted from April through September 2003-2020 (greys). Monthly sea ice export through Fram Strait from [118] plotted from April through September 2003-2014 (black). Monthly sea ice speed values from MODIS observations are also plotted (blue). b) Yearly average weighted values of sea ice extent from MASIE extent, NSIDC extent and NSIDC area (greys). Absolute mean $v^{||}_{ice}$ values of yearly ensembles plotted (green). c) Kurtosis values of PDF constructed from yearly-binned velocity fluctuations as a metric to turbulent events (orange). Notice the inverted right y-axis highlighting the anti-correlation between ice extent and kurtosis values of v'_{ice} PDF.

observed, allowing for larger drifting speeds. In MIZ, however, the opposite was observed. Lund et al., 2018 [71] suggested that sea ice wind stresses might have a stronger effect on consolidated ice than on thinner ice, which has a lower surface roughness and consequently is less responsive to wind forcing.

Finally, the inter-annual time scales of sea ice drift were explored. To that end, weighted average regional values of sea ice extent were calculated based on the number of observations for the Spring and Summer seasons of each year (April through September). These yearly values are presented in Figure 4.4.B-C, grey. The components of sea ice velocity vectors were examined against ice extent, i.e., along-the-mean-flow, $v_{ice}^{||}$, and across-the-mean-flow v'_{ice}. A strong correlation was found between $v_{ice}^{||}$ and the yearly sea ice extent values, R=0.7 (Figure 4.4.B). Of particular interest was the anti-correlation, R=-0.6, found between sea ice cover and the kurtosis values calculated from v'_{ice} PDF (Figure 4.4.C).This behavior can be explained by the relationship between sea ice cover and the submesoscale eddy field. As the sea ice cover decreases, submesoscale eddy activity in the ocean is predicted to increase [138]. The kurtosis values of v'_{ice} found in this investigation serve as a metric to quantify the variability and departure from Gaussianity of sea ice motion. Sea ice cover is known to suppress eddy formation [81]. Therefore, a diminishing sea ice cover results in higher kurtosis values of the v'_{ice} PDF. A predicted ice-free central Arctic will consequently result in an intensified eddy field in the future, similar to the currently observed trends in MIZ.

4.4 Conclusions

In this chapter, the structure of the sea ice field within the MIZ was investigated by quantifying the dispersion statistics of sea ice. The dynamical regime of the sea ice drift field was assessed via a single-particle dispersion analysis. To this end, Lagrangian trajectories of sea ice derived from MODIS imagery were considered along the eastern coast of Greenland. First, the fluctuating velocity of sea ice was recovered by removing the influence of the mean flow. Only the cross-stream component of velocity was considered.

After grouping the data into bi-yearly groups, each of the groups displayed an absolute dispersion growing with a power-law of 5/4. This absolute dispersion regime is known as so-called hyperbolic regime. These findings suggest that sea ice transport (without the influence of a mean flow) is associated with oceanic eddies. Recent observations and numerical simulations have suggested that submesoscales can drive the state and dynamics of sea ice. Therefore, the results provide direct evidence of the importance of meso/submeso-scale turbulence on sea ice transport in MIZ.

Oceanic survey studies often fail to make clear inter-seasonal and inter-annual distinctions to quantify absolute dispersion despite the drastic changes observed in oceanic and atmospheric conditions from season to season and from year to year in the Arctic [112, 153]. To retain statistical integrity, instead, these studies group all the available data of a region into a single statistical ensemble (e.g., [105, 107]). The critical advantage of employing MODIS data is the large number of retrieved sea ice measurements. This allowed for the examination

of inter-annual variability of sea ice dispersion, which was examined for almost two decades along the eastern coast of Greenland. A strong correlation between the conditions of the sea ice field and its drift speed was found. Monthly mean sea ice cover indices were calculated from various sources. On seasonal time scales, sea ice drift speed was highly correlated to the sea ice cover conditions. For the months of April and May, the highest values of sea ice drift speed were recovered every year. On the other hand, in the late summer months of July through September, sea ice speeds decreased to their lowest values. Lastly, sea ice fluctuating velocities varied according to the sea ice cover. This suggested that the amount of high-energy turbulent events in the sea ice flow field increases with a receding ice cover. This is in accordance to the results presented in Chapter 3, where the rotation variance of sea ice was employed as a metric to characterize the small scale-eddy energetics of the flow field.

Chapter 5

Lagrangian statistics of *in-situ* and remote sensing sea ice observations in marginal ice zones

5.1 Introduction

Whether chemical, biological, or artificial, the dispersion of surface tracers can be used to understand the underlying turbulent processes driving their motion. Globally, these turbulent mechanisms have been thoroughly investigated. However, their small size, along with the harsh conditions in the Arctic, have made it difficult to fully understand them and their role in sea ice transport. Leveraging the unique opportunity to employ unprecedented drifter data in concert with satellite images, this chapter investigates the surface circulation of the

Greenland Sea. Both datasets provide important information to understand the ocean surface circulation in regions where direct ocean measurements are challenging to obtain. Moreover, the scales associated with the spread of surface drifters can provide useful information to advance accurate modeling and forecasting of sea ice conditions in the Arctic.

In 2020, rising temperatures and extreme weather events decreased the Arctic ice extent by almost 40% from the 1981-2010 satellite record mean [97]. This rapid ice loss has already begun to transform the region, e.g., marginal ice zones (MIZ) continue to increase in size, duration, and influence over the Arctic climate system [124]. MIZ are important regions along the ice edge where meso- ($R_0 \sim O(-1)$) and submeso-scale ($R_0 \sim O(1)$) variability strongly influences the sea ice field and vice versa. Understanding how sea ice and ocean currents evolve in MIZ is thus crucial to fully characterize the mechanisms controlling surface dispersion and thus the mechanisms transforming the new Arctic.

A complete understanding of the multiscale features driving the sea ice and ocean flow fields is challenging. Globally, coherent structures driving surface circulation have been thoroughly investigated through altimetry data. However, these observations are obstructed by the presence of ice in the Arctic regions. Although many methods exist to recover oceanic measurements from areas of open water over the sea ice cover [4, 54], long-term high-resolution measurements remain unavailable. For these reasons, tracer transport across geostrophic surface currents has become an important tool to investigate the signature of the underlying flow circulation in polar oceans. The wind forcing on drifters and surface currents occurs simultaneously near coastal zones and thus wind forcing does not affect

drifter dispersion [83, 100, 101]. Moreover, the sea ice dynamics are in quasi-equilibrium with the underlying oceanic eddy field in MIZ [75]. Minimally affected by wind forcing, Lagrangian drifters thus serve as an important indicator to gauge the evolution of meso-/submeso-scale physical processes in rapidly changing Arctic MIZ. In this work, we have the unique opportunity to employ high resolution *in-situ* Lagrangian measurements and, for the first time, satellite-derived Lagrangian trajectories of sea ice as surface drifters.

Dating back to work by Colony et al., 1984 and 1985 [13, 14], sea ice has been employed as a tracer to characterize the properties of the underlying flow field via statistical analysis, namely single- and two-particle dispersion [110, 128]. Single-particle dispersion, also known as absolute dispersion, describes the structure of the drift field by quantifying the rate at which a tracer moves away from its original position. If the resolution of the measurements allows it, different regimes in the absolute dispersion of the tracers can be identified, revealing the topology of the underlying flow field. At short time scales, the particles are expected to be advected by the mean flow, known as the ballistic regime [56]. During a late-time limit, the tracer experiences random walk motion known as a diffusive regime. These regimes have been readily resolved in oceanic measurements [16, 56, 57, 107].

At intermediate scales, the presence of anomalous regimes associated with shear and stretching by mesoscale eddies has been observed in numerical simulations, experiments, and oceanic surveys [9, 21, 26, 37, 46, 67, 103, 151].

Meanwhile, a more comprehensive characterization of the flow field across broader length scales can be accomplished by quantifying the relative dispersion of surface tracers.

Two-particle dispersion quantifies the rate at which two tracers move away from each other. Along with relative diffusivity, these metrics can describe the mixing and stirring characteristic length scales of the turbulent flow [56]. At length scales smaller than the Rossby radius of deformation, R_0, particles drift away driven by coherent structures larger than their separation distances. This process is known as nonlocal relative dispersion. At larger scales, two local dispersion regimes can be observed: a ballistic regime and a Richardson regime. These occur when relative dispersion is dominated by eddies whose length scales are similar to the pair separation distances. Lastly, a random walk, or diffusive regime, is recovered when the two particles are uncorrelated and their separation distances exceed the eddy length scales.

Relative dispersion has been explored in various oceanic studies, [15, 46]. Nevertheless, the observational difficulties arising from the small R_0 found at high latitudes can make nonlocal dispersion challenging to resolve. Koszalka et al., [46] explored the relative dispersion of POLEWARD experiment surface drifters in the Nordic Seas from 2007 to 2008. The team resolved three regimes, including a submesoscale regime within the first two days and up to 10 km. Next, they recovered a Richardson regime from 2 to 10 days and 10 to 100 km. A diffusive regime was lastly recovered when the separation distances were greater than 100 km. Meyerjürgens et al., 2020 [83] employed surface drifters in the North Sea. The team resolved a nonlocal dispersion regime at scales smaller than 10 km, followed by a ballistic relative dispersion regime and a Richardson regime in the final phase of their data.

Building on the framework of these studies, the structure of the sea ice drift field is investigated within the MIZ by quantifying the dispersion statistics of sea ice from *in-situ* field campaigns and remote sensing Lagrangian data. A relative dispersion analysis in the Fram Strait region has not been performed yet. Moreover, studies in absolute dispersion statistics are limited to one investigation [26]. This is due, in part, to the limited number of buoy deployments in the region. In this study, the opportunity to employ data from one of the largest Arctic research expeditions was employed. The recent Multidisciplinary drifting Observatory for the Study of Arctic Climate (MOSAiC) campaign collected unprecedented data as the research vessel exited the Arctic through the Transpolar drift into the Fram Strait region from 2019 to 2020. In addition, Moderate Resolution Imaging Spectroradiometer (MODIS) imagery is leveraged to recover valuable daily Lagrangian observations of sea ice at moderate spatial resolutions. MODIS images represent the longest record of Earth ever compiled and provide a continuous view of the evolution of sea ice drift since 2003 [147]. The MOSAiC Lagrangian data, in concert with MODIS imagery, offers an extensive number of sea ice measurements to investigate one- and two-particle pair statistics.

This chapter is organized as follows. The region of interest and data are briefly described in Section 5.2. In section 5.3, the methodology to calculate the dispersion metrics of the datasets is presented. Lastly, the results are given in Section 5.4, followed by a discussion and conclusions in Section 5.5.

5.2 Study area and data

5.2.1 Study area

The study focuses on the MIZ south of Fram Strait along the eastern coast of Greenland (70° to 85°N, -30° to 20°E), Figure 5.1a. This region is an important component of the Arctic climate system. As described in previous chapters, in this region, warm and salty Atlantic waters meet colder and fresher polar waters, supplying nutrients and controlling the heat and freshwater budget of the region [33]. An estimated 14% of the total Arctic sea ice volume exits through Fram Strait each year via the East Greenland Current (EGC), which is the main southward current in the region [121]. Together with strong winds, the EGC transports over 90% of the ice that exits the Arctic into MIZ, making this region the largest and most concentrated meridional sea ice flow in the world [114, 139]. Here, the first baroclinic Rossby deformation radius, R_0 is approximately 5 km [92], suggesting eddy wavelengths in the order of $2\pi R_0$. Eddies have been reported to range within 20-40 km with a lifetime of 2-3 weeks [38, 142]. Larger eddies have also been detected, reaching 80-90 km and lasting no more than 10 days [48]. Atmospheric vortices develop at large spatial scales (200–1000 km in diameter) and quick time scales (1-2 days) [143].

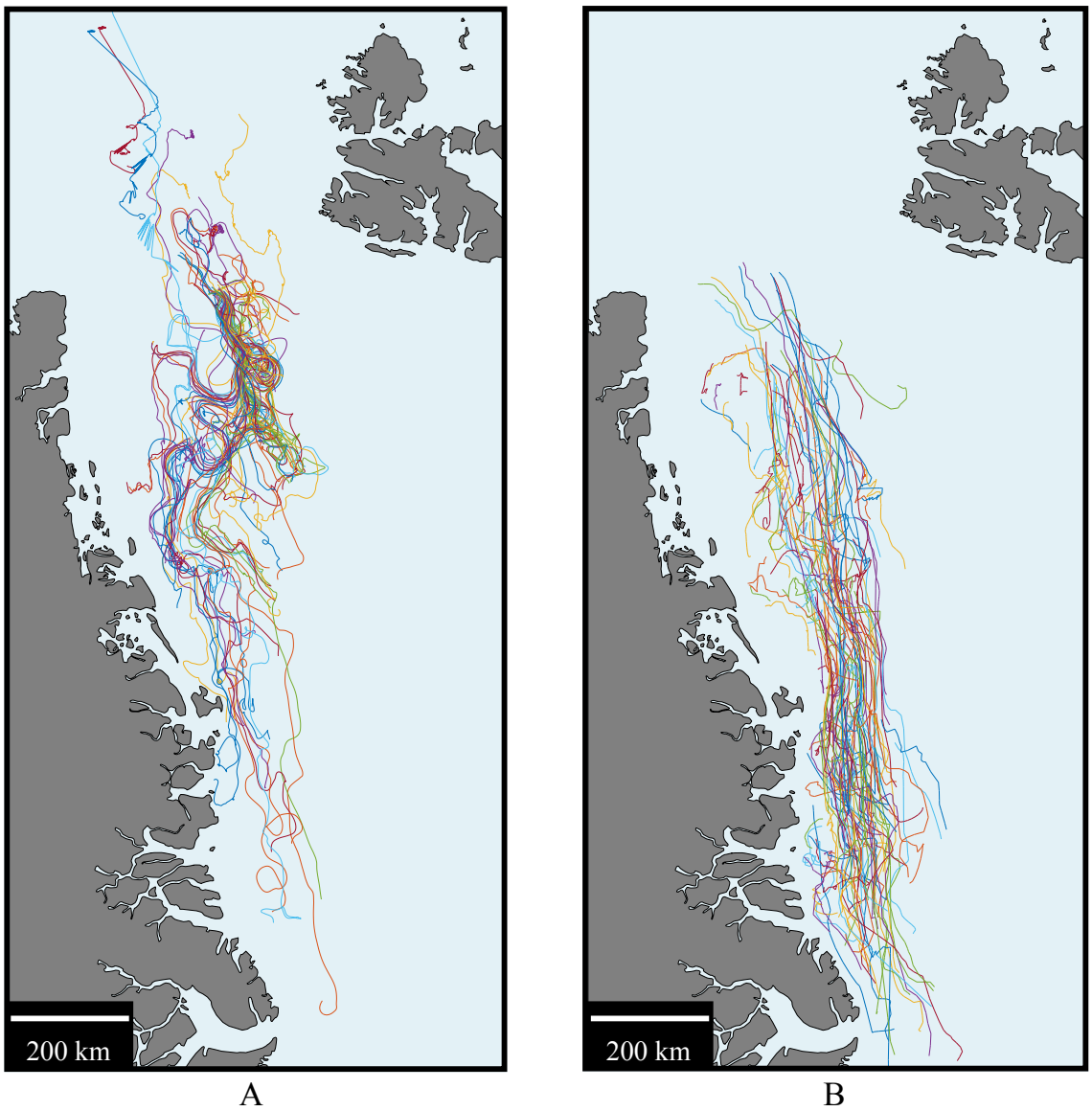

Figure 5.1: Study Region. a) Map of the east Greenland region with 104 MOSAiC buoy trajectories captured during the MOSAiC mission. b) Collapsed map of the east Greenland region with sea ice trajectories derived from MODIS imagery from 2003 to 2020. Only trajectories of sea ice tracked over 25 days are displayed.

5.2.2 Sea ice Lagrangian buoys

The recent MOSAiC campaign collected unprecedented Arctic sea ice data [1]. As the research vessel Polarstern exited the Arctic basin in the transpolar drift, ice tethered platforms, or buoys, were deployed along the vessel's trajectory. In total, an array of over 200 GPS drifting buoys was deployed in a distributed network, capturing scales of sea ice motion from hundreds to thousands of meters from the Siberian coast to the Greenland Sea. The deployment of the first buoy occurred on September 26, 2019, while the last measurement was received on April 19, 2021.

Different types of drifting sensors were deployed during the mission, including CALIBS (which measure temperature, barometric pressure, and position), Modular Sea Ice Buoy (which have sensors to measure barometric pressure, temperature and humidity, temperature, salinity, camera, position, etc), Surface Velocity Profiler (which measure temperature, barometric pressure, and position), among others. Consequently, the transmission frequency of each buoy varied from 15 min to 4 hrs. Therefore, the positions of each buoy with different sampling frequencies are interpolated to obtain uniform hourly positions.

The influence of tides and high-frequency inertial oscillations on buoy motion can be captured due to the hourly resolution of the drifters. The Coriolis parameter is defined as $f = 2\Omega sin(\phi)$, where the rotational speed of Earth, $\Omega = 1.002736$ cycles per day, and ϕ is the latitude. As such, the inertial frequency varies from -1.885 to -1.975 cycle per day in our study region. Therefore, one inertial period corresponds to approximately 12 hrs. To

[1] https://mosaic-expedition.org

remove the effects of high-frequency inertial oscillations, a time-averaging operation on buoy locations over a moving time window of 12 hrs is performed.

Finally, due to the high seasonal and regional variability of the Arctic, only the sections of the MOSAiC trajectories transitioning over MIZ (sea ice concentrations below 80%) during the spring and summer seasons are considered. When large gaps in the position data of buoys were found, the trajectory was stopped during this analysis. On average, while constraining the buoys to these conditions, the buoys have a lifetime of 30 ± 19 days and cover a distance of 363 ± 244 km. This results in a total of 104 buoys, for which trajectories are mapped in Figure 5.1.A. This dataset is referred to as MOSAiC buoys hereafter.

5.2.3 Sea ice remote sensing observations

Complimenting the MOSAiC buoy dataset, the MODIS-derived Lagrangian sea ice trajectories of sea ice derived in previous chapters are employed. To summarize, the MODIS images were directly downloaded from the open-access Earth Observing System Data and Information System (EOSDIS) Worldview platform. These georeferenced images have a moderate resolution (250 m) and are projected onto an Arctic polar stereographic projection (WGS 84/NSIDC Sea Ice polar Stereographic North 70° N). Daily Corrected Reflectance True Color and Corrected Reflectance False Color images are used. Each of these images is composed of three bands corresponding to RGB channels, namely band 1 (620– 670 nm), band 4 (545–565 nm), and band 3 (459–479 nm) for the former and band 7 (2105–2155 nm), band 2 (841–876 nm), and band 1 (620–670 nm) for the latter. To extract the Lagrangian

trajectories of sea ice, the methodology developed in Chapter 2 is employed. A total of 13,280 ice floe trajectories were obtained, with length scales ranging from 4 to 65 km, of which 180 ice floes had trajectory lifetimes longer than 20 days. This last subset is displayed in Figure 5.1.B. The satellite-derived Lagrangian sea ice trajectories are referred to as MODIS sea ice henceforward.

5.2.4 Sea ice mean flow field

To investigate the structure of the underlying flow field via single-particle dispersion, the influence of the mean flow field is first removed. Several methods exist to do so [26, 107, 151]. Following Gabrielski et al., [26], the National Snow and Ice Data Center (NSIDC) sea ice drift product is employed [22]. The NSIDC provides daily Eulerian fields (25 km of resolution) from 1978 to the present day. The mean flow field is estimated by averaging NSIDC daily velocity vectors considering a moving temporal window, $\overline{T}$, of 31 days. The value of $\overline{T}$ is chosen to account for the variability of oceanic and atmospheric conditions of the region, i.e., eddy lifetime in the region is about 20 to 30 days [38].

5.2.5 Sea ice concentration

Daily sea ice concentration values were employed to estimate the day correspoding to when a MOSAiC buoy entered the MIZ. Sea ice concentration estimates are quantified from NSIDC MASIE-AMSR2 (MASAM2) 4-km product. The product blends sea ice concentration data from the Multisensor Analyzed Sea Ice Extent (MASIE) product and the

Advanced Microwave Scanning Radiometer 2 (AMSR2), with grid cell sizes of 4 and 10 km, respectively. The product covers July 2012 to present day [23].

5.3 Theory review and methodology

The surface dispersion of Lagrangian drifters is investigated in the Fram Strait and the Greenland Sea MIZ. Whether MOSAiC instruments or MODIS-derived sea ice, the locations of these surface tracers are statistically analyzed to describe the topology of the flow field. These measurements are projected onto an Arctic polar stereographic projection (WGS 84/NSIDC Sea Ice polar Stereographic North) to calculate their horizontal and vertical velocity components along these projection axes.

First, the dispersion statistics of sea ice via absolute dispersion are considered. The displacement of the drifters from their initial positions is calculated. Next, two-particle dispersion of the drifters is analyzed by pairing buoys as they approach each other. The relative dispersion and diffusion of both drifter ensembles are estimated. Lastly, the so-called finite-scale Lyapunov exponents are quantified, allowing for the calculation of relative dispersion rates with distance as an independent variable [56, 58]. A brief theory review and methodology is presented next.

5.3.1 One-particle statistics

The absolute dispersion, r'^2, of the flow field is obtained by averaging the displacement of particles over an ensemble comprised of N surface drifters [128],

$$r'^2 = \frac{1}{N-1} \sum_{i=1}^{N} [\, x_i'(t) - x_i'(t_0)]^2 \,, \tag{5.1}$$

where $x_i'(t)$ and $x_i'(t_0)$ are the residual positions of drifter i after the influence of the mean flow has been removed at time t and at an initial reference time t_0, respectively. In this study, the MOSAiC buoys will form an ensemble while the MODIS sea ice will comprise a second ensemble.

In order to remove the influence of the mean flow, the monthly mean flow field velocity employing the NSDIC 25 km sea ice drift product is employed. The mean flow fields were interpolated over the locations of every observation. Following Gabrielski et al., [26], the Lagrangian velocities from the particles are projected in the direction of the mean flow. The across-mean flow velocity component is considered the velocity fluctuation, $u_i'(t)$. Finally, Equation 5.1 is obtained by integrating $u_i'(t)$ in time to obtain $x_i'(t)$ [105]. The displacement vectors caused by the velocity fluctuations in the cross-stream direction of the flow field are presented in Figure 5.2.A and 5.2.B for MOSAiC buoys and MODIS sea ice, respectively.

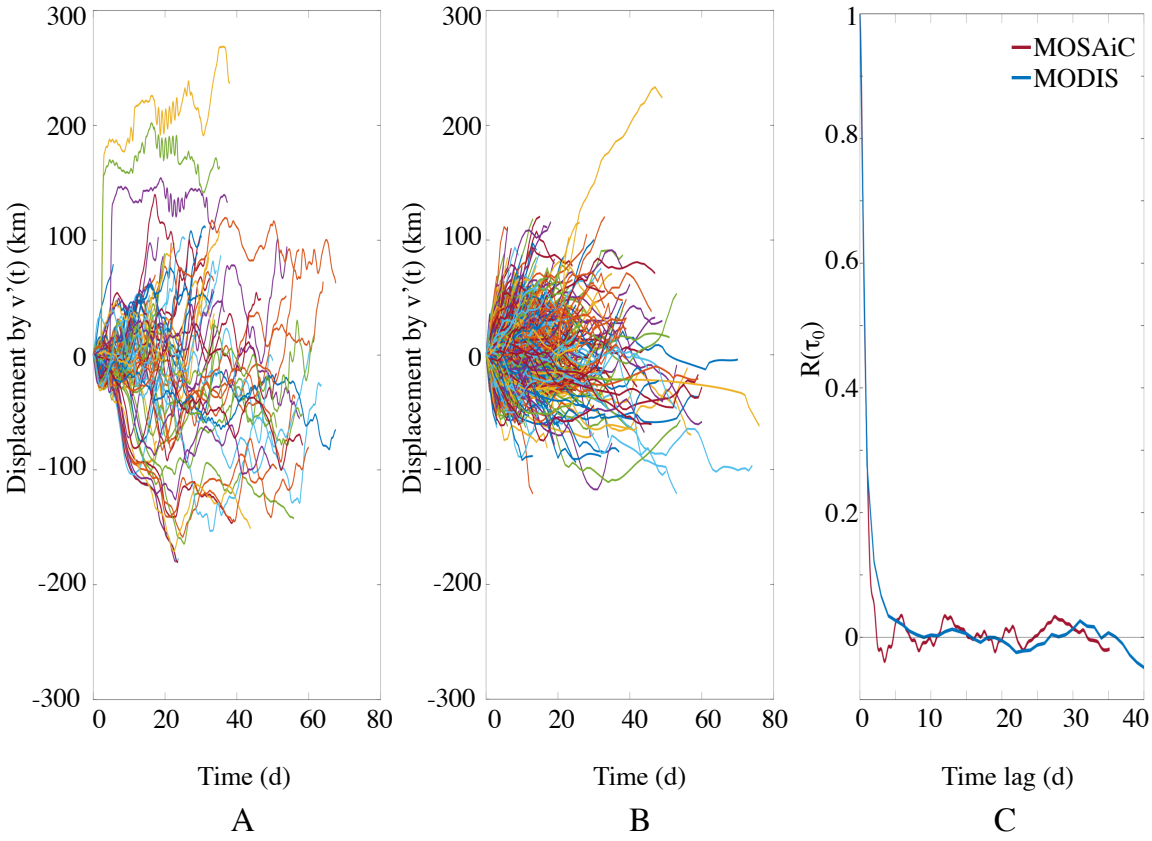

Figure 5.2: Displacements by velocity fluctuations. a) Cumulative displacements of the MOSAiC buoys considering only the velocity fluctuations (cross-stream). b) Cumulative displacements of the MODIS sea ice considering only the velocity fluctuations (cross-stream). d) Normalized autocorrelation function of velocity fluctuations from MOSAiC buoys (red) and MODIS sea ice (blue).

Absolute dispersion

If the data resolution is sufficient and the influence of the mean flow field has been properly removed, distinct dynamical regimes in the absolute dispersion function can be observed. At short time scales, dispersion is characterized by a ballistic regime, where r'^2 grows quadratically. The ballistic dispersion regime is observed at timescales smaller

than Lagrangian integral timescale, T_L. The autocorrelation of fluctuating velocities, R, is calculated as

$$R = \frac{\langle \mathbf{u_i'}(\mathrm{t})\mathbf{u_i'}(\mathrm{t}+\tau_0)\rangle}{\langle \mathbf{u_i'}(\mathrm{t})^2\rangle}\,, \tag{5.2}$$

where τ_0 corresponds to zero lag. The autocorrelation functions of MOSAiC buoys and MODIS sea ice are presented in Figure 5.2.C. T_L is thus defined as

$$T_L = \int_0^{t_z} R(\tau_0)\, d\tau_0\,, \tag{5.3}$$

where t_z is taken as the first-zero crossing of R. T_L for the MOSAiC buoys was calculated to be 0.80 days, while T_L for the MODIS sea ice was 1.06 days. This discrepancy is attributed to the hourly resolution of MOSAiC buoys compared to the daily resolution of MODIS sea ice measurements. In comparison, Gabrielski et al., [26] found values from 0.38 to 0.57 days in the Fram Strait region, meanwhile, Lukovich et al., [67] calculated 0.7 days in the Beaufort Gyre and Colony et al., [13] estimated a velue of 5 days in the Arctic basin.

At intermediate scales, anomalaous absolute dispersion is expected, namely an elliptic and hyperbolic regime, with $r'^2 \propto t^{5/3}$ and $r'^2 \propto t^{5/4}$, respectively. The hyperbolic regime corresponds to the scales at which the flow is dominated by shear and stretching, characteristic of coherent vortices [9, 21, 103].

Finally, at longer timescales, $T \gg T_L$, dispersion is characterized by a diffusive regime. This regime is also known as the random-walk regime, where $r'^2 \propto t$. The dispersion regimes are summarized in Table 5.1.

5.3.2 Two-particle statistics

The relative dispersion of surface drifters along MIZ is next investigated. For the MOSAiC ensemble, buoy pairing is assigned as they approach each other, regardless of their deployment date or location. Buoys are considered pairs if they approach each other at a distance ranging from 650 m to 1 km in order to maximize the number of buoy pairs identified while still capturing short separation scales.

MODIS sea ice floes are also paired according to their separation distances. Due to the coarser resolution of MODIS measurements, a sea ice pair is defined as two ice floes located at a maximum initial separation distance of 20 km. This results in the pairing of 62 ice floes with trajectories longer than 10 days.

Relative dispersion and diffusivity

Relative dispersion, D^2 is calculated by measuring the separation distance between two drifters in time:

$$D^2 = \frac{1}{N} \sum_{i \neq j}^{N} [\, x_i(t) - x_j(t)]^2 + [\, y_i(t) - y_j(t)]^2 \,, \tag{5.4}$$

where x and y are the vertical and horizontal position components along the stereographic projection axis of i and j drifter pairs. The scaling components of relative dispersion give insight into the oceanic topology as drifters spread from a center of mass, providing information into the energy scales associated with the flow field. Two-dimensional turbulence predicts that, at the inertial range where enstrophy cascades to smaller scales, the energy

spectrum, κ, scales with a κ^{-3} dependence [56]. The pair relative dispersion will grow exponentially, $D^2 \propto e^t$ [10, 49, 62]. This so-called nonlocal dispersion occurs because the separation of the pairs is much smaller than the scale at which the energy is injected into the system.

Relative dispersion behaves like absolute dispersion at small and large scales. A ballistic behavior is present when $D^2 \propto t^2$, associated with the local shear of the flow field. A diffusive regime can be recovered if the separation distance of the pairs is larger than the biggest eddies in the region. Therefore, the pair particles are not correlated and their separation grows as a random walk where $D^2 \propto t$.

At intermediate scales, in 2-D turbulence, the energy spectrum cascades at a constant rate of $\kappa^{-5/3}$ towards large scales [49, 56]. This yields a separation rate regime predicted by Richardson's law, where dispersion grows cubically in time up to a length scales comparable to the largest eddies in the region, $D^2 \propto t^3$ [110]. This inertial regime is known as local dispersion since the spreading rate of the pairs is driven by coherent structures comparable in length scales to the pair separation.

The relative diffusivity of the drifters, Y, is defined as the rate of change of relative dispersion. Y measures how fast the system grows in time,

$$Y = \frac{1}{2}\frac{d}{dt}D^2. \tag{5.5}$$

Of particular interest is the diffusivity regime growing under Richardson's law, as this can describe the scales in the flow of the energy-containing eddies. Richardson's law thus

indicates that, at certain length and time scales, the stirring of the particles is driven by eddies comparable in scale to the separation of the particles (local diffusivity). This regime is characterized by $Y \propto D^{4/3}$. Nonlocal diffusivity is characterized by $Y \propto D^2$ [56].

Finite-scale Lyapunov exponents

Artale et al., [5] introduced a finite size metric, $\tau(\rho)$, to describe the Lagrangian motion of particles enclosed in a basin. In this scheme, the main goal is to calculate the time it takes two particles to separate a distance $\tau(\rho)$, rather than quantifying their separation distances as time progresses. Making distance an independent variable is helpful to avoid binning particles under an incorrect dispersion regime.

The Finite-scale Lyapunov exponents are defined as

$$\lambda(\delta) = \frac{log(\rho)}{\left\langle T(\delta) \right\rangle}, \tag{5.6}$$

where T(δ) corresponds to the time it takes for by a pair of drifters to separate from a distance δ to a larger distance $\rho\delta$. Following [15, 58, 151], the scaling factor is defined as $\rho = \sqrt{2}$. FSLE allow for the exploration of every possible initial separation within the buoy trajectories. Therefore, every time the drifters cross an initial separation distance scaled by $\rho = \sqrt{2}$ is taken into consideration. This increases the number of data points and improves the statistical integrity in the calculations [70].

The Richardson regime is observed at scales where the FSLE function plotted against drifter separation distance decreases at a rate $\propto \delta^{-2/3}$. An advantage of analyzing the flow

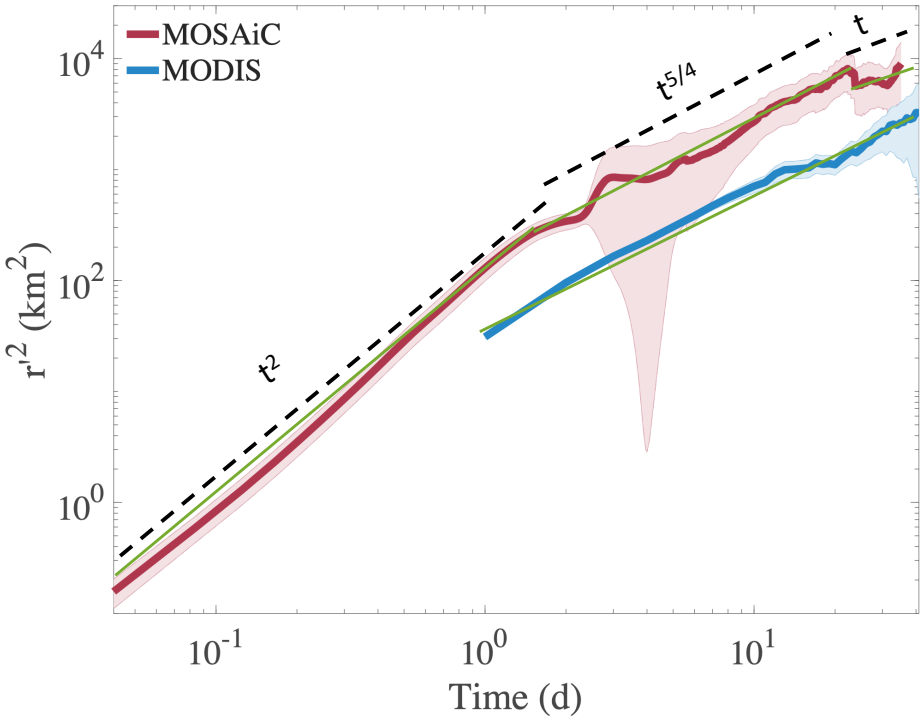

Figure 5.3: Absolute dispersion. Absolute dispersion of MOSAiC buoys (red) and MODIS sea ice (blue). Green lines are estimated fits, while dashed lines represent the theoretical absolute dispersion regimes: ballistic ($r'^2 \propto t^2$), anomalous ($r'^2 \propto t^{5/4}$), and diffusive ($r'^2 \propto t$). The shading corresponds to 95% confidence intervals.

field via FSLE is that the diffusivity can be readily recovered, $Y(\delta) = \lambda\delta^2$ [5]. As mentioned before, nonlocal relative diffusivity is distinguished by $Y(\delta) \propto D^2$, while local diffusivity scales as $Y(\delta) \propto D^{4/3}$.

5.4 Sea ice absolute and relative dispersion analysis

5.4.1 Absolute dispersion

A total of 104 MOSAiC drifting buoy trajectories were employed, along with 13,280 MODIS-dervided sea ice trajectories to calculate the absolute dispersion along Fram Strait and the north-east Greenland Sea (Figure 5.3). Each dispersion point has a minimum of 30 drifters, respectively. Given the high temporal resolution of the MOSAiC buoys, a ballistic regime was observed from the beginning up to 1.5 days. The estimated fit is $216.0t^{2.01}$.

A transition in regimes was observed next. This anomalous regime lasted from 1.5 to 23 days for MOSAiC buoys, with an estimated fit of $159.0t^{1.25}$. The same result was obtained with MODIS sea ice trajectories, with an estimated fit of $35.5t^{1.21}$. Both datasets confirm the presence of anomalous dispersion at similar scales in this region. MODIS sea ice showed an anomalous dispersion that persists until the end of the timeseries. The MOSAiC buoys, on the other hand, displayed a transition at the final stage of the absolute dispersion curve (estimate fit $379.5t^{0.84}$). As expected from theory, absolute dispersion should grow linearly at large scales.

5.4.2 Relative dispersion

Three different regimes were discerned in the relative dispersion function of MOSAiC buoys (Figure 5.4.A). First, an exponential growth from 0 to 2 days is observed. This exponential

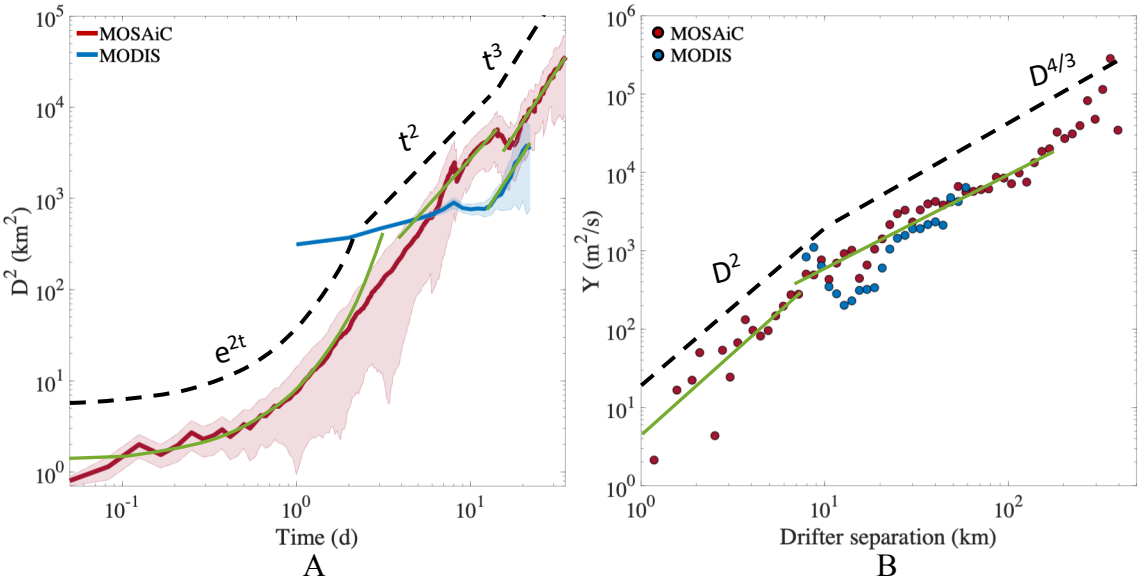

Figure 5.4: Relative statistics. a) Relative dispersion of sea ice from MOSAiC buoys (red) and MODIS sea ice observations (blue). The shaded region indicates the 95% confidence limits for MOSAiC buoys and the 75% confidence limits for MODIS sea ice. Green lines are estimated fits, while dashed lines represent the theoretical relative dispersion regimes: nonlocal ($D^2 \propto e^t$), ballistic ($D^2 \propto t^2$), and Richardson's ($D^2 \propto t^3$) regimes. b) Relative diffusivity of sea ice calculated from MOSAiC buoys (red) and MODIS sea ice observations (blue). Green lines are estimated fits, while dashed lines represent the theoretical relative diffusivity regimes: nonlocal relative diffusivity ($Y \propto D^2$), and local relative diffusivity ($Y \propto D^{4/3}$) regimes.

growth is indicative of nonlocal relative dispersion as sub-mesoscale mechanisms drive the drifter's motion. The estimate fit is $D^2 = 1.2e^{1.86t}$ with an e-folding time equal to 0.54 days.

Next, a ballistic regime from 3.5 to 15 days is seen, distinguished by a quadratic growth in the relative dispersion curve. For this regime, the estimated fit is $D^2 = 22.0t^{2.10}$. At these scales, the drifters are mainly advected by the local shear of the EGC. Next, the Richardson's regime is recovered from 16 days to the end of the time series. The dispersion growth regime is expected to develop as $D^2 \propto t^3$ (estimated fit $D^2 = 1.1t^{2.93}$). This regime is associated with mesoscale eddies.

Interestingly, the Richardson regime is also captured by the MODIS sea ice motion. Because the spatiotemporal resolution of the images is much lower than MOSAiC buoys data, the sea ice pairs have a minimum initial separation of 20 km. Therefore, only the Richardson regime is recovered and the first few days of the MODIS relative dispersion curve can be neglected since it is not expected to capture a nonlocal or ballistic regime. From day 11 onward, the relative separation of the MODIS sea ice grew as t^3, with an estimated fit of $D^2 = 0.5t^{2.88}$.

5.4.3 Relative diffusivity

The relative diffusivities of the MOSAiC buoys and MODIS sea ice pairs were calculated. The mixing scales of the flow field were explored by plotting the results obtained from Equation 5.5 against pair separation (Figure 5.4.B). The pair separations were determined by averaging the relative diffusivities of buoys at specific separation bins discretized as $\text{bin}_n = \alpha^n D_0$, where α=1.1 and D_0 is the initial distance separation of buoys [46]. A nonlocal to local dispersion regime transition was observed at approximately 10 km. This first regime is consistent with nonlocal diffusivity, as the function is expected to grow quadratically at scales smaller than R_0. The estimated fit for the MOSAiC buoys is $4.3D^{2.09}$. The second regime was observed right after, at scales similar to R_0. This regime is an indication of local dispersion, where the separation rates are driven by mechanisms with similar length scales as their separation distance. The estimated fit is $38.8D^{1.19}$.

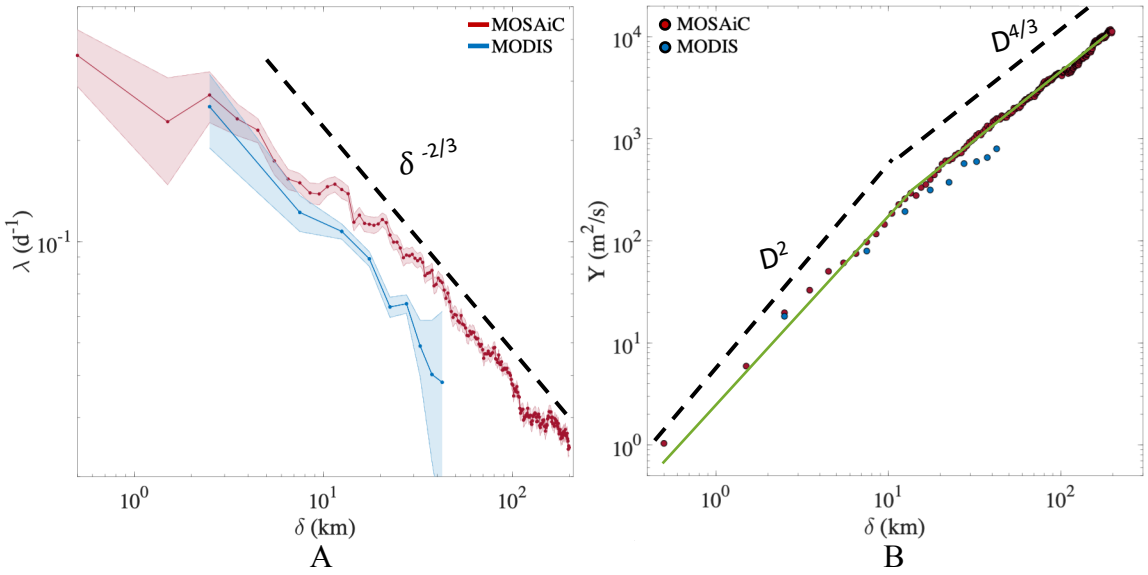

Figure 5.5: Finite-scale Lyapunov exponents. a) FSLE calculated for MOSAiC sea ice buoys (red) and MODIS sea ice observations (blue). The shaded region indicates the 95% confidence limits. Black line indicates the theoretical prediction for Richardson ($\lambda \propto D^{-2/3}$) regime. b) Relative diffusivity derived from FSLE for the MOSAiC buoy network (red) and MODIS sea ice (blue). Green lines are estimated fits, while dashed lines represent the theoretical relative diffusivity regimes: nonlocal relative diffusivity ($Y \propto D^2$), and local relative diffusivity ($Y \propto D^{4/3}$) regimes.

5.4.4 Finite-scale Lyapunov exponents

To calculate the FSLE, every possible initial separation, δ, of the drifter pairs was calculated and every instance the pairs separate a distance, $\rho\delta$, was recorded, where $\rho = \sqrt{(2)}$. The FSLE calculation begins by finding every instance a pair of buoys is separated within a distance, δ =0 to 1 km. Next, the time it takes these buoys to separates to a distance $\rho\delta$ is recorded.

This step is repeated, and so all the buoys separated within a distance, δ =1 to 2 km are found. The time it takes these buoy pairs to separate by a distance $\rho\delta$ is calculated. This is

repeated so forth. The FSLE calculation is halted when the number of pairs in a distance group is reduced to 25 % of the number found in the first group. In this study, the calculation is stopped at the 200th iteration, i.e., δ =199 km to 200 km.

The resulting FSLE vs δ calculation of MOSAiC buoys is presented in Figure 5.5.A. A clear Richardson regime can be identified from 10^1 to 10^2 km. From 0 to 10 km, however, a local dispersion is not resolved. It can be inferred that, at these scales, submesoscale processes smaller than 10 km significantly enhance the dispersion rate of drifters. These findings are in agreement with the local dispersion observed in Figure 5.4, where nonlocal dispersion is observed at short time- and length-scales. Despite the reduced resolution of MODIS data, the Richardson regime is also captured from an FSLE calculation on MODIS sea ice pairs.

Finally, the diffusivity of sea ice was calculated and is presented in Figure 5.5.B. The diffusivity derived via an FSLE calculation is consistent with the results presented in 5.4.B. Nonlocal diffusivity was confirmed by the diffusivity growth scaled as D^2 from 0 to about 10 km (estimated fit was calculated as $2.5D^{1.83}$). Next, the Richardson regime was once again observed after distances between 13 to 160 km, confirming local diffusivity at larger scales (estimated fit $9.14.3D^{1.34}$).

5.5 Conclusions

In this study, the structure of the underlying flow field was analyzed in the Arctic MIZ via one- and two-particle dispersion statistics of drifters. Information on the surface circulation is obtained from two different sources, MOSAiC Lagrangian drifters, and MODIS-detected sea ice. The main contribution of this study is the analysis of high-resolution data collected by the MOSAiC mission. From this data, the time and length scales of the smallest processes in the flow field were resolved. These submesoscale structures are known to strongly influence the dynamics of the region. However, the number of extensive high-resolution long-term *in-situ* observations remains unavailable to fully characterize the dynamics of other MIZ in polar oceans. With this problem in mind, Lagrangian trajectories of sea ice derived from

Table 5.1: Dispersion regimes detected using MOSAiC buoys.

	Absolute dispersion regimes			
	Ballistic	Anomalous		Diffusive
	$\mathbf{t^2}$	$\mathbf{t^{5/4}}$	$\mathbf{t^{5/3}}$	**t**
time scales [days]	0-1.5	1.5-23	ND	24-end
spatial scales [km]	0.5-15	15-90	ND	75-end

	Relative dispersion regimes			
	nonlocal	Ballistic	Richardson's	Diffusive
	$\mathbf{e^t}$	$\mathbf{t^2}$	$\mathbf{t^3}$	**t**
time scales [days]	0-2	3.5-15	16-end	ND
spatial scales [km]	0.8-6	13-60	60-end	ND

* ND: not detected

MODIS remote sensing data were obtained. As such, information of the flow field in regions where *in-situ* measurements are difficult to recover can still be recovered from remote sensing imagery. The comparison between the MOSAiC and the MODIS datasets confirmed the feasibility to retrieve the structure of the flow field from remote sensing imagery. Moreover, it was confirmed that ice motion at the mesoscale range is properly resolved by MODIS imagery and can be observed to transition between submeso- and meso-scale ranges.

The results of this investigation are summarized next. The absolute and relative dispersion at the ocean's surface for the two datasets were quantified. Despite their differences, the results are consistent between datasets and throughout the study. Inconsistency and failure to resolve intermediate regimes were expected when analyzing the absolute and relative dispersion of the MODIS drifters. However, the intermediate regimes were successfully identified by both the high-resolution MOSAiC buoys and the moderate-resolution MODIS sea ice measurements. This opens the door to achieving a more comprehensive characterization of the dynamical processes within MIZ over time by leveraging remote sensing data.

First, single-particle statistics of MOSAiC instruments and MODIS-derived sea ice were investigated. The influence of the mean flow was removed by employing the NSIDC sea ice product to calculate the displacements caused by velocity fluctuations of the drifters. At short time scales, the absolute dispersion of MOSAiC buoys obeyed a nearly ballistic regime. Because the MODIS measurements have a coarser temporal resolution, this regime was not expected to get resolved. However, at longer timescales, the absolute dispersion of both MOSAiC and MODIS drifters grew clearly in an anomalous regime, as the drifters are

strongly influenced by mesoscale processes in the region. Lastly, the absolute dispersion of the MOSAiC buoys showed a change of dispersion regimes after 24 days, likely entering the diffusive regime. There is a difference in magnitudes when comparing the absolute dispersion functions of MOSAiC and MODIS drifters. This can be attributed, in part, to the coarser temporal resolution of the measurements, as the entirety of the displacements from each MODIS drifter is not accounted for. Similarly, Gabrielski et al., 2015 [26] compared the dispersion of two drifter sets with different temporal resolutions, i.e., 1-hr and 12-hr respectively, which also showed a discrepancy in magnitudes similar to what is observed in this study. This single-particle statistics analysis on both drifter datasets emphasizes the findings from other studies that have highlighted the importance of meso/submeso-scale eddies on sea ice transport [47, 76].

These results are also qualitatively consistent with previous studies in the region. For example, buoy field campaigns such as Lukovich et al., 2011 [67] followed the trajectories of 22 ice beacons in the Beaufort Gyre during the winter of 2007 and 2008. Anomalous dispersion was evident in the meridional dispersion of the beacons from 6 days onward. A similar study in the Fram Strait MIZ registered absolute dispersion growing quadratically in time for the first 3 days and an anomalous dispersion from 6 days to 32 days [26]. Both findings agree with the scales resolved in this investigation. However, the studies employed only Lagrangian *in-situ* instruments and a dispersion field analysis in these regions has not been calculated from remote sensing observations to date.

Next, the relative dispersion of drifter pairs was explored via a two-particle dispersion statistical analysis and an FSLE calculation. First, the separation distances of MOSAiC instruments were quantified and observed to grow exponentially from the beginning up to approximately 2 days. This nonlocal dispersion regime corresponds to the nonlocal relative diffusivity regime observed up to 10 km. The e-folding time of 0.5 days agrees with e-folding times found in Nordic Seas during 2007–2008 [46] and the North Sea in 2018 [83]. On the other hand, studies performed in other regions of the world found an e-folding time of 12 days in the central North Atlantic [94], 1.25 days in the Bay of Bengal [122], and 0.5 to 1 day in the Southwestern Gulf of Mexico [152]. The faster e-folding time in this study region indicates faster separation rates of drifter pairs at short-length scales. Therefore, the results demonstrate that the influence of submesoscale coherent structures on the surface dispersion of sea ice at short time- and length- scales drives the dynamics in the region.

Two local relative dispersion regimes were also observed in the MOSAiC buoys, namely the ballistic and Richardson regime. Relative dispersion obeyed a ballistic regime from 3.5 to 15 days, followed by the Richardson regime from day 16 to the end of the time series. Despite the coarser resolution of MODIS measurements, the Richardson regime can also be identified in its relative dispersion function after approximately 11 days. The mixing characteristic length scales of the region agree in both datasets, as local diffusivity is observed after approximately 10 km. This result is per the Rossby radius of deformation in the region, R_0 = 5 km, and the eddy length scales in the region, 20-40 km with a lifetime of 2-3 weeks [38, 142]. Larger eddies have also been observed, 80-90 km [48]. Lastly, a

diffusive regime is not captured by either dataset. Throughout this region of interest, the EGC might impede the drifters to become uncorrelated and separate linearly (random walk).

Finally, the results obtained from quantifying the FSLE for both datasets were consistent with the findings obtained from the relative dispersion analysis. After approximately 10 km, the Richardson regime ($\lambda \propto t^{2/3}$) for both datasets can be discerned in the calculations. When examining the relative diffusivity, this time derived from FSLE, a transition from nonlocal to local diffusivity is observed around 10 km. These results agree with other studies performed around the world, where submesoscale motion shows nonlocal dispersion [15, 46]. Lumpkin et al., 2010 [70], however, warns that a higher than 1-hr resolution sampling is needed to resolve submesoscale motion. Meyerjügens et al., 2020 [83] observed a local dispersion in the form of a Richardson regime at submesoscales. The team attributed this to the possibility of inertial motions and strong tidal oscillations contaminating the submesoscales motion, as well as position uncertainties and sampling frequency of the drifters. Because the influence of inertial oscillations is strong in this region, the influence of inertial oscillations at small scales was alleviated by averaging the MOSAiC buoy motion over one inertial period, as explained in Section 5.3.

The lack of comprehensive drift measurements has thwarted a full characterization of surface dispersion in MIZ. The constant deployment of Lagrangian surveying instruments in the vast oceans presents a plethora of limitations, not to mention the additional challenges of pair buoy deployments under the harsh conditions of polar oceans. In this study, it was demonstrated that extensive and readily available moderate-resolution satellite imagery can

be employed to detect the transition regimes between nonlocal and local relative dispersion of the sea ice field in MIZ. Mesoscale turbulence was seen to dominate the absolute dispersion of sea ice at moderate scales. These findings open the door to achieving a more comprehensive characterization of the ocean surface dispersion dynamics in Arctic regions where Lagrangian measurements are difficult to obtain. To the author's knowledge, absolute and relative dispersion have not been quantified from remote sensing satellite imagery. Moreover, no other study has been conducted in the Fram Strait region to analyze the relative dispersion of sea ice due to the limited amount of buoys simultaneously surveying the region. Understanding the dispersion mechanisms driving the sea ice field can improve the modeling, forecasting, and understanding of the sea ice field in a rapidly changing Arctic system.

Chapter 6

Conclusions

The work presented in this dissertation is a comprehensive study of sea ice drift during the spring and summer seasons in Arctic MIZ over the twenty-first century. With the ultimate goal of advancing the understanding of the sea ice dynamics, this thesis combined the triad of remote sensing observational data analysis, high-resolution *in-situ* Lagrangian instruments, and numerical simulations.

Conventional sea ice characterization tools are intended to effectively retrieve large-scale sea ice motion in the consolidated ice pack. As such, ice tracking algorithms fail to produce accurate results given the high vorticity and deformation rates characteristic of sea ice in MIZ. The need for a characterization scheme capable of identifying the complex sea ice motion in MIZ inspired the development of a sea ice tracking algorithm in Chapter 2 . Extensive optical remote sensing imagery, namely Moderate-resolution Imaging Spectroradiometer (MODIS), was employed for this purpose. The developed algorithm filters atmospheric

conditions affecting MODIS images while maximizing sea ice identification. The algorithm is composed of three main stages: image processing, feature matching, and sea ice tracking. The robustness of the method was tested along the eastern coast of Greenland. Calculated mean ice floe velocities were found to be in good agreement with estimates derived from buoy and GPS measurements as well as SAR drift products. Further testing in Arctic regions with different dynamical properties also proved successful (e.g., within Fram Strait and in the Beaufort Sea), proving the feasibility of the method to collect unprecedented data of sea ice dynamics in the Arctic MIZ.

Chapter 3, is an in-depth assessment of the role of atmospheric and oceanic forcing on ice floe motion. First, a strong relation of the sea ice and ocean dynamic field is established via the idealized quasi-geostrophic model. The rotating rate measurements of over 28,000 ice floes were calculated in the Beaufort Gyre MIZ. The dynamics of the ice were demonstrated to be in quasi-equilibrium with the underlying oceanic eddy field dynamics in MIZ. As such, the sea ice drift field served as an indicator to gauge the evolution of MIZ dynamics in a rapidly changing Arctic. After establishing this relation, the instances when sea ice trajectories deviated from a straight path were further investigated. These trajectories were weakly correlated with the wind field. This suggested that, despite the strong winds in the area, upper ocean currents play an important role in sea ice transport. During some of these events, the intrinsically strong sea ice-ocean interactions drove sea ice to mirror meso/submesoscale ocean eddies, forming loops. An automatic eddy detection algorithm from MODIS imagery was developed. For the first time, the approach retrieved the geographical location, length

scale, and direction of identified eddies leveraging satellite-derived sea ice information. Predominantly, this analysis is affected by missing sections in the Lagrangian trajectories of sea ice. Linear interpolation is used to recover missing information. However, the present work will benefit from the implementation of a better-suited smoother. Preliminary analyses have proven successful when an ensemble Kalman smoother (EnKS) is implemented to recover realistic sea ice dynamics in MIZ. However, the state of the ocean and atmosphere have to be known *a priori*. By improving the quality of the recovered sea ice trajectories, the quality of the eddy-detection tool presented in Chapter 3 can therefore be improved in future work.

In Chapter 4 , the Lagrangian trajectories along the Fram Strait and Greenland Sea MIZ were statistically analyzed to study the topology of the underlying flow field. From 2003 to 2020, over 10,000 ice floe trajectories were employed to quantify the single-particle dispersion of sea ice. In this region, sea ice absolute dispersion grew in an anomalous regime, driven by the dominant influence of energetic turbulent fluctuations. The results highlight the importance of meso/submesoscale eddies in sea ice transport. The longevity of the MODIS data unveiled the sea ice interannual and seasonal variability over the twenty-first century. A strong correlation was found between sea ice velocities and the sea ice extent conditions in the region. The magnitude of sea ice velocity in the central Arctic basin has increased with receding sea ice concentrations. In MIZ, however, a decrease in sea ice speeds with decreasing sea ice concentrations suggests that sea ice wind stresses have a stronger effect on consolidated ice in the central basin in comparison to the thinner MIZ sea

ice. As such, comprehensive observations of the MIZ sea ice thus revealed that the critical physical processes driving sea ice motion in MIZ are different than in the central Arctic Basin. Furthermore, we find an anti-correlation between sea ice extent and sea ice fluctuating velocities. As sea ice extent continues decreasing in the Arctic, the ocean turbulent field is thus expected to intensify.

In Chapter 5 the single-particle and two-particle dispersion of two different types of surface tracers were quantified along the Fram Strait and Greenland sea MIZ. The unique opportunity to employ unprecedented MOSAiC drifter data in concert with MODIS images validated the results presented in Chapter 4. Moreover, this study showed the feasibility to explore the transition processes linking meso/submesoscale ocean circulation in Arctic MIZ employing moderate resolution remote sensing imagery. For the first time, Lagrangian trajectories of sea ice derived from satellite imagery are used to quantify dispersion statistics of the sea ice field. Both datasets provide important information to understand the ocean surface circulation in regions where direct ocean measurements are challenging to obtain. As such, this comprehensive study provided a new tool to study the topology of the underlying turbulent field. Future investigations would benefit from employing higher-resolution imagery to capture the smallest dispersion and energy regimes of the sea ice system.

The MODIS-based sea ice tracking algorithm provides novel observations of the sea ice drift field in MIZ. The presented tool motivates further investigations. A notable future investigation is the development and validation of a simplified sea ice–ocean–atmosphere system model. Correct prediction of the mechanical evolution of MIZ can be achieved by

coupling sea ice observations with high-resolution oceanic and atmospheric measurements. This information can be employed to quantify the momentum transfer between the atmosphere, ocean, and ice. This endeavor will support current efforts of the scientific community to better forecast sea ice conditions. Atmosphere-ocean forcing of *in-situ* measurements are not always available. Nevertheless, the reanalysis product ERA5 10-m wind speeds is suggested to calculate the wind flow field. Surface Water and Ocean Topography (SWOT) data is recommended to infer the ocean flow field. The SWOT mission is scheduled to launch later this year. It will provide sea surface height (SSH) with an unprecedented resolution of 15–30 km wavelength. With global coverage and a repeat period of 21 days, SSH measurements along Arctic MIZ will be collected. The satellite tracks will cover a large area of the Arctic, given its 120 km-wide swaths. The small temporal scales of this data will help determine the presence of eddies in the field and validate the regions identified by meanders and loops in sea ice trajectories to improve the eddy detection algorithm presented in this work.

This dissertation concludes by emphasizing the crucial role of sea ice in polar oceans. As the Arctic climate system transforms at unprecedented rates, it is important to integrate novel and extensive measurements into the study of the sea ice field. Given the plethora of potential applications, this work presents possible collaborations with experts across physical oceanography and mechanical engineering disciplines that will help achieve adequate characterization of sea ice to advance our understanding of MIZ in a *new* Arctic.

Bibliography

[1] K. Aagaard and E. C. Carmack. The role of sea ice and other fresh water in the Arctic circulation. *Journal of Geophysical Research: Oceans*, 94(C10):14485–14498, 1989.

[2] S. Ackerman, K. Strabala, P. Menzel, R. Frey, C. Moeller, L. Gumley, B. Baum, S. W. Seeman, and H. Zhang. Discriminating clear-sky from cloud with MODIS. Algorithm theoretical basis document (MOD35). In ATBD Ref. ATBD-MOD-06, Version 4.0. Madison, WI: University of Wisconsin-Madison., 2002.

[3] B. K. Arbic, R. B. Scott, G. R. Flierl, A. J. Morten, J. G. Richman, and J. F. Shriver. Nonlinear Cascades of Surface Oceanic Geostrophic Kinetic Energy in the Frequency Domain. *Journal of Physical Oceanography*, 42(9):1577–1600, 2012.

[4] T. W. K. Armitage, S. Bacon, A. L. Ridout, S. F. Thomas, Y. Aksenov, and D. J. Wingham. Arctic sea surface height variability and change from satellite radar altimetry and GRACE, 2003–2014. *Journal of Geophysical Research: Oceans*, 121(6):4303–4322, 2016.

[5] V. Artale, G. Boffetta, A. Celani, M. Cencini, and A. Vulpiani. Dispersion of passive tracers in closed basins: Beyond the diffusion coefficient. *Physics of Fluids*, 9(11):3162–3171, 1997.

[6] G. K. Batchelor. *The theory of homogeneous turbulence*. Cambridge Monographs on Mechanics and Applied Mathematics. Cambridge University Press, 1953.

[7] O. Boebel, J. Lutjeharms, C. Schmid, W. Zenk, T. Rossby, and C. Barron. The Cape Cauldron: a regime of turbulent inter-ocean exchange. *Deep Sea Research Part II: Topical Studies in Oceanography*, 50(1):57–86, 2003.

[8] A. Bracco, J. H. LaCasce, and A. Provenzale. Velocity Probability Density Functions for Oceanic Floats. *Journal of Physical Oceanography*, 30(3):461 – 474, 2000.

[9] A. Bracco, J. von Hardenberg, A. Provenzale, J. B. Weiss, and J. C. McWilliams. Dispersion and mixing in quasigeostrophic turbulence. *Physical Review Letters*, 92:084501, 2004.

[10] J. G. Charney. Geostrophic Turbulence. *Journal of Atmospheric Sciences*, 28(6):1087–1095, 1971.

[11] D. A. Clausi and B. Yue. Comparing cooccurrence probabilities and Markov random fields for texture analysis of SAR sea ice imagery. *IEEE Transactions on Geoscience and Remote Sensing*, 42(1):215–228, 2004.

[12] S. T. Cole, M.-L. Timmermans, J. M. Toole, R. A. Krishfield, and F. T. Thwaites. Ekman Veering, Internal Waves, and Turbulence Observed under Arctic Sea Ice. *Journal of Physical Oceanography*, 44(5):1306 – 1328, 2014.

[13] R. Colony and A. S. Thorndike. An estimate of the mean field of Arctic sea ice motion. *Journal of Geophysical Research: Oceans*, 89(C6):10,623–10,629, 1984.

[14] R. Colony and A. S. Thorndike. Sea Ice Motion as a Drunkard's Walk. *Journal of Geophysical Research: Oceans*, 90(C1):965–974, 1985.

[15] R. Corrado, G. Lacorata, L. Palatella, R. Santoleri, and E. Zambianchi. General characteristics of relative dispersion in the ocean. *Scientific Reports*, 7(46291), 2017.

[16] R. E. Davis. Observing the general circulation with floats. *Deep Sea Research Part A. Oceanographic Research Papers*, 38:S531–S571, 1991.

[17] D. Demchev, V. Volkov, E. Kazakov, P. F. Alcantarilla, S. Sandven, and V. Khmeleva. Sea ice drift tracking from sequential SAR images using Accelerated-KAZE features. *IEEE Transactions on Geoscience and Remote Sensing*, 55(9):5174–5184, 2017.

[18] C. Dong, Y. Liu, R. Lumpkin, M. Lankhorst, D. Chen, J. C. McWilliams, and Y. Guan. A Scheme to Identify Loops from Trajectories of Oceanic Surface Drifters: An Application in the Kuroshio Extension Region. *Journal of Atmospheric and Oceanic Technology*, 28(9):1167 – 1176, 2011.

[19] G. Dybkjaer. *Medium Resolution Sea Ice Drift Product User Manual,* version 2.0. EUMETSAT OSISAF Ocean and Sea Ice, 2018.

[20] S. Eastwood, J. Karvonen, F. Dinessen, A. Fleming, L. Toudal Pedersen, R. Saldo, J. Buus-Hinkler, B. Hackett, F. Ardhuin, M. Brandt Kreiner, J. Seppänen, and C. Wettre. *Quality information document for SI TAC Sea Ice products 011-001, -002, -004, -006, -007, -009, -010, -011, -012, -013, -014,* issue: 2.10. Copernicus Marine Environment Monitoring Services, 2020.

[21] D. Elhmaïdi, A. Provenzale, and A. Babiano. Elementary topology of two-dimensional turbulence from a Lagrangian viewpoint and single-particle dispersion. *Journal of Fluid Mechanics*, 257:533–558, 1993.

[22] F. Fetterer, K. Knowles, W.M. Meier, M. Savoie, and A. K. Windnagel. Sea Ice Index, Version 3. [Northern Hemisphere]. Boulder, Colorado USA. NSIDC: National Snow and Ice Data Center, 2017.

[23] F. Fetterer, J. S. Stewart, and W. N. Meier. MASAM2: Daily 4 km Arctic Sea Ice Concentration, Version 1. Boulder, Colorado USA. NSIDC: National Snow and Ice Data Center. doi: 10.7265/N5ZS2TFT. [03-2021], 2015.

[24] M. Fily and D. A. Rothrock. Sea Ice Tracking by Nested Correlations. *IEEE Transactions on Geoscience and Remote Sensing*, GE-25(5):570–580, 1987.

[25] J. D. Ford and B. Smit. A Framework for Assessing the Vulnerability of Communities in the Canadian Arctic to Risks Associated with Climate Change. *Arctic*, 57(4):389–400, 2004.

[26] A. Gabrielski, G. Badin, and L. Kaleschke. Anomalous dispersion of sea ice in the Fram Strait region. *Journal of Geophysical Research: Oceans*, 120(3):1809–1824, 2015.

[27] F. Girard-Ardhuin and R. Ezraty. Enhanced Arctic Sea Ice Drift Estimation Merging Radiometer and Scatterometer Data. *IEEE Transactions on Geoscience and Remote Sensing*, 50(7):2639–2648, 2012.

[28] C. A. Greene, D. E. Gwyther, and D. D. Blankenship. Antarctic Mapping Tools for Matlab. *Computers & Geosciences*, 104:151–157, 2017.

[29] M.-V. Guarino, L. C. Sime, D. Schröeder, I. Malmierca-Vallet, E. Rosenblum, M. Ringer, J. Ridley, D. Feltham, C. Bitz, E. J. Steig, E. Wolff, J. Stroeve, and A. Sellar. Sea-ice-free Arctic during the Last Interglacial supports fast future loss. *Nature Climate Change*, 10:928–932, 2020.

[30] J. Haarpaintner. Arctic-Wide Operational Sea Ice Drift from Enhanced-Resolution QuikScat/SeaWinds Scatterometry and Its Validation. *IEEE Transactions on Geoscience and Remote Sensing*, 44(1):102–107, 2006.

[31] W. D. Hibler. A dynamic thermodynamic sea ice model. *Journal of Physical Oceanography*, 9(4):815 – 846, 1979.

[32] W. D. Hibler III and S. F. Ackley. Numerical simulation of the Weddell Sea pack ice. *Journal of Geophysical Research: Oceans*, 88(C5):2873–2887, 1983.

[33] Z. Hofmann, W.-J. von Appen, and C. Wekerle. Seasonal and Mesoscale Variability of the Two Atlantic Water Recirculation Pathways in Fram Strait. *Journal of Geophysical Research: Oceans*, 126(7):e2020JC017057, 2021.

[34] B. Holt, D. A. Rothrock, and R. Kwok. *Determination of sea ice motion from satellite images*. In Microwave Remote Sensing of Sea Ice, Carsey, F.D. (Ed.). Washington, DC: American Geophysical Union. https://doi.org/doi:10.1029/GM068p0343 .

[35] C. Horvat, E. Tziperman, and J.-M. Campin. Interaction of sea ice floe size, ocean eddies, and sea ice melting. *Geophysical Research Letters*, 43(15):8083–8090, 2016.

[36] B. Hwang, J. Ren, S. McCormack, C. Berry, I. Ben Ayed, H. C. Graber, and E. Aptoula. A practical algorithm for the retrieval of floe size distribution of Arctic sea ice from high-resolution satellite Synthetic Aperture Radar imagery. *Elementa: Science of the Anthropocene*, 5:38, 2017.

[37] J. K. Hutchings J. V. Lukovich and and D. G. Barber. On sea-ice dynamical regimes in the arctic ocean. *Annals of Glaciology*, 56(69):323–331, 2015.

[38] O. M. Johannessen, J. A. Johannessen, E. Svendsen, R. A. Shuchman, W. J. Campbell, and E. Josberger. Ice-Edge Eddies in the Fram Strait Marginal Ice Zone. *Science*, 236(4800):427–429, 1987.

[39] S. Jónsson, A. Foldvik, and K. Aagaard. The structure and atmospheric forcing of the mesoscale velocity field in Fram Strait. *Journal of Geophysical Research: Oceans*, 97(C8):12585–12600, 1992.

[40] J. Karvonen. Operational SAR-based sea ice drift monitoring over the Baltic Sea. *Ocean Science*, 8(4):473–483, 2012.

[41] K.-Y. Kim, J.-Y. Kim, J. Kim, S. Yeo, H. Na, B. D. Hamlington, and R. R. Leben. Vertical Feedback Mechanism of Winter Arctic Amplification and Sea Ice Loss. *Scientific Reports*, 9(1):1184, 2019.

[42] P. Klein and G. Lapeyre. The Oceanic Vertical Pump Induced by Mesoscale and Submesoscale Turbulence. *Annual Review of Marine Science*, 1(1):351–375, 2009.

[43] A. N. Kolmogorov. The Local Structure of Turbulence in Incompressible Viscous Fluid for Very Large Reynolds' Numbers. *Akademiia Nauk SSSR Doklady*, 30:301–305, 1941.

[44] A. S. Komarov and D. G. Barber. Sea Ice Motion Tracking From Sequential Dual-Polarization RADARSAT-2 Images. *IEEE Transactions on Geoscience and Remote Sensing*, 52(1):121–136, 2014.

[45] A. A. Korosov and P. Rampal. A Combination of Feature Tracking and Pattern Matching with Optimal Parametrization for Sea Ice Drift Retrieval from SAR Data. *Remote Sensing*, 9(3):25, 2017.

[46] I. Koszalka, J. H. LaCasce, and K. A. Orvik. Relative dispersion in the Nordic Seas. *Journal of Marine Research*, 67(4):411–433, 2009.

[47] I. E. Kozlov, A. V. Artamonova, G. E. Manucharyan, and A. A. Kubryakov. Eddies in the Western Arctic Ocean From Spaceborne SAR Observations Over Open Ocean and Marginal Ice Zones. 124(9):6601–6616, 2019.

[48] I. E. Kozlov, E. V. Plotnikov, and G. E. Manucharyan. Brief Communication: Mesoscale and submesoscale dynamics in the marginal ice zone from sequential synthetic aperture radar observations. *The Cryosphere*, 14(9):2941–2947, 2020.

[49] R. H. Kraichnan. Inertial ranges in two-dimensional turbulence. *The Physics of Fluids*, 10(7):1417–1423, 1967.

[50] R. Kwok. RADARSAT-1 data (CSA). Dataset: Lagrangian Sea-Ice Kinematics. Retrieved from ASF DAAC 7 December 2014. doi: 10.5067/SSMPINYI15UU.

[51] R. Kwok. Satellite remote sensing of sea-ice thickness and kinematics: a review. *Journal of Glaciology*, 56(200):1129–1140, 2010.

[52] R. Kwok, G. F. Cunningham, and S. S. Pang. Fram strait sea ice outflow. *Journal of Geophysical Research: Oceans*, 109(C1), 2004.

[53] R. Kwok, J. C. Curlander, R. Mcconnell, and S. S. Pang. An ice-motion tracking system at the Alaska SAR Facility. *IEEE Journal of Oceanic Engineering*, 15(1):44–54, 1990.

[54] R. Kwok and J. Morison. Dynamic topography of the ice-covered Arctic Ocean from ICESat. *Geophysical Research Letters*, 38(2), 2011.

[55] R. Kwok, A. Schweiger, D. A. Rothrock, S. Pang, and C. Kottmeier. Sea ice motion from satellite passive microwave imagery assessed with ERS SAR and buoy motions. *Journal of Geophysical Research Oceans*, 103(C4):8191–8214, 1998.

[56] J. H. LaCasce. Statistics from Lagrangian observations. *Progress in Oceanography*, 77(1):1–29, 2008.

[57] J. H. LaCasce, R. Ferrari, J. Marshall, R. Tulloch, D. Balwada, and K. Speer. Float-derived isopycnal diffusivities in the DIMES Experiment. *Journal of Physical Oceanography*, 44(2):764–780, 2014.

[58] G. Lacorata, E. Aurell, and A. Vulpiani. Drifter dispersion in the Adriatic Sea: Lagrangian data and chaotic model. *Annales Geophysicae*, 19(1):121–129, 2001.

[59] T. Lavergne, S. Eastwood, Z. Teffah, H. Schyberg, and L. A. Breivik. Sea ice motion from low-resolution satellite sensors: An alternative method and its validation in the Arctic. *Journal of Geophysical Research: Oceans*, 115:032, 2010.

[60] J.-S. Lee. Speckle analysis and smoothing of synthetic aperture radar images. *Computer Graphics and Image Processing*, 17(1):24–32., 1981.

[61] M. Leppäranta. *The Drift of Sea Ice*. Geophysical Sciences. Springer, 2011.

[62] J.-T. Lin. Relative Dispersion in the Enstrophy-Cascading Inertial Range of Homogeneous Two-Dimensional Turbulence. *Journal of Atmospheric Sciences*, 29(2):394 – 396, 1972.

[63] R. W. Lindsay and H. L. Stern. The RADARSAT Geophysical Processor System: Quality of Sea Ice Trajectory and Deformation Estimates. *Journal of Atmospheric and Oceanic Technology*, 20(9):1333 – 1347, 2003.

[64] A. K. Liu, Y. Zhao, and S. Y. Wu. Arctic sea ice drift from wavelet analysis of NSCAT and special sensor microwave imager data. *Journal of Geophysical Research Oceans*, 104(C5):11529–11538, 1999.

[65] R. Lopez-Acosta, M. P. Schodlok, and M. M. Wilhelmus. Ice Floe Tracker: An algorithm to automatically retrieve Lagrangian trajectories via feature matching from moderate-resolution visual imagery. *Remote Sensing of Environment*, 234:111406, 2019.

[66] Jesús Lucio. Bezier curve (https://www.mathworks.com/matlabcentral/fileexchange/32817-bezier-curve), MATLAB Central File Exchange. Retrieved August 9, 2021. 2021.

[67] J. V. Lukovich, D. G Babb, and D. G. Barber. On the scaling laws derived from ice beacon trajectories in the southern Beaufort Sea during the International Polar Year - Circumpolar Flaw Lead study, 2007-2008. *Journal of Geophysical Research: Oceans*, 116(C9), 2011.

[68] J. V. Lukovich, C. Bélanger, D. G. Barber, and Y. Gratton. On coherent ice drift features in the southern Beaufort sea. *Deep Sea Research Part I: Oceanographic Research Papers*, 92:56–74, 2014.

[69] J. V. Lukovich, C. A. Geiger, and D. G. Barber. Method to characterize directional changes in Arctic sea ice drift and associated deformation due to synoptic atmospheric variations using Lagrangian dispersion statistics. *The Cryosphere*, 11(4):1707–1731, 2017.

[70] R. Lumpkin and S. Elipot. Surface drifter pair spreading in the North Atlantic. *Journal of Geophysical Research: Oceans*, 115(C12), 2010.

[71] B. Lund, H. C. Graber, P. O. G. Persson, M. Smith, M. Doble, J. Thomson, and P. Wadhams. Arctic sea ice drift measured by shipboard marine radar. *Journal of Geophysical Research: Oceans*, 123(6):4298–4321, 2018.

[72] S. Lundrigan and E. Demirov. Mean and Eddy-Driven Heat Advection in the Ocean Region Adjacent to the Greenland-Scotland Ridge Derived From Satellite Altimetry. *Journal of Geophysical Research: Oceans*, 124(3):2239–2260, 2019.

[73] Z. Lv, Y. Hu, H. Zhong, J. Wu, B. Li, and H. Zhao. Parallel K-Means Clustering of Remote Sensing Images Based on MapReduce. In 2010 Proceedings Int. Web Inf. Sys. Mining, Wang F.L., Gong Z., Luo X., and Lei J. (Ed.). Berlin, Germany: Springer-Verlag, 162–170. 2010.

[74] M. Lévy, R. Ferrari, P. J. S. Franks, A. P. Martin, and P. Rivière. Bringing physics to life at the submesoscale. *Geophysical Research Letters*, 39(14), 2012.

[75] G. E. Manucharyan, R. Lopez-Acosta, and M. M. Wilhelmus. Spinning ice floes reveal intensification of mesoscale eddies in the western Arctic Ocean. *Manuscript submitted for publication*, 2021.

[76] G. E. Manucharyan and A. F. Thompson. Submesoscale Sea Ice-Ocean Interactions in Marginal Ice Zones. *Journal of Geophysical Research: Oceans*, 122(12):9455–9475, 2017.

[77] J. A. Maslanik, C. Fowler, J. Stroeve, S. Drobot, J. Zwally, D. Yi, and W. Emery. A younger, thinner Arctic ice cover: Increased potential for rapid, extensive sea-ice loss. *Geophysical Research Letters*, 34(24), 2007.

[78] R. McConnell, R. Kwok, J. Curlander, W. Kober, and S. Pang. ψ-s correlation and dynamic time warping: two methods for tracking ice floes in SAR images. *IEEE Trans. Geosci. Remote. Sens.*, 29:1004–1012, 1991.

[79] D. J. McGillicuddy. Mechanisms of Physical-Biological-Biogeochemical Interaction at the Oceanic Mesoscale. *Annual Review of Marine Science*, 8(1):125–159, 2016.

[80] N. Melia, K. Haines, and E. Hawkins. Sea ice decline and 21st century trans-Arctic shipping routes. *Geophysical Research Letters*, 43:9720–9728. 10.1002/2016GL069315, 2016.

[81] G. Meneghello, J. Marshall, C. Lique, P. E. Isachsen, E. Doddridge, J.-M. Campin, H. Regan, and C. Talandier. Genesis and Decay of Mesoscale Baroclinic Eddies in the Seasonally Ice-Covered Interior Arctic Ocean. *Journal of Physical Oceanography*, 51(1):115 – 129, 2021.

[82] J. Meyerjürgens, T. H. Badewien, S. P. Garaba, J.-O. Wolff, and O. Zielinski. A State-of-the-Art Compact Surface Drifter Reveals Pathways of Floating Marine Litter in the German Bight. *Frontiers in Marine Science*, 6:58, 2019.

[83] J. Meyerjürgens, M. Ricker, V. Schakau, T. H. Badewien, and E. V. Stanev. Relative Dispersion of Surface Drifters in the North Sea: The Effect of Tides on Mesoscale Diffusivity. *Journal of Geophysical Research: Oceans*, 125(8):e2019JC015925, 2020.

[84] A. Mjaavatten. Curvature of a 1D curve in a 2D or 3D space (https://www.mathworks.com/matlabcentral/fileexchange/69452-curvature-of-a-1d-curve-in-a-2d-or-3d-space). MATLAB Central File Exchange. Retrieved August 9, 2021. 2021.

[85] W. Moon and J. S. Wettlaufer. On the nature of the sea ice albedo feedback in simple models. *Journal of Geophysical Research: Oceans*, 119(8):5555–5562, 2014.

[86] S. Muckenhuber, A. A. Korosov, and S. Sandven. Open-source feature-tracking algorithm for sea ice drift retrieval from sentinel-1 sar imagery. *The Cryosphere*, 10(2):913–925, 2016.

[87] S. Muckenhuber and S. Sandven. Open-source sea ice drift algorithm for Sentinel-1 SAR imagery using a combination of feature tracking and pattern matching. *The Cryosphere*, 11(4):1835–1850, 2017.

[88] S. Muckenhuber and S. Sandven. Sea ice drift data for Fram Strait derived from a feature-tracking algorithm applied on Sentinel-1 SAR imagery. *Data in Brief*, 18:1410–1415, 2018.

[89] L. A. Mysak and S. A. Venegas. Decadal climate oscillations in the Arctic: A new feedback loop for atmosphere-ice-ocean interactions. *Geophysical Research Letters*, 25(19):3607–3610, 1998.

[90] F. Nansen. *The Norwegian North polar expedition, 1893-1896 : Scientific Results*. London ; New York : Longmans, Green and Co. ; Christiania : J. Dybwad, 1900-1906, 1902.

[91] NOAA National Geophysical Data Center. 2009: ETOPO1 1 Arc-Minute Global Relief Model. NOAA National Centers for Environmental Information. Accessed 2019.

[92] A. J. G. Nurser and S. Bacon. The Rossby radius in the Arctic Ocean. *Ocean Science*, 10(6):967–975, 2014.

[93] E. Olason and D. Notz. Drivers of variability in Arctic sea-ice drift speed. *Journal of Geophysical Research: Oceans*, 119(9):5755–5775, 2014.

[94] M. Ollitrault, C. Gabillet, and A. C. De Verdière. Open ocean regimes of relative dispersion. *Journal of Fluid Mechanics*, 533:381–407, 2005.

[95] T. M. Pavelsky and L. C. Smith. Spatial and temporal patterns in Arctic river ice breakup observed with MODIS and AVHRR time series. *Remote Sensing of the Environment*, 93(3):328–338, 2004.

[96] G. Peng, J. L. Matthews, M. Wang, R. Vose, and L. Sun. What do global climate models tell us about future arctic sea ice coverage changes? *Climate*, 8(1), 2020.

[97] D. Perovich, W. Meier, M. Tschudi, S. Hendricks, A. A. Petty, D. Divine, S. Farrell, S. Gerland, C. Hass, L. Kaleschke, O. Pavlova, R. Ricker, X. Tian-Kunze, M. Webster, and K. Wood. *Arctic Report Card 2020*, chapter Sea Ice. 2020.

[98] D. K. Perovich, S. V. Nghiem, T. Markus, and A. Schweiger. Seasonal evolution and interannual variability of the local solar energy absorbed by the arctic sea ice–ocean system. *Journal of Geophysical Research: Oceans*, 112(C3), 2007.

[99] S. Pfirman, W. F. Haxby, R. Colony, and I. Rigor. Variability in Arctic sea ice drift. *Geophysical Research Letters*, 31:L16402, 2004.

[100] P.-M. Poulain, R. Gerin, E. Mauri, and R. Pennel. Wind Effects on Drogued and Undrogued Drifters in the Eastern Mediterranean. *Journal of Atmospheric and Oceanic Technology*, 26(6):1144, 2009.

[101] P.-M. Poulain, A. Warn-Varnas, and P. P. Niiler. Near-surface circulation of the Nordic seas as measured by Lagrangian drifters. *Journal of Geophysical Research*, 101:18237–18258, 1996.

[102] A. Proshutinsky, R. Krishfield, J. M. Toole, M.-L. Timmermans, W. Williams, S. Zimmermann, M. Yamamoto-Kawai, T. W. K. Armitage, D. Dukhovskoy, E. Golubeva, G. E. Manucharyan, G. Platov, E. Watanabe, T. Kikuchi, S. Nishino, M. Itoh, S.-H. Kang, K.-H. Cho, K. Tateyama, and J. Zhao. Analysis of the Beaufort Gyre Freshwater Content in 2003-2018. *Journal of Geophysical Research: Oceans*, 124(12):9658–9689, 2019.

[103] A. Provenzale. Transport by coherent barotropic vortices. *Annual Review of Fluid Mechanics*, 31(1):55–93, 1999.

[104] M. Raffel, C. E. Willert, F. Scarano, J. C. Kahler, S. T. Wereley, and J. Kompenhans. *Particle Image Velocimetry: A practical guide,* 3rd ed. Berlin, Germany: Springer International Publishing. https://doi.org/10.1007/978-3-319-68852-7 , 2018.

[105] P. Rampal, S. Bouillon, J. Bergh, and E. Ólason. Arctic sea-ice diffusion from observed and simulated Lagrangian trajectories. *The Cryosphere*, 10(4):1513–1527, 2016.

[106] P. Rampal, J. Weiss, and D. Marsan. Positive trend in the mean speed and deformation rate of Arctic sea ice, 1979-2007. *Journal of Geophysical Research: Oceans*, 114(C5), 2009.

[107] P. Rampal, J. Weiss, D. Marsan, and M. Bourgoin. Arctic sea ice velocity field: General circulation and turbulent-like fluctuations. *Journal of Geophysical Research: Oceans*, 114(C10), 2009.

[108] A. H. H. Renner, S. Gerland, C. Haas, G. Spreen, J. F. Beckers, E. Hansen, M. Nicolaus, and H. Goodwin. Evidence of Arctic sea ice thinning from direct observations. *Geophysical Research Letters*, 41(14):5029–5036, 2014.

[109] C. A. Ribic, D. G. Ainley, and W. R. Fraser. Habitat selection by marine mammals in the marginal ice zone. *Antarctic Science*, 3(2):181–186, 1991.

[110] L. F. Richardson. Atmospheric Diffusion Shown on a Distance-Neighbour Graph. *Proceedings of the Royal Society of London Series A*, 110(756):709–737, 1926.

[111] G. A. Riggs and D. K. Hall. *MODIS Sea Ice products User guide Collection 6,* 1st ed. MODIS and VIIRS Snow and ice Global Mapping Project, 2015.

[112] I. G. Rigor, R. L. Colony, and S. Martin. Variations in Surface Air Temperature Observations in the Arctic, 1979–97. *Journal of Climate*, 13(5):896 – 914, 2000.

[113] I. G. Rigor, J. M. Wallace, and R. L. Colony. Response of Sea Ice to the Arctic Oscillation. *Journal of Climate*, 15:2648–2663., 2002.

[114] B. Rudels, H. J. Friedrich, and D. Quadfasel. The Arctic Circumpolar Boundary Current. *Deep Sea Research Part II: Topical Studies in Oceanography*, 46(6):1023–1062, 1999.

[115] V. Rupolo, V. Artale, B. L. Hua, and A. Provenzale. Lagrangian Velocity Spectra at 700 m in the Western North Atlantic. *Journal of Physical Oceanography*, 26(8):1591 – 1607, 1996.

[116] David T. Sandwell. Biharmonic spline interpolation of geos-3 and seasat altimeter data. *Geophysical Research Letters*, 14(2):139–142, 1987.

[117] R. Slats, C. Oliver, R. Bahnke, H. Bell, A. Miller, D. Pungowiyi, J. Merculief, N. Menadelook Sr., J. Ivanoff, and C. Oxereok. Voices from the Front Lines of a Changing Bering Sea. An Indigenous Perspective for the 2019 Arctic Report Card. *Arctic Report Card 2019,* M. L. Druckenmiller, R. Daniel, and M. Johnson, Eds., 2019.

[118] L. H. Smedsrud, M. H. Halvorsen, J. C. Stroeve, R. Zhang, and K. Kloster. Fram Strait sea ice export variability over the last 80 years, 2016. Supplement to: Smedsrud, LH et al. (2017): Fram Strait sea ice export variability and September Arctic sea ice extent over the last 80 years. *The Cryosphere*, 11(1), 65-79.

[119] C. Solomon and T. Breckon. *Fundamentals of Digital Image Processing : A Practical Approach with Examples in Matlab,* 2nd ed. John Wiley & Sons, Incorporated, West Sussex, United Kingdom, 2011.

[120] T. H. Solomon, E. R. Weeks, and H. L. Swinney. Observation of anomalous diffusion and Lévy flights in a two-dimensional rotating flow. *Physical Review Letters*, 71:3975–3978, 1993.

[121] G. Spreen, L. de Steur, D. Divine, S. Gerland, E. Hansen, and R. Kwok. Arctic Sea Ice Volume Export Through Fram Strait From 1992 to 2014. *Journal of Geophysical Research: Oceans*, 125(6):e2019JC016039, 2020.

[122] M. S. Spydell, F. Feddersen, and J. Macmahan. Relative Dispersion on the Inner Shelf: Evidence of a Batchelor Regime. *Journal of Physical Oceanography*, 51(2):519 – 536, 2021.

[123] J. Stroeve, M. M. Holland, W. Meier, T. Scambos, and M. Serreze. Arctic sea ice decline: Faster than forecast. *Geophysical Research Letters*, 34(9), 2007.

[124] C. Strong and I. G. Rigor. Arctic marginal ice zone trending wider in summer and narrower in winter. *Geophysical Research Letters*, 40(18):4864–4868, 2013.

[125] H. Su, Y. Wang, and J. Yang. Monitoring the Spatiotemporal Evolution of Sea Ice in the Bohai Sea in the 2009–2010 Winter Combining MODIS and Meteorological Data. *Estuaries Coasts*, 35(1):281–291., 2012.

[126] S. Swart, M. D. du Plessis, A. F. Thompson, L. C. Biddle, I. Giddy, T. Linders, M. Mohrmann, and S.-A. Nicholson. Submesoscale Fronts in the Antarctic Marginal Ice Zone and Their Response to Wind Forcing. *Geophysical Research Letters*, 47(6):e2019GL086649, 2020.

[127] R. T. Tan. Visibility in bad weather. In 2008 IEEE Conf. Computer Vision Pattern Recognition, Anchorage, AK, June, 2008.

[128] G. I. Taylor. Diffusion by Continuous Movements. *Proceedings of the London Mathematical Society*, s2-20(1):196–212, 1922.

[129] L. N. Thomas, A. Tandon, and A. Mahadevan. *Submesoscale Processes and Dynamics*, pages 17–38. American Geophysical Union (AGU), 2008.

[130] M. Thomas, C. A. Geiger, and C. Kambhamettu. High resolution (400 m) motion characterization of sea ice using ERS-1 SAR imagery. *Cold Regions Science and Technology*, 52(2):207–223, 2008.

[131] A. S. Thorndike and R. L. Colony. *Arctic Ocean Buoy Program data report 1 January 1980-31 December 1980*. Seattle, WA: Polar Science Center, University of Washington, 1981.

[132] M-L. Timmermans, J. Toole, A. Proshutinsky, R. Krishfield, and A. Plueddemann. Eddies in the Canada Basin, Arctic Ocean, Observed from Ice-Tethered Profilers. *Journal of Physical Oceanography*, 38(1):133 – 145, 2008.

[133] L. Toudal Pedersen and R. Saldo. Sentinel-1 provides ice drift observations for Copernicus Marine Environment Monitoring Service (CMEMS). In 2016 ESA Living Planet Symp., Prague, Czech Republic, May, 2016.

[134] M. Trodahl and P. E. Isachsen. Topographic Influence on Baroclinic Instability and the Mesoscale Eddy Field in the Northern North Atlantic Ocean and the Nordic Seas. *Journal of Physical Oceanography*, 48(11):2593 – 2607, 2018.

[135] M. Tschudi, W. N. Meier, J. S. Stewart, C. Fowler, and J. Maslanik. Polar pathfinder daily 25 km ease-grid sea ice motion vectors, version 4. [North]. Boulder, Colorado USA. NASA National Snow and Ice Data Center Distributed Active Archive Center. doi: https://doi.org/10.5067/INAWUWO7QH7B, 2019.

[136] M. A. Tschudi, W. N. Meier, and J. S. Stewart. An enhancement to sea ice motion and age products at the National Snow and Ice Data Center (NSIDC). *Cryosphere Discussions*, 14:1519–1536, 2020.

[137] D. C. Tseng and C. L. Chien. A cloud removal approach for aerial image visualization. *International Journal of Innovative Computing, Information and Control*, 9(6):2421–2440, 2013.

[138] T. Vihma, R. Pirazzini, I. Fer, I. A. Renfrew, J. Sedlar, M. Tjernström, C. Lüpkes, T. Nygård, D. Notz, J. Weiss, D. Marsan, B. Cheng, G. Birnbaum, S. Gerland, D. Chechin, and J. C. Gascard. Advances in understanding and parameterization of small-scale physical processes in the marine Arctic climate system: a review. *Atmospheric Chemistry and Physics*, 14(17):9403–9450, 2014.

[139] T. Vinje and O Finneskasa. *The ice transport through the Fram Strait*. Skrifter. Norsk Polarinstutt, Oslo, 1986.

[140] W.-J. von Appen, U. Schauer, R. Somavilla, E. Bauerfeind, and A. Beszczynska-Möller. Exchange of warming deep waters across Fram Strait. *Deep Sea Research Part I: Oceanographic Research Papers*, 103:86–100, 2015.

[141] W.-J. von Appen, C. Wekerle, L. Hehemann, V. Schourup-Kristensen, C. Konrad, and M. H. Iversen. Observations of a Submesoscale Cyclonic Filament in the Marginal Ice Zone. *Geophysical Research Letters*, 45(12):6141–6149, 2018.

[142] P. Wadhams and V. A. Squire. An ice-water vortex at the edge of the East Greenland Current. *Journal of Geophysical Research: Oceans*, 88(C5):2770–2780, 1983.

[143] J. S. Wagner, A. Gohm, A. Dörnbrack, and A. Schäfler. The mesoscale structure of a polar low: airborne lidar measurements and simulations. *Quarterly Journal of the Royal Meteorological Society*, 137(659):1516–1531, 2011.

[144] Y. Wang, Q. Chen, and B. Zhang. Image Enhancement Based on Equal Area Dualistic Sub-Image and Non-parametric Modified Histogram Equalization Method . *IEEE Transactions on Consumer Electronics*, 45(1):68–75, 1999.

[145] J. P. Wilkinson. Ice dynamics in the central Greenland Sea. *Journal of Geophysical Research: Oceans*, 111:C12022, 2006.

[146] R. E. Wolfe, M. Nishihama, A. J. Fleig, J. A. Kuyper, D. P. Roy, J. C. Storey, and F. S. Patt. Achieving sub-pixel geolocation accuracy in support of MODIS land science. *Remote Sensing of the Environment*, 83(1-2):31–49., 2002.

[147] R. E. Wolfe, D. P. Roy, and E. Vermote. MODIS land data storage, gridding, and compositing methodology: Level 2 grid. *IEEE Transactions on Geoscience and Remote Sensing*, 36(4):1324–1338, 1998.

[148] R. A. Woodgate, E. Fahrbach, and G. Rohardt. Structure and transport of the East Greenland Current at 75°N from moored current meters. *Journal of Geophysical Research: Oceans*, 104(C8):18059–18072, 1999.

[149] R. Yulmetov, A. Marchenko, and S. Løset. Iceberg and sea ice drift tracking and analysis off north-east Greenland. *Ocean Engineering*, 123:223–237, 2016.

[150] N. Zakhvatkina, A. Korosov, S. Muckenhuber, S. Sandven, and M. Babiker. Operational algorithm for ice-water classification on dual-polarized RADARSAT-2 images. *The Cryosphere*, 11(1):33–46., 2017.

[151] L. Zavala Sansón. Surface dispersion in the Gulf of California. *Progress in Oceanography*, 137:24–37, 2015.

[152] L. Zavala Sansón, P. Pérez-Brunius, and J. Sheinbaum. Surface Relative Dispersion in the Southwestern Gulf of Mexico. *Journal of Physical Oceanography*, 47(2):387 – 403, 2017.

[153] Y. Zhang, C. Chen, R. C. Beardsley, G. Gao, J. Qi, and H. Lin. Seasonal and interannual variability of the Arctic sea ice: A comparison between AO-FVCOM and observations. *Journal of Geophysical Research: Oceans*, 121(11):8320–8350, 2016.

[154] M. Zhao, M.-L. Timmermans, S. Cole, R. Krishfield, and J. Toole. Evolution of the eddy field in the Arctic Ocean's Canada Basin, 2005–2015. *Geophysical Research Letters*, 43(15):8106–8114, 2016.

[155] Y. Zhao, A. K. Liu, and D. G. Long. Validation of Sea Ice Motion from QuikSCAT with those from SSM/I and Buoy. *IEEE Transactions on Geoscience and Remote Sensing*, 40(6):1241–1246, 2002.